Design and Functions of Porous Organic Polymers

Huang, Ning

2015

Department of Structural Molecular Science

School of Physical Sciences

SOKENDAI

(The Graduate University for Advanced Studies)

Contents

General Introduction

Porous materials play important roles in various areas ranging from science to technology and have attracted considerable attention as a useful platform for advanced functional materials. In the last decades, the field of porous organic materials has attracted considerable attention because of the distinguished performance and widespread applications such as gas storage, gas separation, superhydrophobic interfaces, catalysis, energy conversion, energy storage, and optoelectronics. Synthetic chemists have developed fesible pathways to prepare a wide number of porous materials; however, it was still a graet challenge to construct organic porous networks by chemical synthesis until the emerge of the concept of reticular chemistry, which employs topologically designed organic molecules as building blocks to construct various novel organic porous materials.

1. Covalent Organic Frameworks

Covalent organic frameworks (COFs) are a novel kind of porous crystalline organic materials assembled from organic molecular building blocks.[1-6] The construction principles of such class of materials allow for the design of precisely controlled structures because their chemical and physical properties can be easily tuned through the selection of the building blocks and the linkage motif.[1] Yaghi and co-workers firstly exhibited the successful utility of the topologically designed principle in the synthesis of porous organic frameworks connected via strong covalent bonds in the solvothermal conditions, namely covalent organic frameworks (COFs) (**Figure 1**).[2a]

Composed of light-weight elements and linked by strong covalent bonds, covalent organic frameworks, demonstrate very low densities, high thermal and chemical stabilities, as well as permanent porosity.[2-4] Based on the topological design of various building blocks, COFs can be tail-made constructed into both two- (2D) and three-dimensions (3D). As for 2D COFs, the covalent bonded porous structure is sterically confined into 2D sheets which stack together to form a platelike eclipsed structure composed of periodically aligned 1D columns.[3-5] In contrast, 3D COFs, which extend this framework three-dimensionally through a building block containing an sp^3 carbon or silane atom (**Figure 2**), characteristically possess high specific surface areas (in

some cases larger than 4000 m^2 g^{-1}), numerous open sites, and low densities (as low as 0.17 g cm^{-3}). These features make 3D COFs ideal candidates for gas storage.

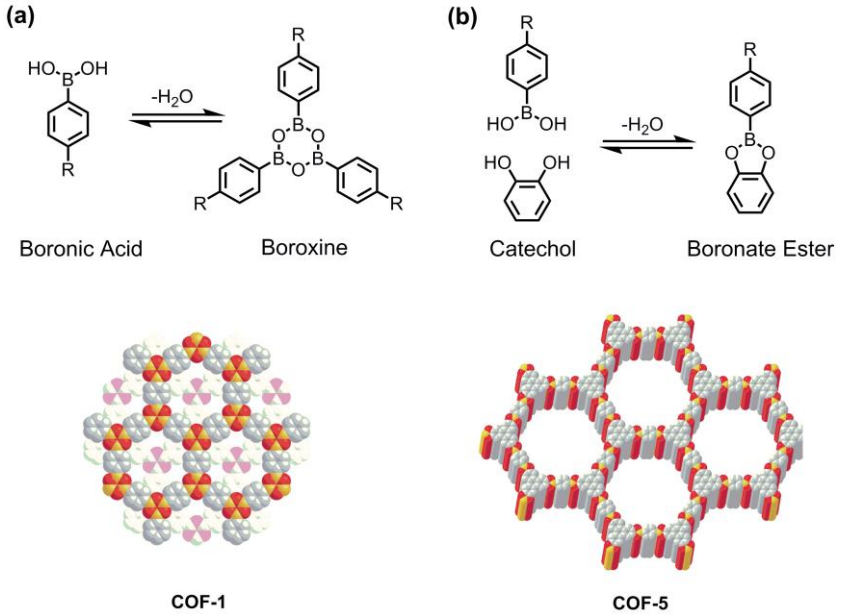

Figure 1. Reversible reactions of boronic acids: (a) self-condensation forms a boroxine ring resulting in a staggered COF-1, and (b) co-condensation with a catechol (HHTP) forms a boronate ester resulting in COF-5. Coloring scheme: C, gray; H, white, B, orange, O, red.

The synthesis of COFs has been achieved by kinetically controlled reactions, which can irreversibly form covalent bonds. Generally, it is very difficult to prepare crystalline organic cross-linked polymers using irreversible reactions. In contrast, dynamic reactions leads to the formation of covalent bonds, which can be reversibly formed, broken, and reformed. Therefore, unlike conventional covalent bond formation, this synthetic strategy is thermodynamically controlled and offers reversible pathway with "error checking" and "proof-reading" characteristics, resulting in the formation of the quite stable structures.

The design and synthesis of COFs have two important issues that must be taken into consideration to achieve thermodynamic control in reversible reactions: the structure of the building blocks and the synthetic method, including the reaction solvent and temperature.

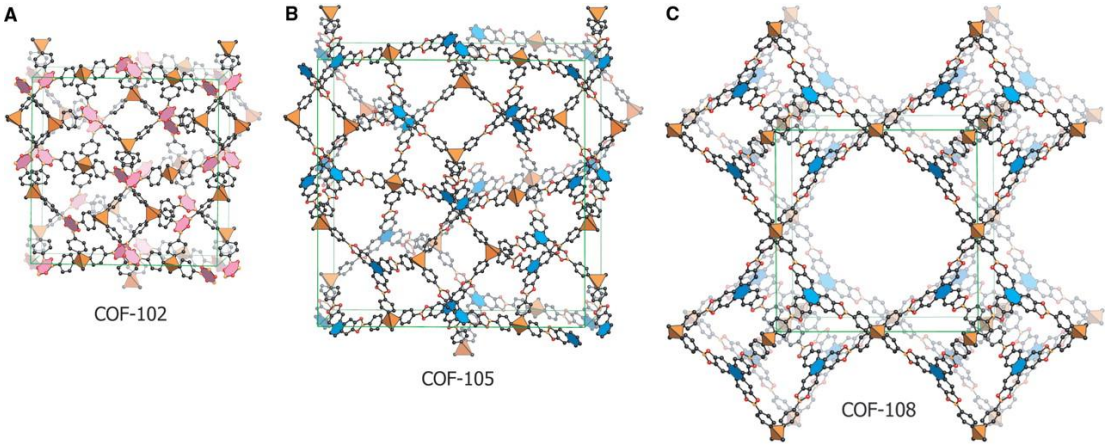

Figure 2. Modeled crystalline structures of COF-102 (A), COF-105 (B), and COF-108 (C).

To obtain crystalline and periodically ordered COFs, the structure of the building blocks must satisfy two required factors: a reversible reaction and the well preserved geometry of the building blocks. A series of reversible reactions have been employed to meet the requirement for successful COF synthesis (**Figure 3**). Most of the reported frameworks rely on the boron chemistry since boronic acids can be either self-condensed or co-condensed with catechols to form a six-membered boroxine and five-membered boronate ester linkages. Similar to the case of either boroxine or boronate esters, borosilicate linkages have been used to produce COFs through the condensation of a tetraboronic acid with tert-butylsilanetriol.

The specific geometries of building blocks enables the topological design of the COFs. As shown in **Figure 3**, the geometry of building blocks will determine the resulting structures of COFs. Therefore, the combinations such as 3D-T_d + 3D-T_d, 3D-T_d + 2D-C_2, or 3D-T_d + 2D-C_3 can generate the construction of 3D COFs with different crystalline space groups. In contrast, selected combinations of 2D blocks (*e.g.*, 2D-C_2 + 2D-C_3, 2D-C_3 + 2D-C_3 or 2D-C_2 + 2D-C_4) will afford 2D COFs with predesigned topologies and pore structures (**Figure 3**). The nature and discrete bonding direction of arenes makes aromatic π systems suitable building blocks for COFs. The diversity of aromatic systems allows numerous building block combinations, which endows the COFs with high flexibility in their topological design.

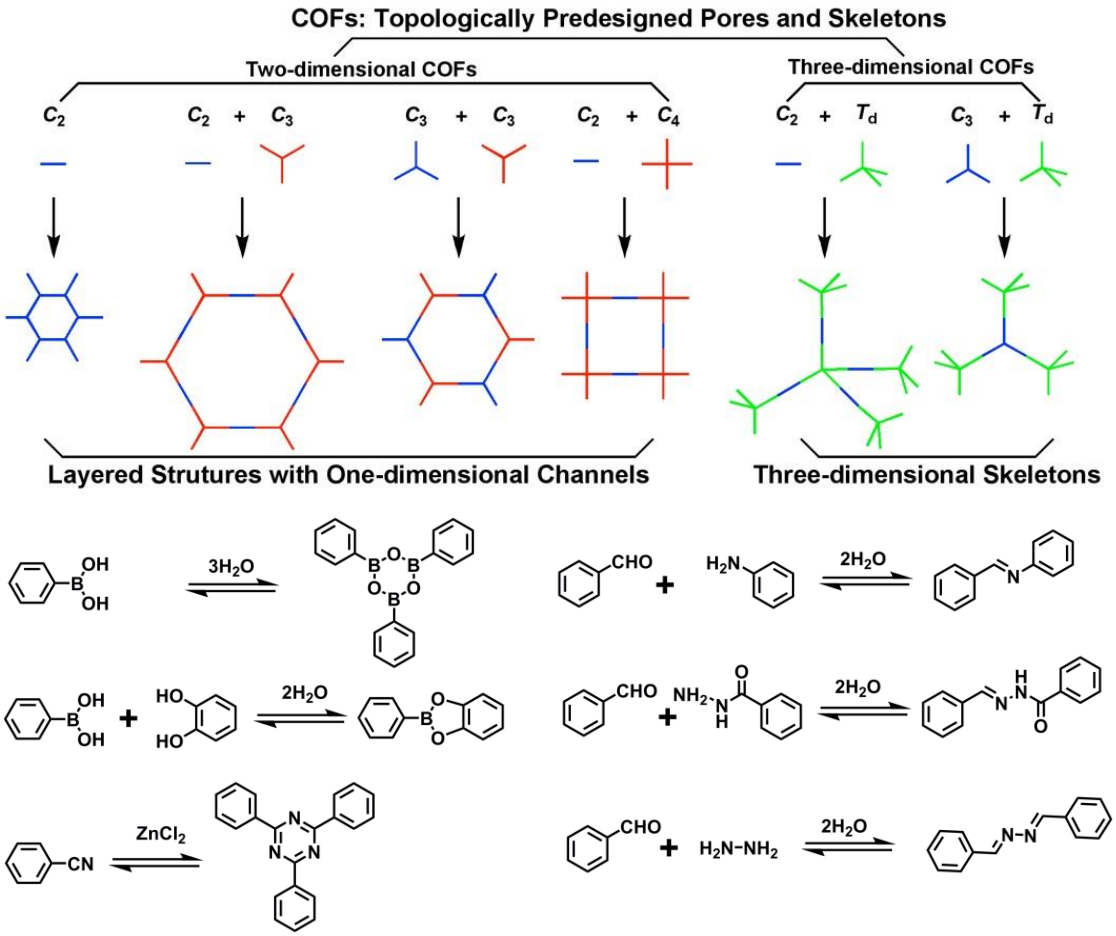

Figure 3. Schematic representation of the dynamic chemical reactions for the preparation of COFs and the combination of building blocks with different geometries to design 2D COFs.

The function of a COF arises from its porosity and molecular skeletons. As predesignable porous materials, COFs have been emerged as a new media for gas adsorption and storage. These frameworks can be further functionalized to contain catalytic sites for use as heterogeneous catalysts. Because of their unique topology and stacking layer structures, 2D COFs produce columnar arrays throughout their building blocks, which are difficult to synthesize using traditional supramolecular or conventional porous material approaches. In this sense, 2D COFs offer a new platform for the molecular design of semiconducting materials with periodic and built-in molecular ordering.

2. Cojugated Micro/Mesoporous Polymers

Among the covalently linked organic porous materials, CMPs are a class of amorphous materials that allow the linking of building blocks in a π-conjugated fashion and possess three-dimensional (3D) porous networks. Such kind of structural chatacters are very unique and are not available in the other porous counterparts, which are either not π-conjugated, or conventional conjugated polymers, which have no porous structures.[7-12] The first example of CMPs was reported by Cooper and coworks,[7a] after that, a large number of chemists and material scientists have contributed to the development of this field and drive the rapid growth of the CMP family. CMPs are unique in that they allow the complementary utilization of π-conjugated skeletons and nanopores for functional exploration; they have shown great potential for challenging energy and environmental issues, as exemplified by their excellent performance in gas adsorption, heterogeneous catalysis, light emitting, light harvesting and electrical energy storage.

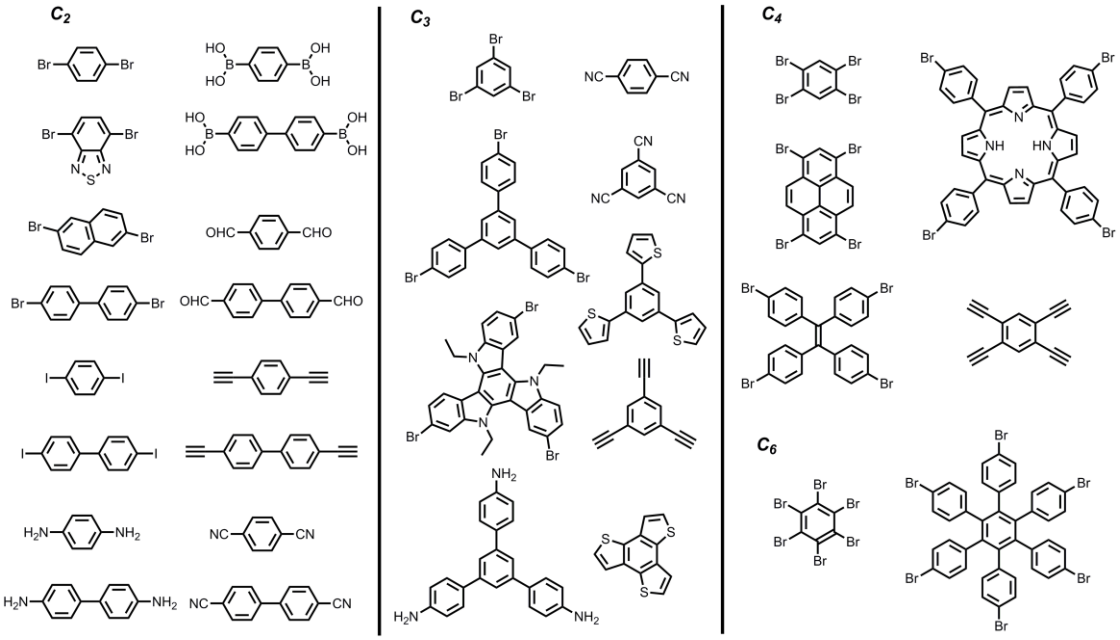

Figure 4. Schematic representation of the structures of building blocks with different geometries, sizes and reactive groups for the synthesis of CMPs.

The network architecture of CMPs have some demands that building blocks have at least two reactive sites. To construct the porous structure, connecting building blocks with different

functions and geometries to build a 3D polymer skeleton is necessary, whereas self-condensation reactions can contribute to homo-coupling of building blocks. Building blocks can be classified by their geometries into C_2, C_3, C_4 and C_6 categories (**Figure 4**). Self-condensation can result in the formation of 3D networks. At the same time, cross-coupling reactions typically use such combinations as $C_2 + C_3$,[7a,11e] $C_2 + C_4$,[11f,12a] $C_2 + C_6$,[12b] $C_3 + C_4$, $C_3 + C_6$ or $C_4 + C_6$.[12c] In both cases, nanopores are generated in confined 3D networks by covalent bonds, with permanent porosity in the resulting CMPs.

In order to build conjugated porous structures, the synthetic method must be able to link different kinds of building blocks with a covalent bond. Chemical reactions employed for the synthesis of linear conjugated polymers can also be utilizedf or CMP synthesis. Numerous coupling reactions, such as Suzuki cross-coupling, Yamamoto reaction, Sonogashira-Hagihara reaction, oxidative coupling reaction, Schiff-base reaction, Friedel-Crafts reaction, phenazine ring fusion reaction and cyclotrimerization have been well developed for the synthesis of CMPs. In iew of building blocks with different geometries, reactive sites, and π systems, the structural diversity significantly endows the flexibility of the design of desired skeletons and pores.

CMPs are also specific since they are nanoporous and π-conjugated, however, their structures can be easily designed and synthesized at the molecular level and topologically controlled. Resulting from high surface areas and porous characteristics, CMPs have come out as a new class of porous materials for gas storage and seperation. The inherent porosity supply open space and are accessible for various guest molecules and metal ions, allowing for the construction of supramolecular structures and organic-inorganic hybrids. Significantly, CMPs enable the complementary utilization of π-conjugated skeletons and nanopores for functional application. They have demonstrated great potential for challenging energy and environmental problems, as exemplified by their outstanding performance in such applications as gas adsorption, heterogeneous catalysis, light emitting, light harvesting and electric energy storage.

In summary, CMPs are a fascinating kind of materials with great potential for applications. The past efforts on the design, synthesis and functional exploration have demonstrated that CMPs are a versatile platform for structural and functional designs, which will continuously drive the further advancement of this emerging field.

3. Scope of This Thesis

In Chapter 1 and Chapter 2, I report a facile strategy for the pore surface functionalization of covalent organic frameworks (COFs) via a post-synthetic ring-opening and click reaction protocol, respectively (**Figure 5**). This approach allows the integration of functionalities such as carboxylic acid, amine, alcohol groups to the pore walls and combines a number of striking features including high-throughput synthesis, high crystallinity, large porosity, and robust chemical stability. The pore surface functionalization exerts a prominent effect on the uptake of carbon dioxide by increasing the capacity to 3-4 folds, which ties the highest capacity among the porous materials. These considerable effects demonstrate the significance and effectiveness of rational post-synthetic functionalization of pore surface in the exploration of COF.

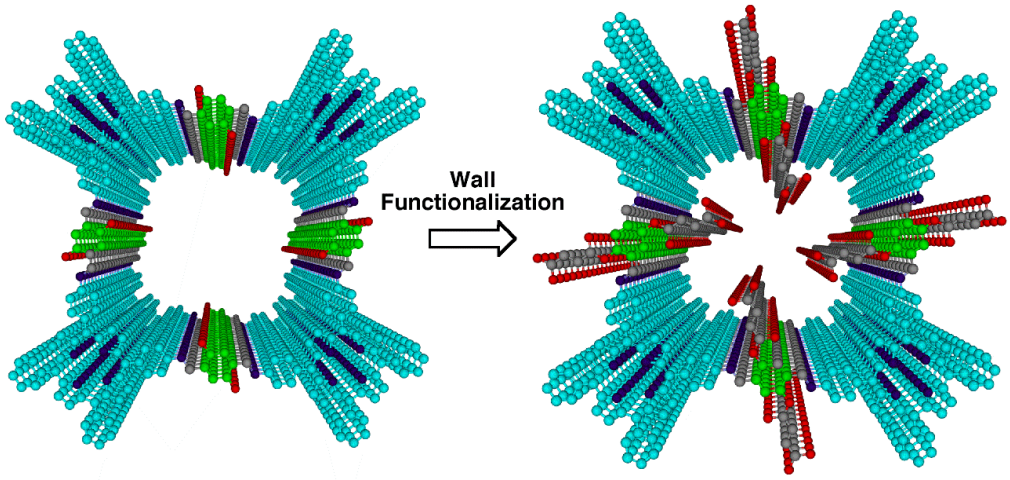

Figure 5. Eclipsed stack of phthalocyanine 2D sheets and microporous channels in NiPc-COF (a 2 × 2 grid). Colors used for identification are as follows: phthalocyanine unit (sky blue), Ni (green), N (violet), C (grey), O (red), B (orange) and H (white).

In Chapter 2, highly cross linked mesoporous conjugated polymer H_2P-CMP stabilized Pd nanoparticles (PdNPs⊃H_2P-CMP) were prepared by straightforward post synthetic method. The catalytic activity of PdNPs⊃H_2P-CMP was high enough for Suzuki cross coupling reactions of aryl chlorides under thermal and microwave heating conditions in aqueous solution. PdNPs⊃H_2P-CMP exhibited high catalytic activity and recycled for eight times with loss of activity (**Figure 6**).

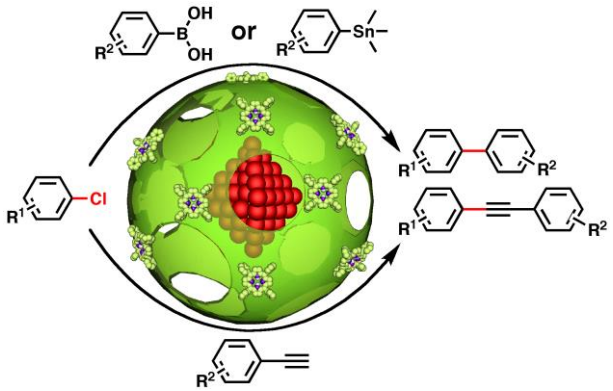

Figure 6. Uncovered and stable palladium nanoparticles are synthesized by using a mesoporous π-network are disclosed to serve as high performance heterogeneous catalyst in water.

In Chapter 3, I firstly developed a methodology using electropolymerization for the synthesis of thin CMP films (**Figure 7**). The thickness of these films is synthetically controllable, ranging from nanometers to micrometers, and they are obtained on substrates or as freestanding films. The CMP films combine a number of striking physical properties, including high porosity, extended π conjugation, facilitated exciton delocalization, and high-rate electron transfer. I explored the CMP films as versatile platforms for highly sensitive and label-free chemo- and biosensing of electron-rich and electron-poor arenes, metal ions, dopamine, and hypochloroic acid, featuring rapid response, excellent selectivity, and robust reusability.

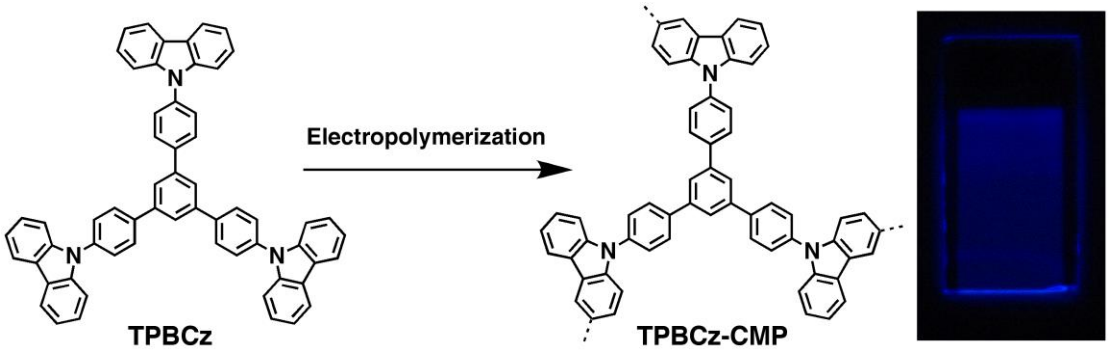

Figure 7. a) Schematic representation of the electrochemical synthesis of TPBCz-CMP films. b) Elementary pore of the film. Photos of c) a film on an ITO substrate (0.5×1.5 cm^2), d) the film under UV light, and e) a 100 nm thick freestanding film (0.5×1 cm^2) in acetonitrile. Scale bars: 0.5 cm.

References

1. X. Feng, X. Ding, D. Jiang, *Chem. Soc. Rev.* **2012**, *41*, 6010-6022.

2. a) A. P. Côté, A. I. Benin, N. W. Ockwig, M. O'Keeffe, A. J. Matzger, O. M. Yaghi, *Science* **2005**, *310*, 1166-1170; b) H. M. El-Kaderi, J. R. Hunt, J. L. Mendoza-Cortés, A. P. Côté, R. E. Taylor, M. O'Keeffe, O. M. Yaghi, *Science* **2007**, *316*, 268-272; c) A. P. Côté, H. M. El-Kaderi, H. Furukawa, J. R. Hunt, O. M. Yaghi, *J. Am. Chem. Soc.* **2007**, *129*, 12914-12915; d) J. R. Hunt, C. J. Doonan, J. D. LeVangie, A. P. Cote, O. M. Yaghi, *J. Am. Chem. Soc.* **2008**, *130*, 11872-11873; e) C. J. Doonan, D. J. Tranchemontagne, T. G. Glover, J. R. Hunt, O. M. Yaghi, *Nature Chem.* **2010**, *2*, 235-238. f) S. Wan, F. Gndara, A. Asano, H. Furukawa, A. Saeki, S. K. Dey, L. Liao, M. W. Ambrogio, Y. Y. Botros, X. Duan, S. Seki, J. F. Stoddart, O. M. Yaghi, *Chem. Mater.* **2011**, *23*, 4094-4097; g) F. J. Uribe-Romo, C. J. Doonan, H. Furukawa, K. Oisaki and O. M. Yaghi, *J. Am. Chem. Soc.* **2011**, *133*, 11478-11481.

3. a) R. W. Tilford, W. R. Gemmill, H. C. zur Loye, J. J. Lavigne, *Chem. Mater.* **2006**, *18*, 5296-5301; b) R. W. Tilford, S. J. Mugavero, P. J. Pellechia, J. J. Lavigne, *Adv. Mater.* **2008**, *20*, 2741-2746; c) L. M. Lanni, R. W. Tilford, M. Bharathy, J. J. Lavigne, *J. Am. Chem. Soc.* **2011**, *133*, 13975-13983; d) M. Dogru, A. Sonnauer, A. Gavryushin, P. Knochel, T. Bein, *Chem. Commun.* **2011**, *47*, 1707-1709.

4. S. Y. Ding, J. Gao, Q. Wang, Y. Zhang, W. G. Song, C. Y. Su and W. Wang, *J. Am. Chem. Soc.* **2011**, *133*, 19816-19822.

5. a) S. Wan, J. Guo, J. Kim, H. Ihee, D. Jiang, *Angew. Chem.* **2008**, *120*, 8958-8962; *Angew. Chem. Int. Ed.* **2008**, *47*, 8826-8830; b) S. Wan, J. Guo, J. Kim, H. Ihee, D. Jiang, *Angew. Chem.* **2009**, *121*, 5547-5550; *Angew. Chem. Int. Ed.* **2009**, *48*, 5439- 5442; c) A. Nagai, Z. Guo, X. Feng, S. Jin, X. Chen, X. Ding, D. Jiang, *Nat. Commun.* **2011**, *2*, 536; d) X. Ding, J. Guo, X. Feng, Y. Honsho, J. D. Guo, S. Seki, P. Maitarad, A. Saeki, S. Nagase, D. Jiang, *Angew. Chem.* **2011**, *123*, 1325-1329; *Angew. Chem. Int. Ed.* **2011**, *50*, 1289-1293; e) X. Ding, L. Chen, Y. Honso, X. Feng, O. Saengsawang, J. D. Guo, A. Saeki, S. Seki, S. Irle, S. Nagase, V. Parasuk, D. Jiang, *J. Am. Chem. Soc.* **2011**, *133*, 14510-14513; f) X. Feng, L. Chen, Y. P. Dong, D. Jiang, *Chem. Commun.* **2011**, *47*, 1979-1981; g) X. Feng, L. Chen, Y. P. Dong, D. Jiang, *Chem. Commun.* **2011**, *47*, 1979-1981; h) X. Feng, L. Liu, Y. Honsho, A. Saeki, S. Seki, S. Irle, Y. P.

Dong, A. Nagai, D. Jiang, *Angew. Chem.* **2012**, *124*, 2672-2676; *Angew. Chem. Int. Ed.* **2012**, *51*, 2618-2622; i) X. Feng, L. Chen, Y. Honsho, O. Saengsawang, L. Liu, L.Wang, A. Saeki, S. Irle, S. Seki, Y. P. Dong, D. Jiang, *Adv. Mater.* **2012**, *24*, 3026-3031; j) X. Ding, X. Feng, A. Saeki, S. Seki, A. Nagai, D. Jiang, *Chem. Commun.* **2012**, *48*, 8952-8954; k) X. Feng, Y. P. Dong, D. Jiang, *CrystEngComm.* **2013**, *15*, 1508-1511; l) X. Chen, M. Addicoat, S. Irle, A. Nagai, D. Jiang, *J. Am. Chem. Soc.* **2013**, *135*, 546-549; m) S. Jin, X. Ding, X. Feng, M. Supur, K. Furukawa, S. Takahashi, M. Addicoat, M. E. El-Khouly, T. Nakamura, S. Irle, S. Fukuzumi, A. Nagai, D. Jiang, *Angew. Chem.* **2013**, *125*, 2071-2075; *Angew. Chem., Int. Ed.* **2013**, *52*, 2017-2021; n) A. Nagai, X. Chen, X. Feng, X. Ding, Z. Guo, D. Jiang, *Angew. Chem.* **2013**, *125*, 3858-3862; *Angew. Chem., Int. Ed.* **2013**, *52*, 3770-3774; o) S. Jin, K. Furukawa, M. Addicoat, L. Chen, T. Seiya, S. Irle, T. Nakamura, D. Jiang, *Chem. Sci.* **2013**, *4*, 4505-4511.

6. a) E. L. Spitler, W. R. Dichtel, *Nature Chem.* **2010**, *2*, 672-677; b) J. W. Colson, A. R. Woll, A. Mukherjee, M. P. Levendorf, E. L. Spitler, V. B. Shields, M. G. Spencer, J. Park, W. R. Dichtel, *Science* **2011**, *228*, 228-231; c) E. L. Spitler, B. T. Koo, J. L. Novotney, J. W. Colson, F. J. Uribe-Romo, G. D. Gutierrez, P. Clancy, W. R. Dichtel, *J. Am. Chem. Soc.* **2011**, *133*, 19416-19421; d) E. L. Spitler, J. W. Colson, F. J. Uribe-Romo, A. R. Woll, M. R. Giovino, A. Saldivar, W. R. Dichtel, *Angew. Chem.* **2012**, *124*, 2677-2681; *Angew. Chem., Int. Ed.* **2012**, *51*, 2623-2727; e) D. N. Bunck, W. R. Dichtel, *Angew. Chem.* **2012**, *124*, 1921-1925; *Angew. Chem., Int. Ed.* **2012**, *51*, 1885-1889; f) B. T. Koo, W. R. Dichtel, P. Clancy, *J. Mater. Chem.* **2012**, *22*, 17460-17469. g) D. N. Bunck, W. R. Dichtel, *Chem. Commun.* **2013**, *49*, 2457-2459; h) C. R. DeBlase, K. E. Silberstein, T.-T. Truong, H. D. Abruña, and W. R. Dichtel, *J. Am. Chem. Soc.* **2013**, *135*, 16821–16824; i) H. Xu, X. Chen, J. Gao, J. B. Lin, M. Addicoat, S. Irle, D. L. Jiang, *Chem. Commun.* **2014**, *50*, 1292-1294.
7. a) S. H. Chen, R. F. Horvath, J. Joglar, M. J. Fisher and S. J. Danishefsky, *J. Org. Chem.*, **1991**, *56*, 5834-5845; b) A. Suzuki, *Chem. Commun.* **2005**, 4759-4763; c) Y. F. Wang, W. Deng, L. Liu and Q. X. Guo, Chin. *J. Org. Chem.* **2005**, *25*, 8-24; d) J. X. Jiang, F. B. Su, A. Trewin, C. D. Wood, N. L. Campbell, H. J. Niu, C. Dickinson, A. Y. Ganin, M. J. Rosseinsky, Y. Z. Khimyak and A. I. Cooper, *Angew. Chem., Int. Ed.* **2007**, *46*, 8574-8578; e) J. Langecker and M. Rehahn,

Macromol. *Chem. Phys.* **2008**, *209*, 258-271; f) A. Suzuki, *Angew. Chem., Int. Ed.* **2011**, *50*, 6722-6737.

8. a) E. H. Cordes and W. P. Jencks, *J. Am. Chem. Soc.* **1962**, *84*, 832-837; b) C. Liu, H. Zhang, W. Shi and A. W. Lei, *Chem. Rev.* **2011**, *111*, 1780-1824; c) W. Shi, C. Liu and A. Lei, *Chem. Soc. Rev.* **2011**, *40*, 2761-2776; d) R. Chinchilla and C. Nájera, *Chem. Soc. Rev.* **2011**, *40*, 5084-5121.
9. a) V. Gevorgyan and Y. Yamamoto, *J. Organomet. Chem.* **1999**, *576*, 232-247; b) S. Kotha, E. Brahmachary and K. Lahiri, Eur. *J. Org. Chem.* **2005**, 4741-4767; c) B. Karami and S. Khodabakhshi, J. Serb. *Chem. Soc.* **2011**, *76*, 1191-1198.
10. a) M. Yamada, Y. Tanaka, Y. Yoshimoto, S. Kuroda and I. Shimao, *Bull. Chem. Soc. Jpn.* **1992**, *65*, 1006-1011; b) M. Hayashi, S. Z. Nakayama and H. Kawabata, *Chem. Commun.* **2000**, 1329-1330; c) P. Kuhn, M. Antonietti and A. Thomas, *Angew. Chem., Int. Ed.* **2008**, *47*, 3450-3453; d) S. W. Yuan, B. Dorney, D. White, S. Kirklin, P. Zapol, L. P. Yu and D. J. Liu, *Chem. Commun.* **2010**, *46*, 4547-4549; e) J. A. McCubbin and O. V. Krokhin, *Tetrahedron Lett.* **2010**, *51*, 2447-2449.
11. a) J. X. Jiang, F. B. Su, A. Trewin, C. D. Wood, H. J. Niu, J. T. A. Jones, Y. Z. Khimyak and A. I. Cooper, *J. Am. Chem. Soc.* **2008**, *130*, 7710-7720; b) J. X. Jiang, F. Su, H. Niu, C. D. Wood, N. L. Campbell, Y. Z. Khimyak and A. I. Cooper, *Chem. Commun.* **2008**, 486-488; c) J. Schmidt, M. Werner and A. Thomas, *Macromolecules* **2009**, *42*, 4426-4429; d) J. X. Jiang, A. Trewin, D. J. Adams and A. I. Cooper, *Chem. Sci.* **2011**, *2*, 1777-1781; e) Y. H. Xu, L. Chen, Z. Q. Guo, A. Nagai and D. Jiang, *J. Am. Chem. Soc.* **2011**, *133*, 17622-17625; f) G. Cheng, T. Hasell, A. Trewin, D. J. Adams and A. I. Cooper, *Angew. Chem., Int. Ed.* **2012**, *51*, 12727-12731.
12. a) L. Chen, Y. Honsho, S. Seki and D. Jiang, *J. Am. Chem. Soc.* **2010**, *132*, 6742-6748; b) Q. Chen, M. Luo, T. Wang, J. X. Wang, D. Zhou, Y. Han, C. S. Zhang, C. G. Yan and B. H. Han, *Macromolecules* **2011**, *44*, 5573-5577; c)Y. Kou, Y. Xu, Z. Guo and D. Jiang, *Angew. Chem., Int. Ed.* **2011**, *50*, 8753-8757.

Part I

Covalent Organic Frameworks

Chapter 1

Covalent Organic Frameworks for Carbon Dioxide Capture through Channel-Wall Functionalization

Angew. Chem., Int. Ed., 2015, **54**, 2986-2990.

Ning Huang, Xiong Chen, Rajamani Krisna and Donglin Jiang

Abstract: Ordered open channels found in two-dimensional covalent organic frameworks (2D COFs) could enable them to adsorb carbon dioxide. However, the frameworks' dense layer architecture results in low porosity that has thus far restricted their potential for carbon dioxide adsorption. Here I report a strategy for converting a conventional 2D COF into an outstanding platform for carbon dioxide capture through channel-wall functionalization. The dense layer structure enables the dense integration of functional groups on the channel walls, creating a new version of COFs with high capacity, reusability, selectivity, and separation productivity for flue gas. These results suggest that channel-wall functional engineering could be a facile and powerful strategy to develop 2D COFs for high-performance gas storage and separation.

Keywords: carbon dioxide; covalent organic frameworks; flue gas separation; gas adsorption; synthesis

Introduction

Covalent organic frameworks (COFs), a class of crystalline porous polymers that allow the atomically precise integration of building blocks into periodicities, have emerged as a new platform for designing advanced organic materials with periodic structures.[1-5] Two-dimensional (2D) COFs have limited surface areas and small pore volumes as a result of their dense π-stacking layer structure, which greatly restricts their potential as a porous medium for the adsorption of gases such as carbon dioxide, methane, and hydrogen. With the exception of two examples utilizing azine[2b] and boronate[3d] linkages that interact with specific gas molecules to exhibit good capacity, the majority of 2D COFs have very low performance in gas adsorption. To improve this situation, I present a strategy that explores the channel walls for functional engineering and demonstrate its significance and effectiveness in the design of 2D COFs for high-performance gas adsorption and separation.

Results and Discussions

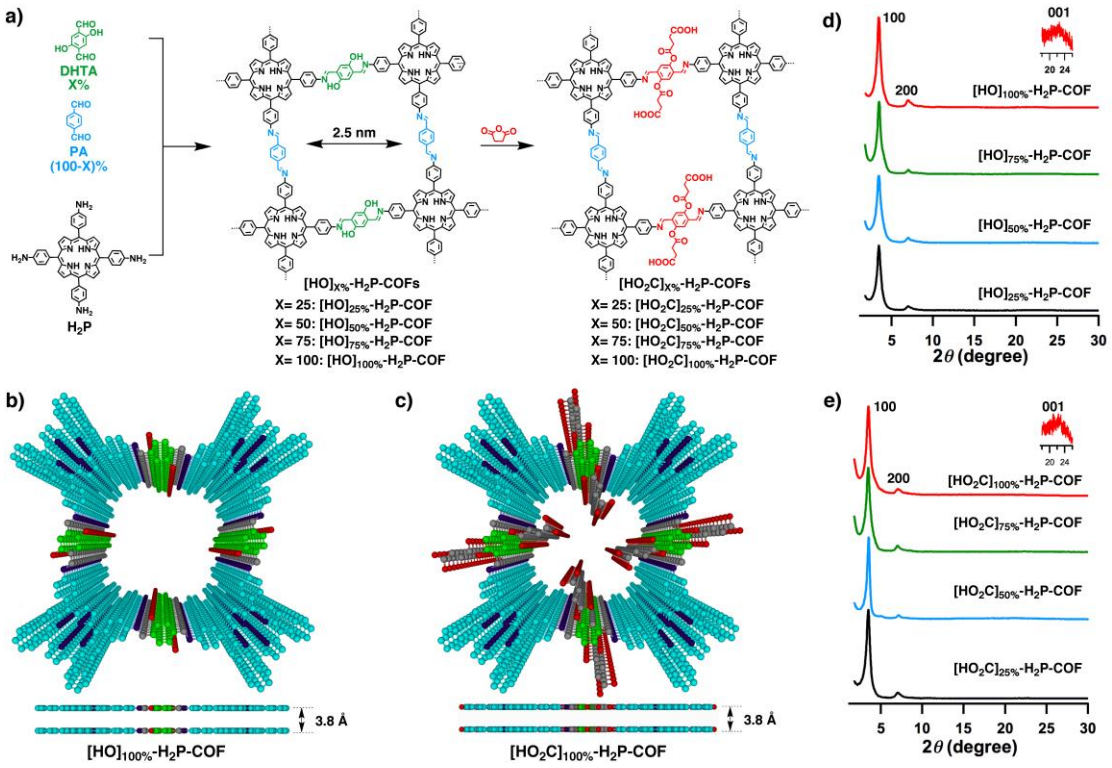

Figure 1. a) Synthesis of $[HO_2C]_{X\%}$-H_2P-COFs with channel–walls functionalized with carboxylic acid groups via the ring-opening reaction of $[OH]_{X\%}$-H_2P-COFs with succinic anhydride. Top and

side views of (b) $[HO]_{100\%}$-H_2P-COF and (c) $[HO_2C]_{100\%}$-H_2P-COF. XRD patterns of (f) $[OH]_{X\%}$-H_2P-COFs and (g) $[HO_2C]_{X\%}$-H_2P-COFs.

The advantage of the dense layer structure of 2D COFs is that this architecture enables the dense incorporation of functional groups onto the channel walls. This structural benefit compensates for the low porosity of 2D COFs. I observed that functional engineering of the channel walls converts a conventional 2D COFs into an outstanding carbon-dioxide-capture material. I demonstrated this strategy by using a conventional imine-linked 2D COF (**Figures 1**a, b, $[HO]_{100\%}$-H_2P-COF) as a scaffold with porphyrin at the vertices and phenol units on the pore walls; this 2D COF exhibits a low capacity for carbon dioxide adsorption. The phenol groups undergo a quantitative ring-opening reaction with succinic anhydride that decorate the channel walls with open carboxylic acid groups (**Figures 1**a, c, $[HO_2C]_{100\%}$-H_2P-COF). The content of

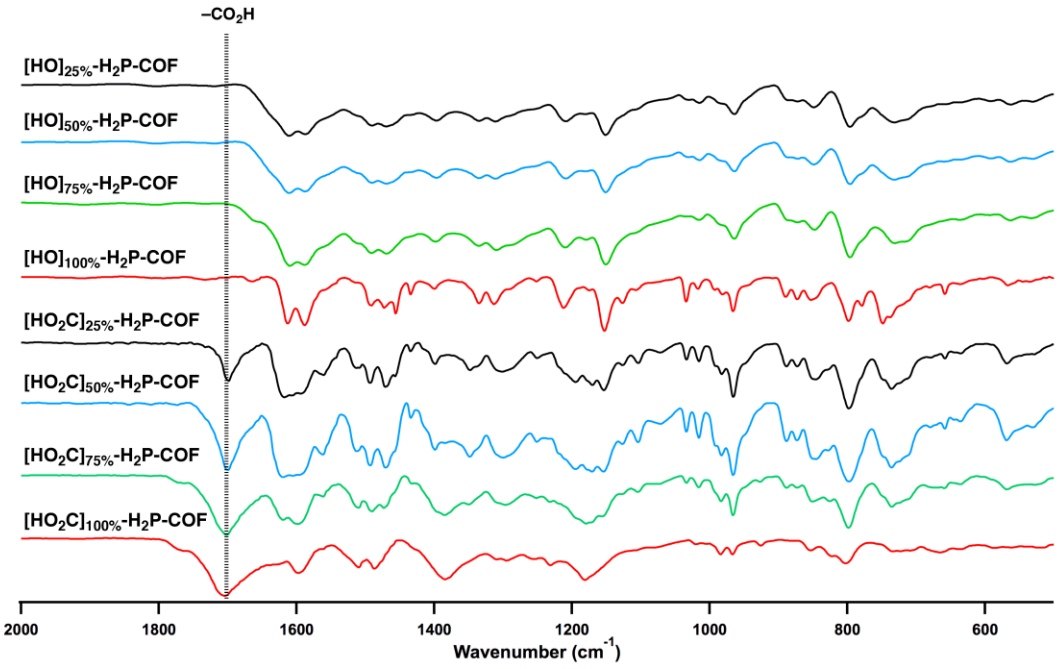

Figure 2. IR spectra of $[OH]_{X\%}$-H_2P-COFs and $[COOH]_{X\%}$-H_2P-COFs.

carboxylic acid units on the channel walls was tuned by adjusting the content of phenol groups via a three-component condensation system with a mixture of 2,5-dihydroxyterephthalaldehyde (DHTA) and 1,4-phthalaldehyde (PA) as the wall components (**Figure 1**a, $[HO]_{X\%}$-H_2P-COFs, X

= [DHTA]/([DHTA] + [PA])). Various analytic methods revealed that the DHTA-to-PA molar ratios integrated into $[HO]_{X\%}$-H_2P-COFs were identical to those employed for the reactions (**Figures 2, 3**). Using this method, I synthesized a series of $[HO_2C]_{X\%}$-H_2P-COFs with controlled carboxylic acid density that varied from 25% to 50%, 75%, and 100% (**Figure 1c,**). The $[HO_2C]_{X\%}$-H_2P-COFs were characterized using infrared spectroscopy (**Figure 2**), elemental and thermogravimetric analysis (**Table 1, Figure 3**), energy dispersive X-ray spectrometry (**Table 2,**

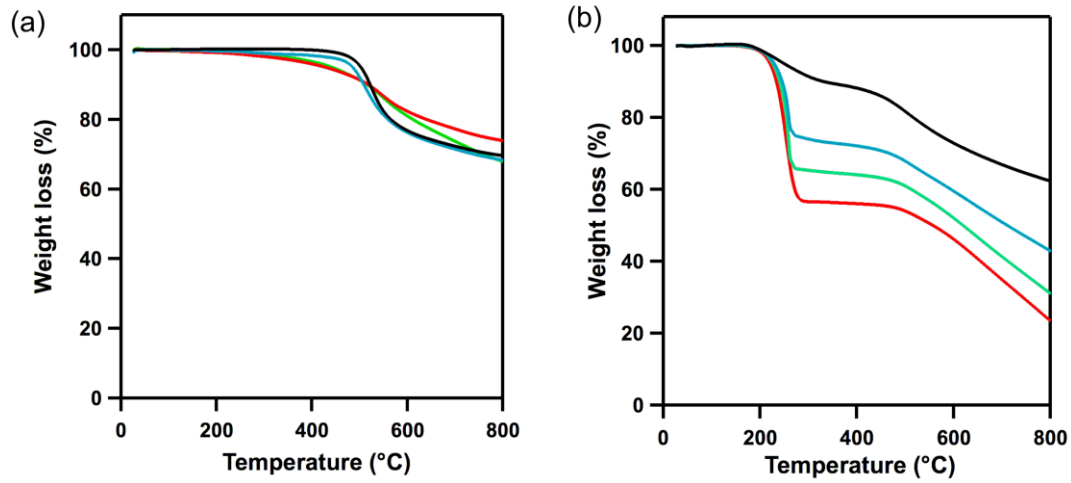

Figure 3. a) TGA curves of $[HO]_{X\%}$-H_2P-COFs (red: $[HO]_{100\%}$-H_2P-COF, green: $[HO]_{75\%}$-H_2P-COF, blue: $[HO]_{50\%}$-H_2P-COF, black: $[HO]_{25\%}$-H_2P-COF); b) TGA curves of $[CO_2H]_{X\%}$-H_2P-COF.

Figure 4) and X-ray diffraction (XRD) measurements (**Figure 1e**). These methods reveal that the content of carboxylic acid units integrated into the channel walls is close to the X% value of $[HO_2C]_{X\%}$-H_2P-COFs. Notably, compared to metal-catalyzed azide-ethynyl[2c, 2d] or other click reactions,[4c] this ring-opening reaction is free of metal catalysts, proceeds smoothly and cleanly, and excludes the formation of metal nanoparticles that would contaminate the channels.

The $[HO]_{100\%}$-H_2P-COF samples exhibited strong XRD peaks at 3.49 °, 7.21 °, and 23.1 °, which are assignable to 100, 200, and 001 facets, respectively (**Figure 1d, red curve**).[2d] Other $[HO]_{X\%}$-H_2P-COFs exhibited identical diffraction patterns (**Figure 1d**). The $[HO_2C]_{X\%}$-H_2P-COFs exhibit XRD patterns (**Figure 1e**) similar to those of $[HO]_{X\%}$-H_2P-COFs, which indicates that the crystal structure of $[HO_2C]_{X\%}$-H_2P-COFs is similar to that of $[HO]_{100\%}$-H_2P-COF.[2d] The presence

of (001) facet at 23.1 °, which correspondis to an interlayer interval of 3.8 Å, indicates that $[HO]_{X\%}$-H_2P-COFs and $[HO_2C]_{X\%}$-H_2P-COFs have dense π-stacking layer structures (**Figures 1b, c**).

Table 1. Elemental analysis results of $[HO]_{X\%}$-H_2P-COFs and $[HO_2C]_{X\%}$-H_2P-COFs.

COFs		C%	H%	N%
$[HO]_{25\%}$-H_2P-COF	Calcd.	76.95	4.25	11.97
	Found	74.92	4.88	10.87
$[HO]_{50\%}$-H_2P-COF	Calcd.	78.29	4.33	12.17
	Found	76.68	4.68	11.54
$[HO]_{75\%}$-H_2P-COF	Calcd.	79.67	4.40	12.39
	Found	78.24	4.87	10.92
$[HO]_{100\%}$-H_2P-COF	Calcd.	81.11	4.48	12.61
	Found	78.62	5.03	11.28
$[HO_2C]_{25\%}$-H_2P-COF	Calcd.	74.05	4.37	10.79
	Found	70.42	4.87	8.67
$[HO_2C]_{50\%}$-H_2P-COF	Calcd.	71.76	4.34	9.85
	Found	69.34	4.71	8.72
$[HO_2C]_{75\%}$-H_2P-COF	Calcd.	69.84	4.31	9.05
	Found	68.46	4.92	7.82
$[HO_2C]_{100\%}$-H_2P-COF	Calcd.	68.21	4.29	8.37
	Found	64.43	5.17	7.02

The crystal structures of $[HO]_{X\%}$-H_2P-COFs and $[HO_2C]_{X\%}$-H_2P-COFs suggest the presence of open nanochannels (**Figures 1b, c**). The $[HO]_{X\%}$-H_2P-COFs exhibit typical type-IV nitrogen sorption isotherm profiles indicative of mesoporous character (**Figure 5**). Notably, the Brunauer-Emmett-Teller (BET) surface area (1054-1284 $m^2\ g^{-1}$), pore volume (0.89-1.02 $cm^3\ g^{-1}$), and pore size (2.5 nm) remained nearly unchanged (**Table 3**). Pore size distribution profiles revealed that these COFs possess a single type of mesopores (**Figures 5b-e**). Therefore, the

three-component condensation reaction is reasonably concluded to allow for the integration of phenol groups in a controlled manner while retaining crystallinity and porosity.

Functionalization of the channel walls with carboxylic acid groups triggers microporosity in $[HO_2C]_{X\%}$-H_2P-COFs, as evidenced by their typical type-I sorption curves (**Figure 5f)**. The BET

Table 2. Energy dispersive X-ray spectrometry (EDX) analysis of $[HO]_{X\%}$-H_2P-COFs and $[HO_2C]_{X\%}$-H_2P-COFs

COFs		C%	O%	N%
$[HO]_{25\%}$-H_2P-COF	Calcd.	76.95	6.83	11.97
	Found	77.36	5.92	12.50
$[HO]_{50\%}$-H_2P-COF	Calcd.	78.29	5.21	12.17
	Found	77.2	5.01	13.41
$[HO]_{75\%}$-H_2P-COF	Calcd.	79.67	3.54	12.39
	Found	78.8	3.83	12.91
$[HO]_{100\%}$-H_2P-COF	Calcd.	81.11	1.8	12.61
	Found	82.93	1.81	10.92
$[HO_2C]_{25\%}$-H_2P-COF	Calcd.	74.05	10.79	10.79
	Found	74.50	10.06	11.06
$[HO_2C]_{50\%}$-H_2P-COF	Calcd.	71.76	14.05	9.85
	Found	70.33	14.95	10.38
$[HO_2C]_{75\%}$-H_2P-COF	Calcd.	69.84	16.8	9.05
	Found	68.61	16.98	10.09
$[HO_2C]_{100\%}$-H_2P-COF	Calcd.	68.21	19.13	8.37
	Found	67.08	19.70	8.92

surface area (S_{BET}) decreased from 786 to 673, 482, and 364 $m^2\ g^{-1}$, whereas the pore size decreased from 2.2 to 1.9, 1.7, and 1.4 nm (**Table 3**), as the content of carboxylic groups was increased from 25% to 50%, 75%, and 100%, respectively. The pore volume also decreased from 0.78 to 0.66, 0.54, and 0.43 $cm^3\ g^{-1}$, as the content of carboxylic groups was increased. This reduction in porosity is indicative of space filling by the functional units appended to the channel

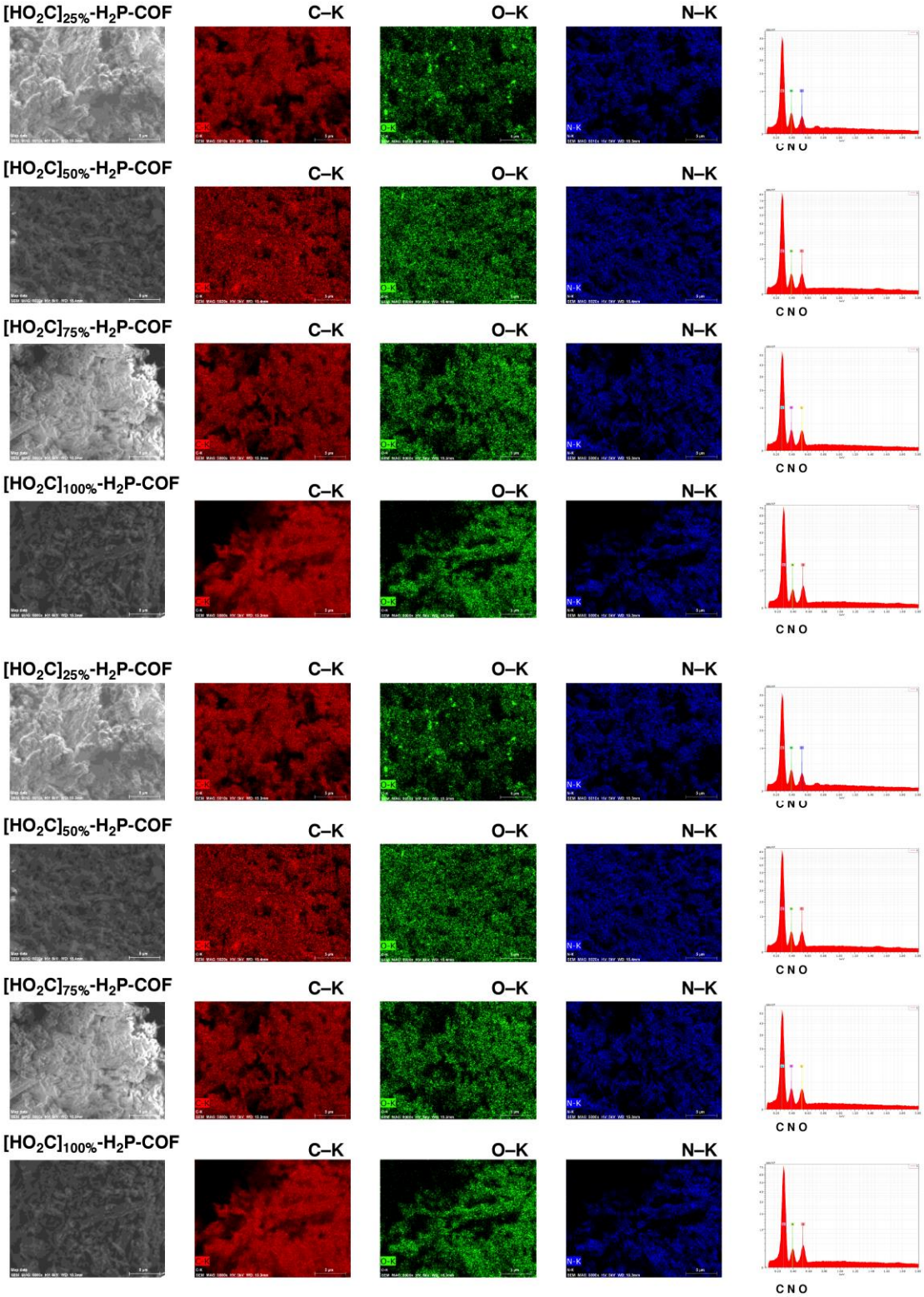

Figure 4. EDX analysis of $[HO]_{X\%}$-H_2P-COFs and $[HO_2C]_{X\%}$-H_2P-COFs.

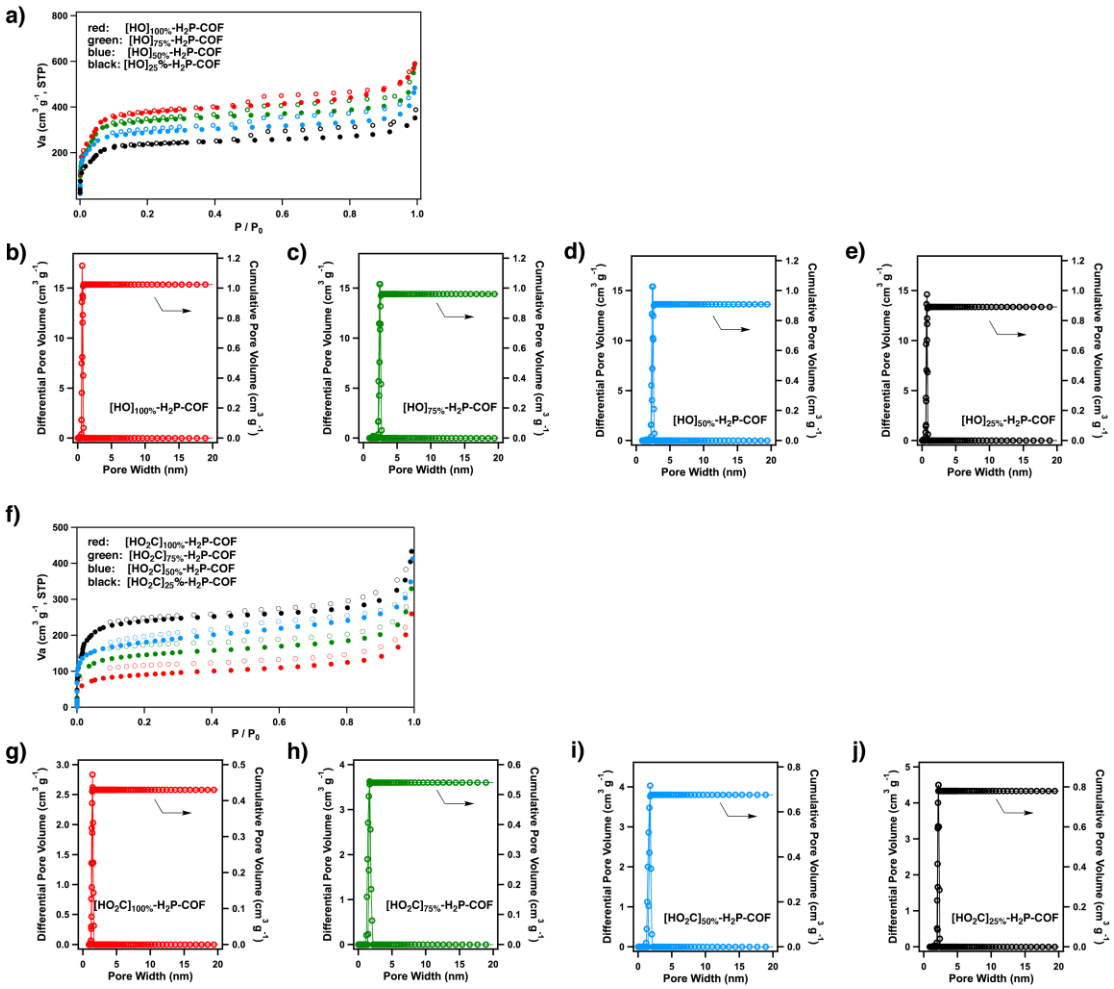

Figure 5. a) Nitrogen sorption isotherm curves of $[HO]_{X\%}$-H_2P-COFs. b-e) Pore size and pore size distribution profiles of $[HO]_{X\%}$-H_2P-COFs. f) Nitrogen sorption isotherm curves of $[HO_2C]_{X\%}$-H_2P-COFs. g-j) Pore size and pore size distribution profiles of $[HO_2C]_{X\%}$-H_2P-COFs.

walls. Notably, the pore size distribution profiles revealed that porosity was solely derived from the micropores (**Figures 5g-j**). This observation suggests that the channel walls were randomly functionalized with carboxylic acid groups in the case of $[HO_2C]_{X\%}$-H_2P-COFs (X = 25, 50, and 75). Stability test revealed that $[HO_2C]_{X\%}$-H_2P-COF was stable upon immersion in THF, water, and aqueous HCl (1 M), $NaHCO_3$ (1 M), and KOH (1 M) solutions for 24 h (**Figure 6**).

Carboxylic acid groups have been reported to trigger a dipolar interaction with carbon dioxide.[6a-6f] In $[HO_2C]_{X\%}$-H_2P-COFs, the carboxylic acid units are located at the termini and exhibit an acidity similar to that of the free carboxylic acid, as evidenced by their pK_a values of 5.86. I first investigated the CO_2 adsorption by $[HO]_{X\%}$-H_2P-COFs at pressures up to 1 bar and at

temperatures of 273 K (**Figure 7a**) and 298 K (**Figure 7b**). The $[HO]_{X\%}$-H_2P-COFs exhibited low capacities between 46 and 63 mg g^{-1} at 273 K and between 31 and 35 mg g^{-1} at 298 K (**Table 3**). By contrast, the $[HO_2C]_{X\%}$-H_2P-COFs exhibited dramatically increased CO_2 adsorption capacities. For example, $[HO_2C]_{100\%}$-H_2P-COF exhibited a capacity of 180 and 76 mg g^{-1} at 273 K (**Figure 7c**) and 298 K (**Figure 7d**), respectively. These capacities are 2.8- and 2.2-fold greater than those of $[HO]_{100\%}$-H_2P-COF (**Table 3**). Interestingly, the adsorption capacity of $[HO_2C]_{X\%}$-H_2P-COFs increased in proportion to their carboxylic acid content (**Figures 7c, d**; **Table 3**). These positive effects clearly confirmed the effectiveness of channel-wall functionalization in enhancing CO_2 adsorption.

Table 3. Porosity, CO_2 uptake, and Q_{st} value of $[HO]_{X\%}$-H_2P-COFs and $[HO_2C]_{X\%}$-H_2P-COFs.

H_2P-COFs	S_{BET} (m^2 g^{-1})	Pore Size (nm)	Pore Volume (cm^3 g^{-1})	CO_2 Uptake (mg g^{-1}) at 1 bar		Q_{st} (kJ mol^{-1})
				273 K	298 K	
$[HO]_{25\%}$	1054	2.5	0.89	54	31	32.2
$[HO]_{50\%}$	1089	2.5	0.91	46	34	29.4
$[HO]_{75\%}$	1153	2.5	0.96	52	32	31.5
$[HO]_{100\%}$	1284	2.5	1.02	63	35	36.4
$[HO_2C]_{25\%}$	786	2.2	0.78	96	58	38.2
$[HO_2C]_{50\%}$	673	1.9	0.66	134	67	39.6
$[HO_2C]_{75\%}$	482	1.7	0.54	157	72	41.2
$[HO_2C]_{100\%}$	364	1.4	0.43	174	76	43.5

Various 2D and 3D COFs with different structures have been previously synthesized and investigated in attempts to develop a practical scaffold for carbon dioxide adsorption. Typical examples include boronate-linked 2D COF-5 (5.9 wt%, S_{BET} = 1670 m^2 g^{-1}),[3c] TDCOF-5 (9.2

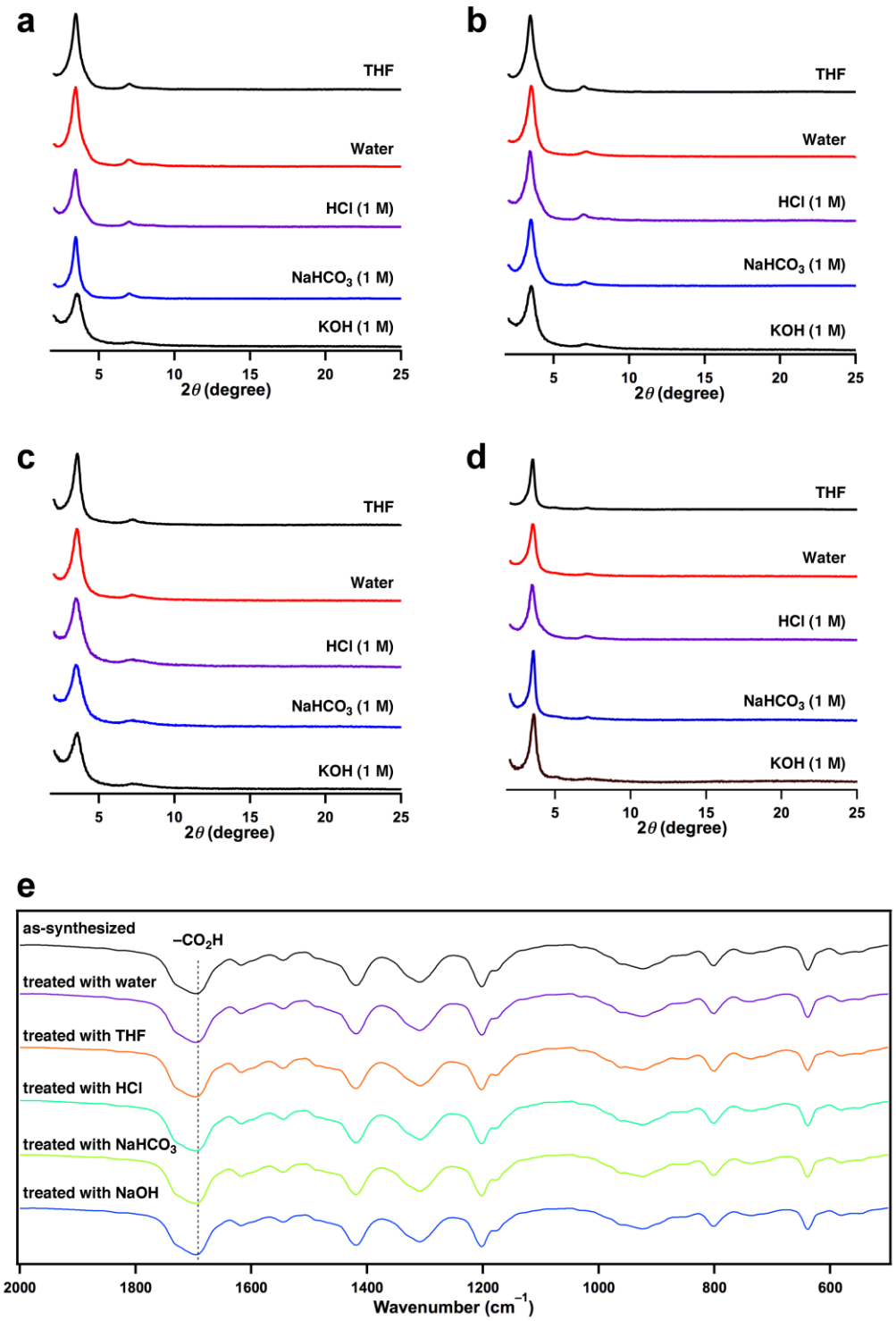

Figure 6. Stability test of $[HO_2C]_{X\%}$-H_2P-COFs. The XRD patterns of a) $[HO_2C]_{25\%}$-H_2P-COF, b) $[HO_2C]_{50\%}$-H_2P-COF, c) $[HO_2C]_{75\%}$-H_2P-COF, and d) $[HO_2C]_{100\%}$-H_2P-COF upon immersion in different solvents at room temperature for 24 h. (e) IR spectra of $[HO_2C]_{100\%}$-H_2P-COF and the $[HO_2C]_{100\%}$-H_2P-COF samples upon treatment with different solvents at room temperature for 24 h. These IR spectra revealed that the carboxylic acid groups were retained under these conditions.

wt%, S_{BET} = 2497 m^2 g^{-1}),[5a] and 3D COF-103 (7.6 wt%, S_{BET} = 3530 m^2 g^{-1}),[3c] imine-linked ILCOF-1 (6.0 wt%, S_{BET} = 2723 m^2 g^{-1})[5b] and TpPa-1 (15.6 wt%, S_{BET} = 535 m^2 g^{-1}),[3d] and azine-linked ACOF-1 (17.7 wt%, S_{BET} = 1176 m^2 g^{-1}).[2b] The capacity of $[HO]_{100\%}$-H_2P-COF (6.5 wt%) is close to those of conventional and non-functionalized COF-5, IL-COF-1, and COF-103. By contrast, the wall-channel functionalized $[HO_2C]_{100\%}$-H_2P-COF takes up 4.1 mmol g^{-1} of CO_2 (18.0 wt%, 180 mg g^{-1}, S_{BET} = 364 m^2 g^{-1}), which is the highest performance among 2D and 3D COFs reported thus far. To the best of my knowledge, the capacity observed for $[HO_2C]_{100\%}$-H_2P-COF is also comparable to those of other top-class members, including PPN-6-SO_3Li (187 mg g^{-1}),6g Amine-PCN-58 (128 mg g^{-1}),[6p] UCBZ-1 (99 mg g^{-1}),[6q] N-TC-EMC (176 mg g^{-1}),[6h] and PPN-6-CH_2DETA (190 mg g^{-1}).[6i]

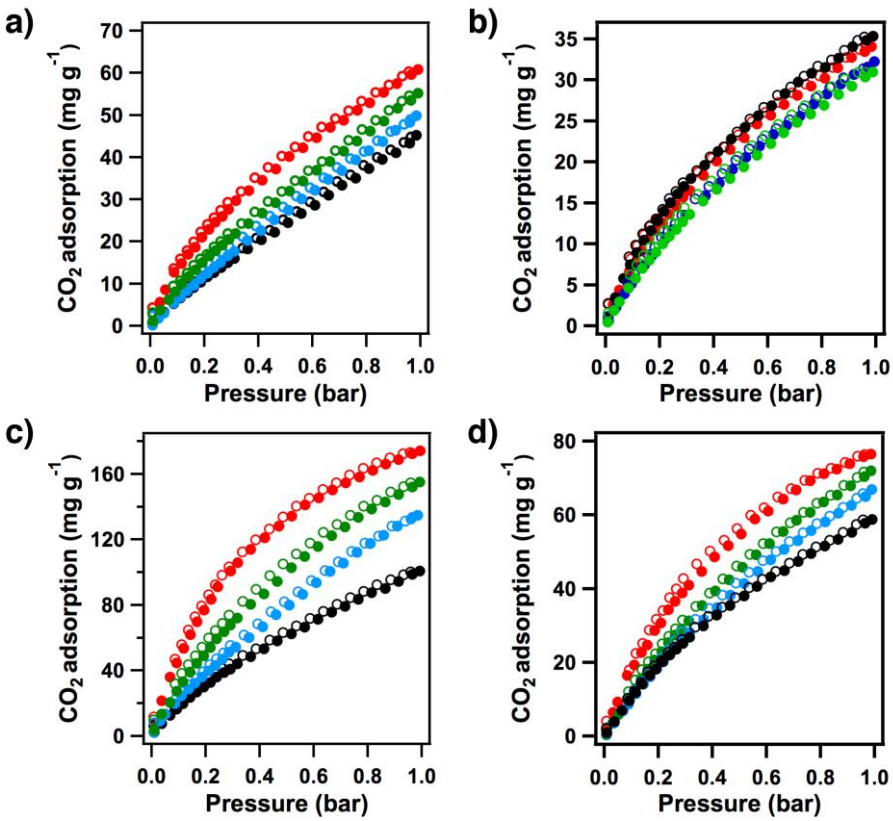

Figure 7. CO_2 sorption curves of $[HO]_{X\%}$-H_2P-COFs measured at (a) 273 K and (b) 298 K (black: $[HO]_{25\%}$-H_2P-COF, blue: $[HO]_{50\%}$-H_2P-COF, green: $[HO]_{75\%}$-H_2P-COF, red: $[HO]_{100\%}$-H_2P-COF). CO_2 sorption curves of $[HO_2C]_{X\%}$-H_2P-COFs measured at (c) 273 K and (d) 298 K (black: $[HO_2C]_{25\%}$-H_2P-COF, blue: $[HO_2C]_{50\%}$-H_2P-COF, green: $[HO_2C]_{75\%}$-H_2P-COF, red: $[HO_2C]_{100\%}$-H_2P-COF). Open and filled circles represent desorption and adsorption, respectively.

Upon functionalization with carboxylic acid groups that have affinity for carbon dioxide, $[HO_2C]_{100\%}$-H_2P-COF may exhibit enhanced adsorption selectivity. Based on the CO_2 and N_2 sorption isotherm curves measured at 298 K (**Figures 7, 8**), I investigated the selective adsorption of CO_2 over N_2, which is critical for carbon capture from air or flue gas streams. The ideal absorbed solution theory (IAST) of Myers and Prausnitz[7a] is a well-established model for describing the adsorption of gas mixtures in porous materials. Using pure-component isotherm fits, I determined the adsorption selectivity defined by $S_{ads} = (q_1/q_2)/(p_1/p_2)$ using the IAST method (SI). The accuracy of the IAST calculations for estimating the component loadings for several binary mixtures in a wide variety of porous materials has been established by comparison with Configurational-bias Monte Carlo (CBMC) simulations of mixture adsorption. I utilized

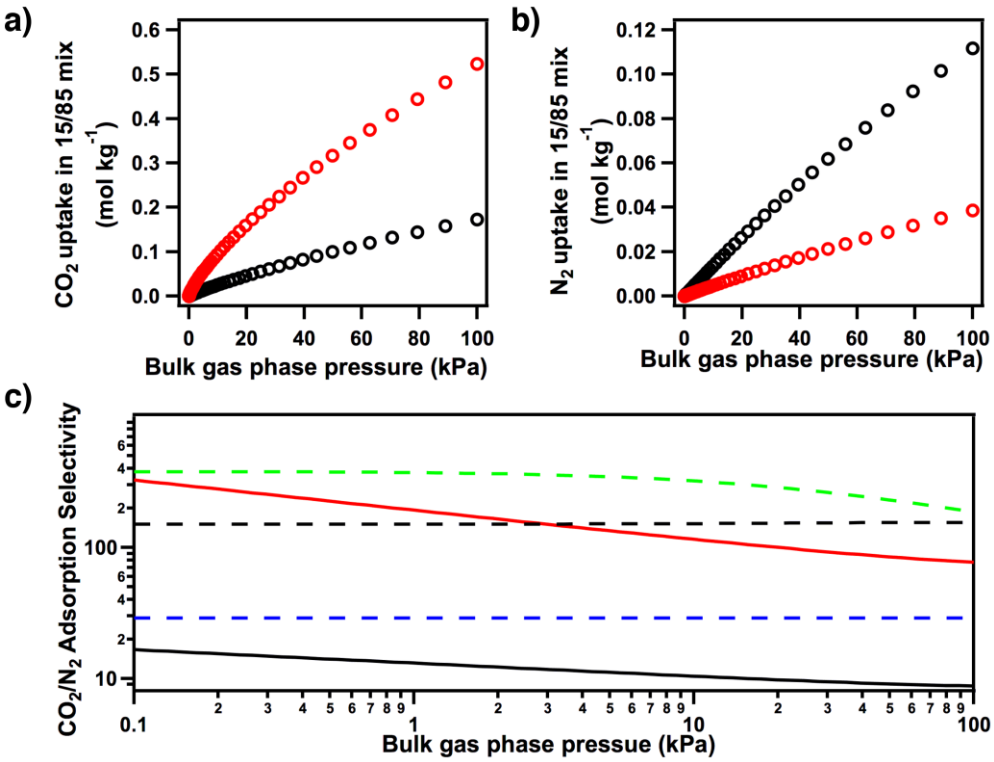

Figure 8. a) CO_2 and b) N_2 uptake by $[HO]_{100\%}$-H_2P-COF (black circles) and $[HO_2C]_{100\%}$-H_2P-COF (red circles) of a 15/85 CO_2/N_2 flue gas mixture at 298 K. c) CO_2/N_2 absorption selectivity of $[HO]_{100\%}$-H_2P-COF (black curve) and $[HO_2C]_{100\%}$-H_2P-COF (red curve) for the 15/85 CO_2/N_2 flue gas mixture at 298 K. The selectivities of NaX zeolite (broken blue curve), CuBTC (broken black curve), and MgMOF-74 (broken green curve) are shown for comparison.

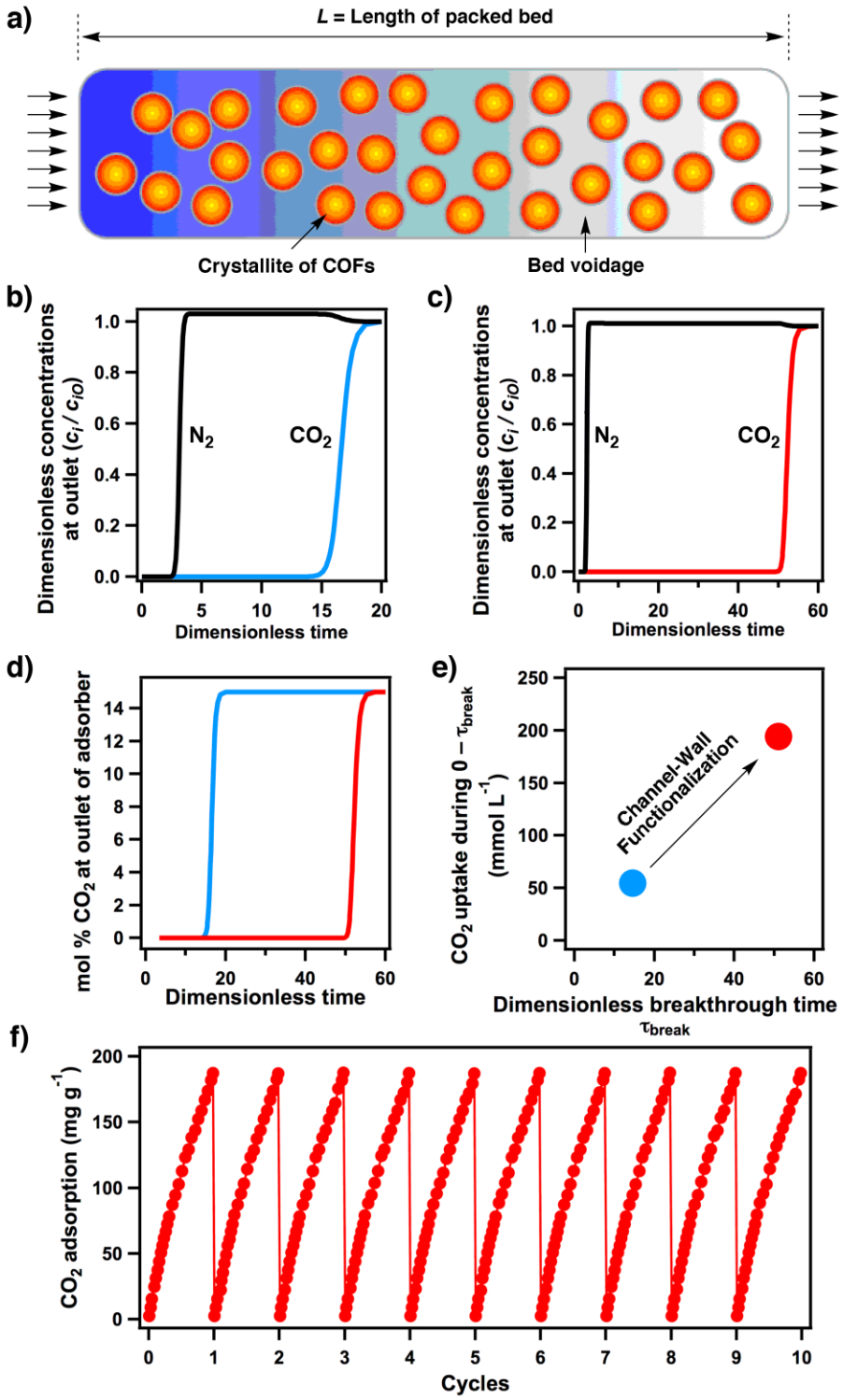

Figure 9. a) Fixed–bed adsorber for COFs. Flue gas breakthrough profiles of (b) $[HO]_{100\%}$-H_2P-COF and (c) $[HO_2C]_{100\%}$-H_2P-COF at 298 K. d) Comparison of $\%CO_2$ at the adsorber outlet at 298 K (blue curve: $[HO]_{100\%}$-H_2P-COF, red curve: $[HO_2C]_{100\%}$-H_2P-COF). e)

Comparison of CO_2 capture productivity at 298 K (blue spot: $[HO]_{100\%}$-H_2P-COF, red spot: $[HO_2C]_{100\%}$-H_2P-COF). f) Cycle test of $[HO_2C]_{100\%}$-H_2P-COF at 273 K.

$[HO]_{100\%}$-H_2P-COF and $[HO_2C]_{100\%}$-H_2P-COF for the separation of a CO_2/N_2 mixture that is relevant for CO_2 capture from flue gases and for my evaluation I assumed the CO_2/N_2 mixtures contained 15% CO_2 and 85% N_2, following the earlier work of Mason et al.[6l] **Figures 8a** and **8b** show the IAST calculation of CO_2 and N_2 uptake capacities for the 15/85 CO_2/N_2 mixture at 298 K. Notably, $[HO_2C]_{100\%}$-H_2P-COF exhibited a CO_2 uptake capacity of 0.51 mol kg^{-1} at 100 kPa (= 1 bar), whereas $[HO]_{100\%}$-H_2P-COF displayed an uptake of only 0.16 mol kg^{-1} (**Figure 8a**). By contrast, $[HO]_{100\%}$-H_2P-COF exhibited a N_2 uptake of 0.118 mol kg^{-1}, which is substantially greater than that of $[HO_2C]_{100\%}$-H_2P-COF (0.038 mol kg^{-1}, Figure 8b). These results clearly suggest that the functionalization of channel walls with carboxylic acid groups significantly enhances the CO_2 adsorption capacity of the flue mixture gas. **Figure 9c** presents the adsorption selectivity for the 15/85 CO_2/N_2 flue gas mixture, in comparison to those of CuBTC (a MOF),[6j] MgMOF-74,[6k-6n] and NaX zeolite.[6n,6o] At low pressures, such as 0.1 kPa, the adsorption selectivity S_{ads} was 323, which is greater than that of both CuBTC (broken black curve) and NaX zeolite (broken blue curve) and is close to that of MgMOF-74 (broken green curve). By contrast, $[HO]_{100\%}$-H_2P-COF exhibited a selectivity of only 18 at 0.1 kPa. At 100 kPa, $[HO_2C]_{100\%}$-H_2P-COF exhibited a selectivity of 77, whereas $[HO]_{100\%}$-H_2P-COF exhibited a selectivity of only 8. Notably, the selectivity of $[HO_2C]_{100\%}$-H_2P-COF is sufficiently high for potential practical use.

To clarify the nature of CO_2 adsorption, the isosteric heat of adsorption (Q_{st}) was calculated from the CO_2 adsorption isotherms measured at pressures up to 1 bar and at temperatures at 273 and 298 K. Interestingly, the Q_{st} value increased proportionally with the carboxylic acid content (**Table 3**). Therefore, the functionalized walls facilitate interactions with CO_2 and contribute to the enhanced performance. The Q_{st} value was 43.5 kJ mol^{-1} for $[HO_2C]_{100\%}$-H_2P-COF, which is compatible to that for MgMOF-74 and much higher than those for $[HO]_{100\%}$-H_2P-COF (34.5 kJ mol^{-1}), CuBTC, and NaX zeolite.

To evaluate the gas separation ability of adsorbents under kinetic flowing gas conditions, breakthrough simulations were performed using a precise methodology established by Krishna and Long.[7b] These simulations properly reflect the separation capability of a pressure-swing adsorption (PAS) process, which is an energetically efficient method for industrial-scale capture. The performance of a COF in a PSA unit is governed by both selectivity and capacity factors. **Figure 9a** presents a schematic of a packed-bed absorber. **Figures 9b** and **9c** show typical breakthrough curves for $[HO]_{100\%}$-H_2P-COF and $[HO_2C]_{X\%}$-H_2P-COF, respectively. The *x*-axis is dimensionless time, defined as dividing the actual time, τ, by the characteristic time, $L\varepsilon/\mu$. Clearly, $[HO_2C]_{100\%}$-H_2P-COF exhibited a breakthrough time of 50, which is much longer than that of $[HO]_{100\%}$-H_2P-COF (15). **Figure 9d** compares the breakthrough characteristics of COFs in terms of mole% CO_2 at the outlet as a function of dimensionless time for operation at a total pressure of 100 kPa. $[HO]_{100\%}$-H_2P-COF (red curve) has a breakthrough time much longer than that of $[HO]_{100\%}$-H_2P-COF (blue curve). Longer breakthrough times are desirable for greater CO_2 capture. For a quantitative evaluation of the COFs, I arbitrarily chose the required outlet gas purity to be <0.05 mol% CO_2. Using this purity specification, I determined the breakthrough times, τ_{break}, for each COF. On the basis of the material balance on the absorber, I determined the amount of CO_2 captured during the time interval 0-τ_{break}. **Figure 9e** presents a plot of the number of millimoles of CO_2 captured per *L* of adsorbent during the time interval 0-τ_{break} against the breakthrough time τ_{break}. Notably, $[HO_2C]_{100\%}$-H_2P-COF (red circle) exhibited superior CO_2 productivity compared with $[HO]_{100\%}$-H_2P-COF (black circle).

The aforementioned results indicate that channel-wall functionalization is efficient to convert a conventional COF into outstanding CO_2 adsorption materials; the effects of functional groups on carbon dioxide capture are positive and profound ranging from capacity to selectivity and productivity. To examine the cycle performance of $[HO_2C]_{100\%}$-H_2P-COF in terms of CO_2 uptake, I conducted temperature and vacuum swings with a Belsorp mini II analyzer by saturating the samples with CO_2 up to 1.0 bar at 273 K followed by placing the samples under high vacuum for 60 min at 353 K. Remarkably, after 10 cycles, no significant decline in uptake capacity was observed (**Figure 9f**), indicating complete desorption in each regeneration cycle and excellent cycling performance. These features assure a green process in regenerating the adsorbers.

Conclusion

In summary, I developed a strategy for converting a conventional 2D COF into an outstanding CO_2 capture scaffold via channel-wall functionalization. The high-throughput ring-opening reaction is useful for creating carboxylic acid functionalized channel walls while retaining layered and open porous structure. Given the rather limited room for increasing the porosity of 2D COFs, together with the availability of a broad diversity of different functional groups, I anticipate that the present channel-wall engineering strategy will be critical to exploring 2D COFs for high-performance gas storage and separation.

Experimental Sections

Methods Fourier transform Infrared (FT IR) spectra were recorded on a JASCO model FT IR-6100 infrared spectrometer. UV-Vis-IR diffuse reflectance spectrum (Kubelka-Munk spectrum) was recorded on a JASCO model V-670 spectrometer equipped with integration sphere model IJN-727. Powder X-ray diffraction (PXRD) data were recorded on a Rigaku model RINT Ultima III diffractometer by depositing powder on glass substrate, from $2\theta = 1.5°$ up to $60°$ with $0.02°$ increment. Elemental analysis was performed on a Yanako CHN CORDER MT-6 elemental analyzer. TGA measurements were performed on a Mettler-Toledo model TGA/SDTA851^e under N_2, by heating to 800 ℃ at a rate of 10 ℃ min^{-1}. Nitrogen sorption isotherms were measured at 77 K with a Bel Japan Inc. model BELSORP-mini II analyzer. Before measurement, the samples were degassed in vacuum at 120 ℃ for more than 10 h. By using the non-local density functional theory (NLDFT) model, the pore volume was derived from the sorption curve. ^{1}H NMR spectra were recorded on a JEOL model JNM-LA400 NMR spectrometer, where the chemical shifts (δ in ppm) were determined with a residual proton of the solvent as standard. Scanning electron microscopy (SEM) was carried out using solid samples on Hitachi Hitechnology C C model SU6600 and energy dispersive X-ray spectrometry (EDX) was recorded on Bruker AXS model using Quantax system with XFlash 6| 10 detector.

Materials and Synthetic Procedures

1-Butanol, *o*-dichlorobenzene (*o*-DCB), anhydrous acetone (99.5%), tetrahydrofuran, and acetic acid were purchased from Wako Chemicals. succinic anhydride and 1,4-phthalaldehyde (PA)

was purchased from TCI. Free-base 5,10,15,20-tetrakis(p-tetraphenylamino) porphyrin (H_2P) was prepared from *p*-nitrobenzaldehyde using a literature procedure.[9a] 2,5-Dihydroxyterephthala ldehyde (DHTA) was synthesized according to a reported method.[9b]

[HO]$_{X\%}$-H_2P-COFs. An *o*-DCB/BuOH/6 M AcOH mixture (5/5/1 by vol.; 1.1 mL) of H_2P (0.02 mmol, 13.48 mg) and DHTA/PA (total 0.04 mmol) at different molar ratios of 25/75, 50/50, 75/25, and 100/0 was degassed in a Pyrex tube (10 mL) by three freeze-pump-thaw cycles. The tube was sealed off and heated at 120 ℃ for three days. The precipitate was collected by centrifugation, washed with anhydrous THF for five times, and washed with acetone twice. The powder was dried at 120 ℃ under vacuum overnight to give the corresponding product in isolated yields of 78%, 75%, 84%, and 82% for [HO]$_{25\%}$-H_2P-COF, [HO]$_{50\%}$-H_2P-COF, [HO]$_{75\%}$-H_2P-COF, and [HO]$_{100\%}$-H_2P-COF, respectively.

[HO$_2$C]$_{X\%}$-H_2P-COFs. [HO]$_{X\%}$-H_2P-COFs (30 mg) was weighed into a 10-mL glass vial, to which succinic anhydride (6 mL, 1.0 M solution in anhydrous acetone) was added. The reaction mixture was heated at 60 ℃ for two days. The precipitate was collected by centrifugation, washed with anhydrous THF for five times. The crude product was rinsed with THF for 48 h using a Soxhlet extractor. The powder was dried at 100 ℃ under vacuum overnight to give the corresponding products of [HO$_2$C]$_{25\%}$-H_2P-COF, [HO$_2$C]$_{50\%}$-H_2P-COF, [HO$_2$C]$_{75\%}$-H_2P-COF, and [HO$_2$C]$_{100\%}$-H_2P-COF, quantitatively.

Hydrolysis of [HO$_2$C]$_{X\%}$-H_2P-COFs. The [HO$_2$C]$_{X\%}$-H_2P-COFs (100 mg) sample were hydrolyzed by refluxing in a THF/H_2O (2/1 by vol., 24 mL) solution of KOH (3 M) for 5 days. After filtration, 5 mL of aqueous HCl solution (6 M) was added slowly to the filtrate and the mixture was stirred for 1 h. The greenish porphyrin precipitate was removed by filtration. The filtrate was evaporated under vacuum and submitted to ^{1}H NMR spectroscopy in d_6-DMSO.

Fitting of pure component isotherms

The salient properites of two different COFs ([HO]$_{100\%}$-H_2P-COF and [HO$_2$C]$_{100\%}$-H_2P-COF) are specified in **Table 4**. The potential of these COFs are evaluated for the separation of CO_2/N_2 mixtures that is relevant for CO_2 capture from flue gases. For my evaluations, I assume the CO_2/N_2 mixtures to contain 15% CO_2, and 85% N_2, following the earlier work of Mason et al.[8a]

The experimentally measured excess loadings of CO_2, and N_2, obtained at different temperatures, were first converted to absolute loadings before data fitting. The procedure for converting to absolute loadings is the same as described in the Supporting Information accompanying the paper of Wu et al.[8b] For the purpose of converting to absolute loadings, the pore volumes used are specified in **Table 5**. The isotherm data for CO_2 were fitted with the Langmuir-Freundlich model:

$$q = q_{sat}\frac{bp^{\nu}}{1+bp^{\nu}} \quad (1)$$

with *T*-dependent parameter *b*

$$b_A = b_0 \exp\left(\frac{E}{RT}\right) \quad (2)$$

The Langmuir-Freundlich parameters for adsorption of CO_2 are provided in **Table 6**. The simpler Langmuir model was adequate for fitting the isotherm data for N_2; Table S6 provides the *T*-dependent Langmuir parameters for N_2 in different materials

Table 4. Salient properties of $[HO]_{100\%}$-H_2P-COF and $[HO_2C]_{100\%}$-H_2P-COF (The crystal framework densities, required in the breakthrough simulations, are estimated as (bulk density)/(one-bed porosity) with the assumption that the bed porosity is 0.4)

COFs	Bulk density (g cm^{-3})	S_{BET} (m^2 g^{-1})	Pore volume (cm^3 g^{-1})	Pore size (nm)
$[HO]_{100\%}$-H_2P-COF	0.24	1186	0.78	2.54
$[HO_2C]_{100\%}$-H_2P-COF	0.26	326	0.49	1.56

Table 5. Langmuir-Freundlich parameters for adsorption of CO_2 in COFs (The experimentally measured excess loadings were first converted to absolute loadings before data fitting.)

COFs	q_{sat} (mol kg^{-1})	b_0 (Pa^{-v})	E (kJ mol^{-1})	n (dimensionless)
$[HO]_{100\%}$-H_2P-COF	2.2	1.4×10^{-11}	34.6	0.9
$[HO_2C]_{100\%}$-H_2P-COF	7.7	6.04×10^{-11}	33.5	0.77

Table 6. One-site Langmuir parameters for N_2 in different materials

COFs	$q_{A,sat}$ (mol kg^{-1})	b_{A0} (Pa^{-1})	E_A (kJ mol^{-1})
$[HO]_{100\%}$-H_2P-COF	1.2	6.14×10^{-12}	30.7
$[HO_2C]_{100\%}$-H_2P-COF	2	2.38×10^{-11}	23.9

2.4.4 Isosteric heat of adsorption

The isosteric heat of adsorption, Q_{st}, defined as

$$Q_{st} = RT^2\left(\frac{\partial \ln p}{\partial T}\right)_q \quad (3)$$

was determined using the pure component isotherm fits using the Clausius-Clapeyron equation.

2.4.5 IAST calculations

The selectivity of preferential adsorption of component 1 over component 2 in a mixture containing 1 and 2, perhaps in the presence of other components too, can be formally defined as

$$S_{ads} = \frac{q_1 / q_2}{p_1 / p_2} \quad (4)$$

In equation (4), q_1 and q_2 are the *absolute* component loadings of the adsorbed phase in the mixture. These component loadings are also termed the uptake capacities. In all the calculations to be presented below, the calculations of q_1 and q_2 are based on the use of the Ideal Adsorbed Solution Theory (IAST) of Myers and Prausnitz.[8c] The accuracy of the IAST calculations for estimation of the component loadings for several binary mixtures in a wide variety of zeolites, and MOFs has been established by comparison with Configurational-Bias Monte Carlo (CBMC) simulations of mixture adsorption.[8d-i]

2.4.6 Simulation methodology for transient breakthrough in fixed bed absorbers

The separation of CO_2/N_2 mixtures is commonly carried out in fixed bed absorbers in which the separation performance is dictated by a combination of three separate factors: (a) adsorption selectivity, (b) uptake capacity, and (c) intra-crystalline diffusivities of guest molecules within the pores. Transient breakthrough simulations are required for a proper evaluation of MOFs; the simulation methodology used in my work is described in earlier publications.[8j,8k] A brief summary of the simulation methodology is presented below.

Assuming plug flow of an *n*-component gas mixture through a fixed bed maintained under isothermal conditions (see schematic in **Figure 9a**), the partial pressures in the gas phase at any position and instant of time are obtained by solving the following set of partial differential equations for each of the species *i* in the gas mixture.[8l]

$$\frac{1}{RT}\frac{\partial p_i(t,z)}{\partial t} = -\frac{1}{RT}\frac{\partial\left(v(t,z)p_i(t,z)\right)}{\partial z} - \frac{\left(1-\varepsilon\right)}{\varepsilon}\rho\frac{\partial \bar{q}_i(t,z)}{\partial t}; \qquad i = 1,2,\ldots n \qquad (5)$$

In equation (5), t is the time, z is the distance along the adsorber, r is the framework density, e is the bed voidage, v is the interstitial gas velocity, and $\bar{q}_i(t,z)$ is the *spatially averaged* molar loading within the crystallites of radius r_c, monitored at position z, and at time t.

At any time t, during the transient approach to thermodynamic equilibrium, the spatially averaged molar loading within the crystallite r_c is obtained by integration of the radial loading profile

$$\bar{q}_i(t) = \frac{3}{r_c^3}\int_0^{r_c} q_i(r,t)r^2 dr \qquad (6)$$

For transient unary uptake within a crystal at any position and time with the fixed bed, the radial distribution of molar loadings, q_i, within a spherical crystallite, of radius r_c, is obtained from a solution of a set of differential equations describing the uptake

$$\frac{\partial q_i(r,t)}{\partial t} = -\frac{1}{\rho}\frac{1}{r^2}\frac{\partial}{\partial r}\left(r^2 N_i\right) \qquad (7)$$

The molar flux N_i of component *i* is described by the simplified version of the Maxwell-Stefan equations in which both correlation effects and thermodynamic coupling effects are considered to be of negligible importance

$$N_i = -\rho D_i \frac{\partial q_i}{\partial r} \qquad (8)$$

Summing equation (**6**) over all *n* species in the mixture allows calculation of the *total average* molar loading of the mixture within the crystallite

$$\bar{q}_t(t,z) = \sum_{i=1}^{n} \bar{q}_i(t,z) \qquad (9)$$

The *interstitial* gas velocity is related to the *superficial* gas velocity by

$$v = \frac{u}{\varepsilon} \qquad (10)$$

In industrial practice, the most common operation uses a step-wise input of mixtures to be separated into an absorber bed that is initially free of adsorbents, i.e. I have the initial condition

$$t = 0; \quad q_i(0,z) = 0 \qquad (11)$$

At time $t = 0$, the inlet to the absorber, $z = 0$, is subjected to a step input of the *n*-component gas mixture and this step input is maintained till the end of the adsorption cycle when steady-state conditions are reached.

$$t \geq 0; \quad p_i(0,t) = p_{i0}; \quad u(0,t) = u_0 \qquad (12)$$

where u_0 is the superficial gas velocity at the inlet to the absorber.

The breakthrough characteristics for any component is essentially dictated by two sets of parameters: (a) The characteristic contact time between the crystallites and the surrounding fluid phase, and (b), that reflect the importance of intra-crystalline diffusion limitations. It is common to use the dimensionless time, obtained by dividing the actual time *t*, by the characteristic time, when plotting simulated breakthrough curves.

If the value of is large enough to ensure that intra-crystalline gradients are absent and the entire crystallite particle can be considered to be in thermodynamic equilibrium with the surrounding bulk gas phase at that time *t*, and position *z* of the adsorber

$$\bar{q}_i(t,z) = q_i(t,z) \quad (13)$$

The molar loadings at the *outer surface* of the crystallites, i.e. at $r = r_c$, are calculated on the basis of adsorption equilibrium with the bulk gas phase partial pressures p_i at that position *z* and time *t*. The adsorption equilibrium can be calculated on the basis of the IAST. The assumption of thermodynamic equilibrium at every position *z*, and any time *t*, i.e. invoking Equation (10), generally results in sharp breakthroughs for each component. Sharp breakthroughs are desirable in practice because this would result in high productivity of pure products. Essentially, the influence of intra-crystalline diffusion is to reduce the productivity of pure gases. For all the breakthrough calculations reported in this work, I assume negligible diffusion resistances for all materials and I invoke the simplified Equation (10).

Notation

b_A	dual-Langmuir-Freundlich constant for species *i* at adsorption site A,
c_i	molar concentration of species *i* in gas mixture, mol m^{-3}
c_{i0}	molar concentration of species *i* in gas mixture at inlet to adsorber, mol m^{-3}
L	length of packed bed adsorber, m
N	number of species in the mixture, dimensionless
N_i	molar flux of species *i*, mol m^{-2} s^{-1}
p_i	partial pressure of species *i* in mixture, Pa
p_t	total system pressure, Pa
q_i	component molar loading of species *i*, mol kg^{-1}
$\bar{q}_i(t,z)$	*spatially averaged* component molar loading of species *i*, mol kg^{-1}
r_c	radius of crystallite, m
R	gas constant, 8.314 J mol^{-1} K^{-1}
t	time, s
T	absolute temperature, K
u	superficial gas velocity in packed bed, m s^{-1}
v	interstitial gas velocity in packed bed, m s^{-1}

Greek letters

e	voidage of packed bed, dimensionless
r	framework density, kg m^{-3}
	time, dimensionless

Subscripts

i	referring to component
i_{break}	referring to breakthrough
t	referring to total mixture

References

1. a) X. Feng, X. S. Ding, D. Jiang, *Chem. Soc. Rev.* **2012**, *41*, 6010-6022; b) M. Dogru, T. Bein, *Chem. Commun.* **2014**, *50*, 5531-5546.
2. a) A. Nagai, Z. Guo, X. Feng, S. Jin, X. Chen, X. Ding, D. Jiang, *Nature Commun.* **2011**, *2*, 536; b) X. Feng, L. Liu, Y. Honsho, A. Saeki, S. Seki, S. Irle, Y. Dong, A. Nagai, D. Jiang, *Angew. Chem. Int. Ed.* **2012**, *51*, 2618-2622; c) Z. Li, X. Feng, Y. Zou, Y. Zhang, H. Xia, X. Liu, Y. Mu, *Chem. Commun.* **2014**, *50*, 13825-13828; d) H. Xu, X. Chen, J. Gao, J. Lin, M. Addicoat, S. Irle, D. Jiang, *Chem. Commun.* **2014**, *50*, 1292-1294.
3. a) H. Furukawa, O. M. Yaghi, *J. Am. Chem. Soc.* **2009**, *131*, 8875-8883; b) C. J. Doonan, D. J. Tranchemontagne, T. G. Glover, J. R. Hunt, O. M. Yaghi, *Nature Chem.* **2010**, *2*, 235-238; c) S. Kandambeth, D. B. Shinde, M. K. Panda, B. Lukose, T. Heine, R. Banerjee, *Angew. Chem. Int. Ed.* **2013**, *52*, 13052-13056; d) S. Chandra, S. Kandambeth, B. P. Biswal, B. Lukose, S. M. Kunjir, M. Chaudhary, R. Babarao, T. Heine, R. Banerjee, *J. Am. Chem. Soc.* **2013**, *135*, 17853-17861; e) L. Stegbauer, K. Schwinghammer, B. V. Lotsch, *Chem. Sci.* **2014**, *5*, 2789-2793.
4. a) D. N. Bunck, W. R. Dichtel, *Angew. Chem. Int. Ed.* **2012**, *51*, 1855-1859; b) D. N. Bunck, W. R. Dichtel. *Chem. Commun.* **2013**, *49*, 2457-2459; c) Q. Fang, Z. Zhuang, S. Gu, R. B. Kaspar, J. Zheng, J. Wang, S. Qiu, Y. Yan. *Nature Commun.* **2014**, *5*, doi: 10.1038/ncomms5503.
5. a) Z. Kahveci, T. Islamoglu, G. A. Shar, R. Ding, H. M. El-Kaderi, *CrystEngComm* **2013**, *15*, 1524-1527; b) M. G. Rabbani, A. K. Sekizkardes, Z. Kahveci, T. E. Reich, R. Ding, H. M. El-Kaderi, *Chem. Eur. J.* **2013**, *19*, 3324-3328.
6. a) S. Cavenati, C. A. Grande, A. E. Rodrigues, *J. Chem. Eng. Data* **2004**, *49*, 1095-1101; b) N. Hiyoshi, K. Yogo, T. Yashima, *Microporous Mesoporous Mater.* **2005**, *84*, 357-365; c) Y. Belmabkhout, G. Pirngruber, E. Jolimaitre, A. Methivier, *Adsorption* **2007**, *13*, 341-349; d) S. R. Caskey, A. G. Wong-Foy, A. J. Matzger, *J. Am. Chem. Soc.* **2008**, *130*, 10870-10871; e) J. C. Hicks, J. H. Drese, D. J. Fauth, M. L. Gray, G. Qi, C. W. Jones, *J. Am. Chem. Soc.* **2008**, *130*, 2902-2903; f) G. T. Rochelle, *Science* **2009**, *325*, 1652-1654; g) T. Gadzikwa, O. K. Farha, K. L. Mulfort, J. T. Hupp, S. T. Nguyen, *Chem. Commun.* **2009**, 3720-3722; h) P. D. C. Dietzel, V.

Besikiotisa, R. Blom, *J. Mater. Chem.* **2009**, *19*, 7362-7370; i) A. Torrisi, R. G. Bell, C. Mellot-Draznieks, *Cryst. Growth Des.* **2010**, *10*, 2839-2841; j) R. Dawson, D. J. Adams, A. I. Cooper, *Chem. Sci.* **2011**, *2*, 1173-1177; k) W. Lu, D. Yuan, J. Sculley, D. Zhao, R. Krishna, H. C. Zhou, *J. Am. Chem. Soc.* **2011**, *133*, 18126-18129; l) J. A. Mason, K. Sumida, Z. R. Herm, R. Krishna, J. R. Long, *Energy Environ. Sci.* **2011**, *4*, 3030-3040; m) L. Wang, R. T. Yang, *J. Phys. Chem.* C **2012**, *116*, 1099-1106; n) W. Lu, J. P. Sculley, D. Yuan, R. Krishna, Z. Wei, H. C. Zhou, *Angew. Chem. Int. Ed.* **2012**, *51*, 7480-7484; o) P. Chowdhury, S. Mekala, F. Dreisbach, S. Gumma, *Microporous Mesoporous Mater.* **2012**, *152*, 246-252; p) H. Jiang, D. Feng, T. Liu, J. Li, H. Zhou, *J. Am. Chem. Soc.* **2012**, *134*, 14690-14693; q) Y. Zhu, W. Zhang, *Chem. Sci.* **2014**, *5*, 4957-4961.

7. a) A. L. Myers, J. M. Prausnitz, *AIChE Journal* **1965**, *11*, 121-127; b) R. Krishna, J. R. Long, *J. Phys. Chem.* C **2011**, *115*, 12941-12950.
8. a) A. L. Myers, J. M. Prausnitz, *A.I.Ch.E.J.* **1965**, *11*, 121; b) M. Yuasa, K. Oyaizu, A. Yamaguchi, M. Kuwakado *J. Am. Chem. Soc.* **2004**, *126*, 11128; c) R. Krishna, J. M. van Baten, *Chem. Eng. J.* **2007**, *133*, 121; d) R. Krishna, J. M. van Baten, *J. Membr. Sci.* **2010**, *360*, 323; e) J. A. Mason, K. Sumida, Z. R. Herm, R. Krishna, J. R. Long, *Energy Environ. Sci.* **2011**, *4*, 3030; f) R. Krishna, J. M. van Baten, Phys. *Chem. Chem. Phys.* **2011**, *13*, 10593; g) R. Krishna, J. M. van Baten, *J. Membr. Sci.* **2011**, *383*, 289; h) R. Krishna, J. M. van Baten, *J. Membr. Sci.* **2011**, *377*, 249; i) R. Krishna, J. R. Long, *J. Phys. Chem.* C **2011**, *115*, 12941; j) H. Wu, K. Yao, Y. Zhu, B. Li, Z. Shi, R. Krishna, J. Li, *J. Phys. Chem.* C **2012**, *116*, 16609; k) R. Krishna, J. M. van Baten, *Chem. Eng. Sci.* **2012**, *69*, 684; l) U. S. Hiremath, *Tetrahedron Letters* **2013**, *54*, 3419.
9. a) M. Yuasa, K. Oyaizu, A. Yamaguchi, M. Kuwakado *J. Am. Chem. Soc.* **2004**, *126*, 11128; b) U. S. Hiremath, *Tetrahedron Letters* **2013**, *54*, 3419.

Chapter 2

Tailor-Made Pore Surface Engineering in Covalent Organic Frameworks: Systematic Functionalization for Performance Screening

J. Am. Chem. Soc., **2015**, *137*, 7079-7082.

Ning Huang, Rajamani Krisna and Donglin Jiang

Abstract: Imine-linked covalent organic frameworks (COFs) were synthesized to bear content-tunable, accessible, and reactive ethynyl groups on the walls of one-dimensional pores. These COFs offer an ideal platform for pore-wall surface engineering aimed at anchoring diverse functional groups ranging from hydrophobic to hydrophilic units and from basic to acidic moieties with controllable loading contents. This approach enables the development of various tailor-made COFs with systematically tuned porosities and functionalities while retaining the crystallinity. We demonstrate that this strategy can be used to efficiently screen for suitable pore structures for use as CO_2 adsorbents. The pore-surface-engineered walls exhibit an enhanced affinity for CO_2, resulting in COFs that can capture and separate CO_2 with high performance.

Keywords: carbon dioxide; covalent organic frameworks; flue gas separation; gas adsorption; surface engineering

Introduction

Covalent organic frameworks (COFs) are an emerging class of crystalline porous polymers with pre-designable porous structure.[1] The ordered open channels found in two-dimensional (2D) COFs could render them able to adsorb CO_2. However, the COFs' dense layer architecture results in low porosity that has thus far restricted their potential for CO_2 adsorption.[2-7] Here, we describe the use of pore surface engineering to overcome these limitations by anchoring functional groups to the pore walls to enhance the affinity of the COFs for CO_2. This method integrates a variety of functionalities with controllable loading contents onto the pore walls, which efficiently screen for structures that are suitable for CO_2 capture. Among various types of COFs, imine-linked COFs are stable under various conditions, making them attractive for CO_2 adsorption.[2d, 2f, 5, 6e] However, conventional imine-linked COFs usually exhibit low CO_2 capacities. The conversion of imine-linked COFs into high-performance CO_2-adsorption materials is highly desired but has yet to be fully explored.

Results and Discussions

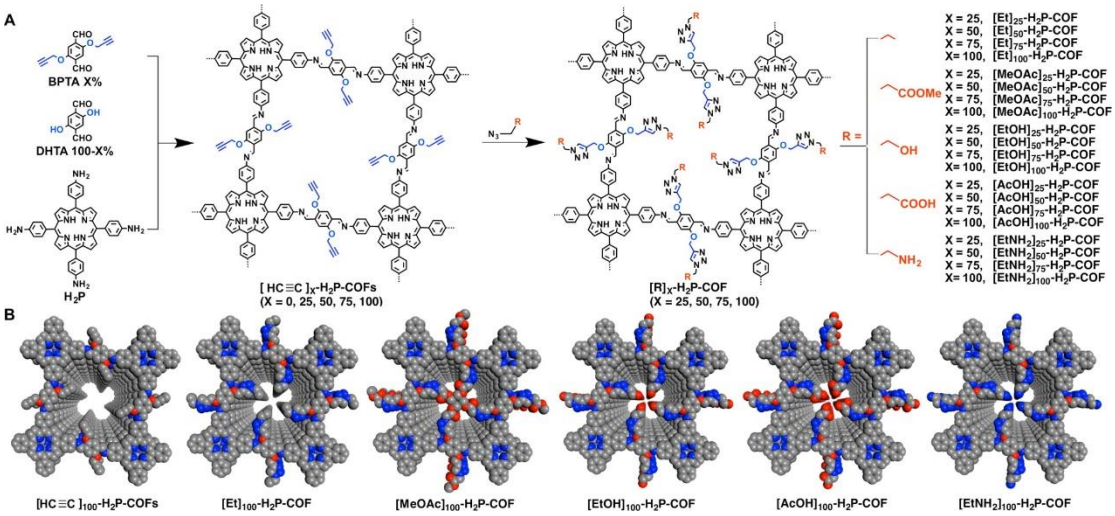

Scheme 1. (A) Schematic of Pore Surface Engineering of Imine-Linked COFs with Various Functional Groups via Click Reactions; (B) Pore Structures of COFs with Different Functional Groups (Gray, C; Blue, N; Red, O).

We utilized a mesoporous imine-linked porphyrin COF with a low capacity for CO_2 adsorption as a scaffold (**Scheme 1**). We developed a three-component reaction system consisting of 5,10,15,20-tetrakis(p-tetraphenylamino)porphyrin and a mixture of 2,5-bis(2- propynyloxy

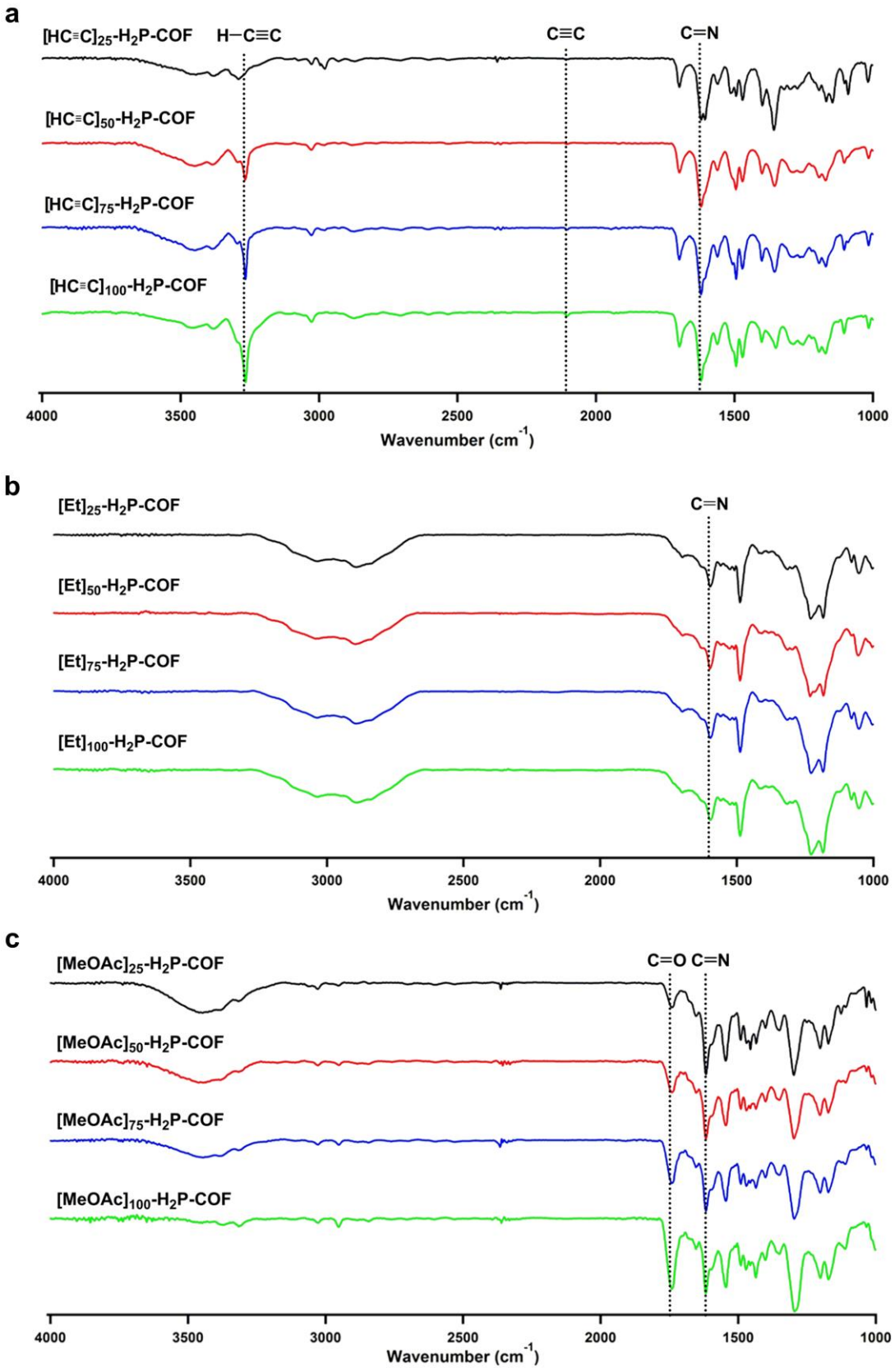
a
[HC≡C]25-H2P-COF
H—C≡C
C≡C
C=N
[HC≡C]50-H2P-COF
[HC≡C]75-H2P-COF
[HC≡C]100-H2P-COF
4000
3500
3000
2500
2000
1500
1000
Wavenumber (cm-1)
b
[Et]25-H2P-COF
C=N
[Et]50-H2P-COF
[Et]75-H2P-COF
[Et]100-H2P-COF
4000
3500
3000
2500
2000
1500
1000
Wavenumber (cm-1)
c
[MeOAc]25-H2P-COF
C=O C=N
[MeOAc]50-H2P-COF
[MeOAc]75-H2P-COF
[MeOAc]100-H2P-COF
4000
3500
3000
2500
2000
1500
1000
Wavenumber (cm-1)

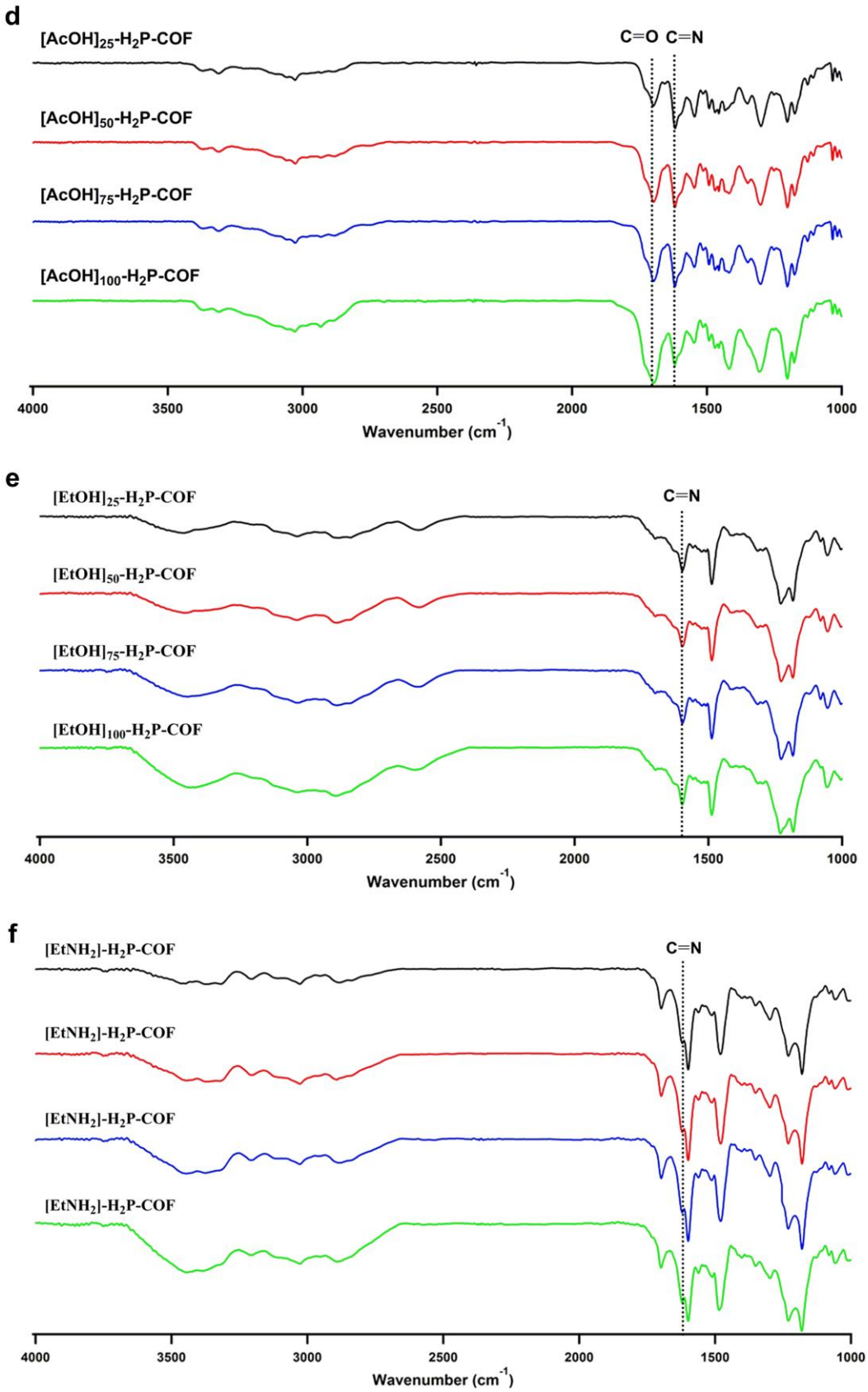

Figure 1. FT-IR spectra of $[HC{\equiv}C]_x$-H_2P-COFs, $[Et]_x$-H_2P-COFs, $[MeOAc]_x$-H_2P-COFs, $[AcOH]_x$-H_2P-COFs, $[EtOH]_x$-H_2P-COFs and $[EtNH_2]_x$-H_2P-COFs (X = 25, 50, 75, and 100).

terephthalaldehyde (BPTA) and 2,5-dihydroxyterephthalaldehyde (DHTA) at various molar ratios (X = [BPTA]/([BPTA] + [DHTA]) × 100 = 0, 25, 50, 75, and 100) for the synthesis of four COFs with different ethynyl contents on their edges (**Scheme 1**, $[HC{\equiv}C]_X$-H_2P-COFs, X = 25, 50, 75, and 100). Quantitative click reactions between the ethynyl units and azide compounds were performed to anchor the desired groups onto the pore walls (**Scheme 1**). We synthesized 20 different COFs with pores functionalized with a variety of functional groups, including ethyl, acetate, hydroxyl, carboxylic acid, and amino groups; these groups ranged from hydrophobic to hydrophilic and from basic to acidic (**Scheme 1**, $[R]_X$-H_2P-COFs ($[Et]_X$-H_2P-COFs, $[MeOAc]_X$-H_2P-COFs, $[EtOH]_X$-H_2P-COFs, $[AcOH]_X$-H_2P-COFs, $[EtNH_2]_X$-H_2P-COFs)).

Infrared (IR) spectroscopy provides direct evidence for the presence of ethynyl units in $[HC{\equiv}C]_X$-H_2P-COFs and functionalized groups in $[R]_X$-H_2P-COFs (**Figure 1**).[3a] Elemental analysis revealed that the actual ethynyl and functional unit contents of the COFs were close to the calculated values. X-ray diffraction (XRD) measurements revealed that $[HC{\equiv}C]_X$-H_2P-COFs and H_2P-COF exhibited the same XRD pattern, thereby demonstrating that the crystal structure of H_2P-COF was retained. The pore-surface-engineered COFs also exhibited the same XRD patterns as H_2P-COF, indicating that the crystalline framework was retained. **Scheme 1B** presents the pore structures of $[HC{\equiv}C]_{100}$-H_2P-COF, $[Et]_{100}$-H_2P-COF, $[MeOAc]_{100}$-H_2P-COF, $[EtOH]_{100}$-H_2P-COF, $[AcOH]_{100}$-H_2P-COF, and $[EtNH_2]_{100}$-H_2P-COF. The porous structures of these COFs can be fully changed through the integration of different functional groups.

Nitrogen sorption isotherms were collected at 77 K to investigate the porosity of the COFs (**Figure 2**). The $[HC{\equiv}C]_X$-H_2P-COFs exhibited Brunauer-Emmett-Teller (BET) surface areas of 1474, 1413, 962, 683, and 462 $m^2\ g^{-1}$, corresponding to ethynyl content (X) of 0, 25, 50, 75, and 100, respectively. This trend indicates that the ethynyl groups occupied the pore space. As a result, the pore volume decreased from 0.75 to 0.71, 0.57, 0.42, and 0.28 $cm^3\ g^{-1}$, respectively. Notably, these COFs contained only one type of pore in the framework (**Figure 3**), indicating that the ethynyl units were randomly integrated into the pore walls of $[HC{\equiv}C]_X$-H_2P-COFs (X = 25, 50, and 75). The pore size decreased from 2.5 to 2.3, 2.1, 1.9, and 1.6 nm as the X value was increased from 0 to 25, 50, 75, and 100, respectively.

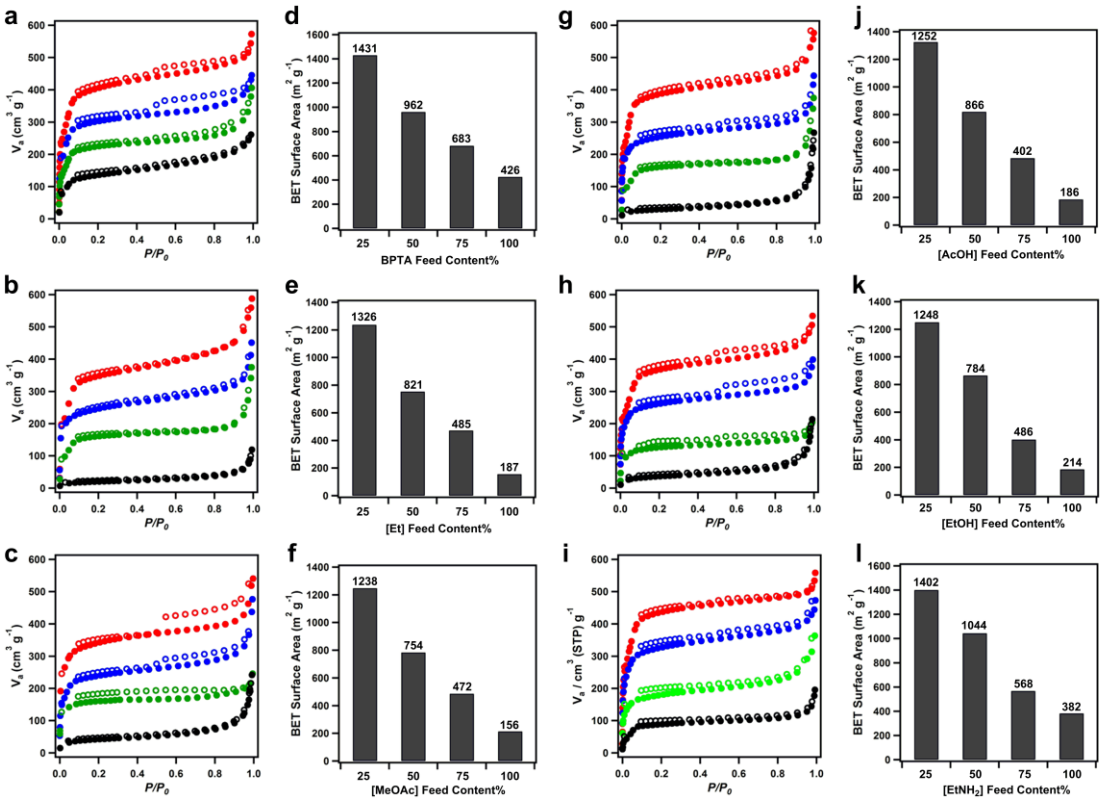

Figure 2. Nitrogen sorption isotherm curves of $[HC{\equiv}C]_x$-H_2P-COFs (**a,** red: 25, blue: 50, green: 75, black: 100), $[Et]_x$-H_2P-COFs (**b**), $[MeOAc]_x$-H_2P-COFs (**c**), $[AcOH]_x$-H_2P-COFs (**g**), $[EtOH]_x$-H_2P-COFs (**h**) and $[EtNH_2]_x$-H_2P-COFs (**i**) at 77K.

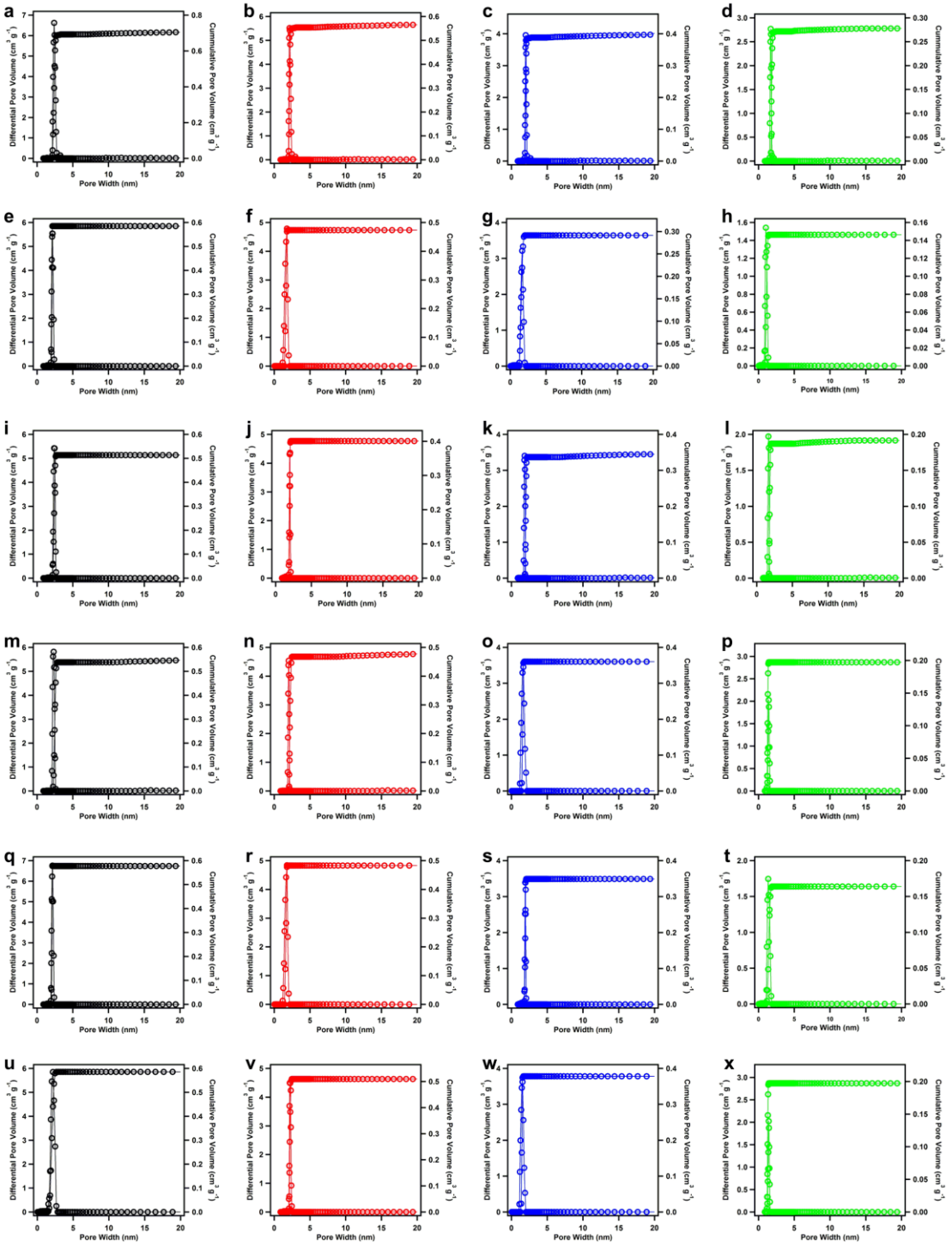

Figure 3. Pore size and pore volume distribution files for $[HC{\equiv}C]_x$-H_2P-COFs (**a-d**), $[Et]_x$-H_2P-COFs (**e-h**), $[MeOAc]_x$-H_2P-COFs (**i-l**), $[AcOH]_x$-H_2P-COFs (**m-p**), $[EtOH]_x$-H_2P-COFs (**q-t**) and $[EtNH_2]_x$-H_2P-COFs (**u-x**, X = 25, 50, 75, and 100).

Compared to $[HC{\equiv}C]_X$-H_2P-COFs, the $[Et]_X$-H_2P-COFs with the same X value exhibited more explicit decrease in their BET surface areas, pore volumes, and pore sizes (**Figure 3**).

These decrease resulted from the occupation of the pores by longer chains that were integrated via pore surface engineering (**Scheme 1B**). For example, for $[Et]_{25}$-H_2P-COF, $[Et]_{50}$-H_2P-COF, $[Et]_{75}$-H_2P-COF, and $[Et]_{100}$-H_2P-COF, the BET surface areas were 1326, 821, 485, and 187 $m^2\ g^{-1}$, and the pore volumes were 0.55, 0.48, 0.34, and 0.18 $cm^3\ g^{-1}$, respectively. The pore surface engineering steadily decreased the pore size from a mesopore to supermicropores, allowing the systematic tuning of the pore sizes from 2.2 to 1.9, 1.6, and 1.5 nm. Such fine adjustments of the pore size have not been achieved via direct polycondensation. Upon pore-wall engineering with ester, hydroxyl, carboxylic acid, and amino groups, the BET surface areas, pore volumes, and pore sizes of the resulting $[MeOAc]_X$-H_2P-COFs, $[EtOH]_X$-H_2P-COFs, $[AcOH]_X$-H_2P-COFs, and $[EtNH_2]_X$-H_2P-COFs exhibited similar tendencies to decrease compared to those of the $[Et]_X$-H_2P-COFs.

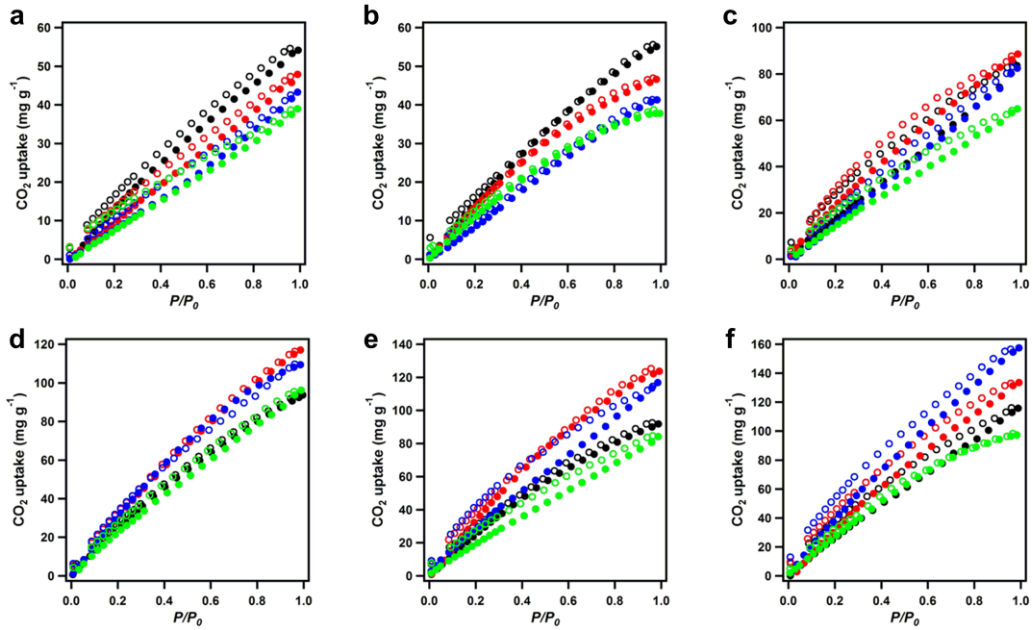

Figure 4. CO_2 sorption curves of $[HC{\equiv}C]_x$-H_2P-COFs (**a**, black: 25, red: 50, blue: 75, green: 100), $[Et]_x$-H_2P-COFs (**b**), $[MeOAc]_x$-H_2P-COFs (**c**), $[AcOH]_x$-H_2P-COFs (**d**), $[EtOH]_x$-H_2P-COFs (**e**) and $[EtNH_2]_x$-H_2P-COFs (**f**) at 273 K.

The systematic integration of functional groups, in combination with a significant decrease in the pore size, makes the resulting COFs attractive for CO_2 adsorption (**Figures 4 and 5**). $[HC{\equiv}C]_X$-H_2P-COFs with the X values of 0, 25, 50, 75, and 100 exhibited CO_2 capacity of 38, 29, 26, 24, and 20 mg g^{-1}, at 298 K and 1 bar; the capacities increased to 72, 54, 48, 43, and 39

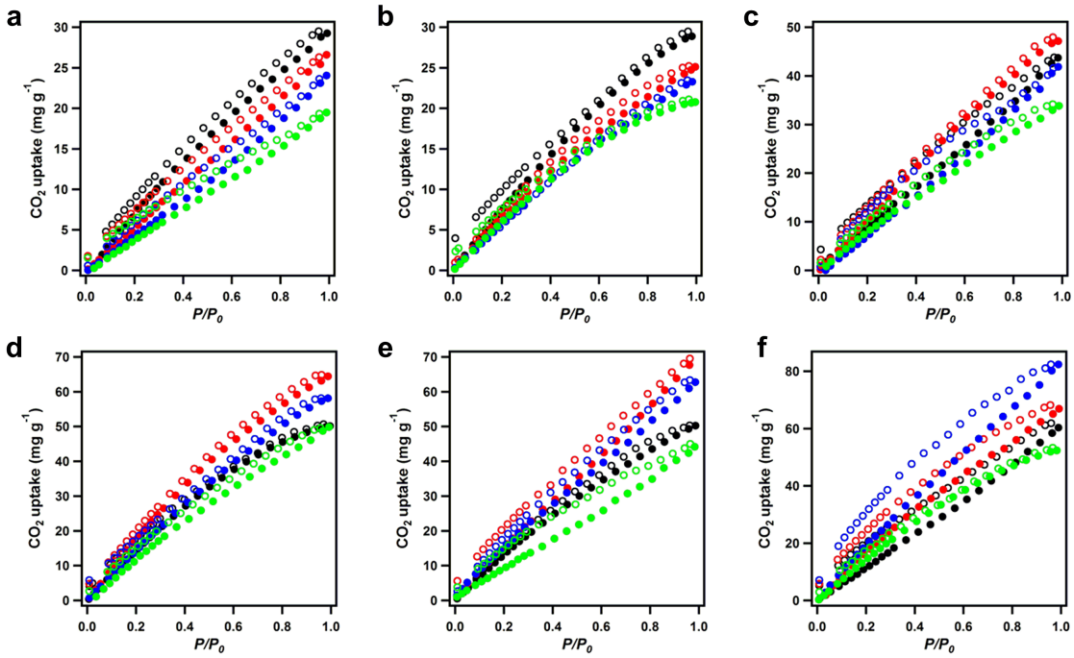

Figure 5. CO_2 sorption curves of $[HC{\equiv}C]_x$-H_2P-COFs (**a**), black: 25, red: 50, blue: 75, green: 100, $[Et]_x$-H_2P-COFs (**b**), $[MeOAc]_x$-H_2P-COFs (**c**), $[AcOH]_x$-H_2P-COFs (**d**), $[EtOH]_x$-H_2P-COFs (**e**) and $[EtNH_2]_x$-H_2P-COFs (**f**) at 298 K.

mg g^{-1} at 273 K and 1 bar (**Figure 6**). These results indicate that the $[HC{\equiv}C]_X$-H_2P-COFs are conventional COFs with low adsorption capacities. We observed that the capacity for CO_2 adsorption was highly dependent on the structures of the functional groups. Upon the introduction of ethyl units onto the pore walls, the resulting $[Et]_X$-H_2P-COFs (X = 25, 50, 75, and 100) exhibited CO_2 adsorption capacities similar to those of the $[HC{\equiv}C]_X$-H_2P-COFs under otherwise identical conditions (**Figure 6**).

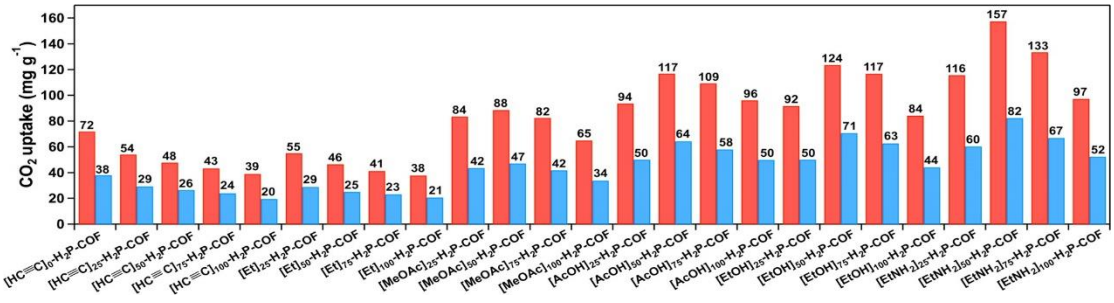

Figure 1. Carbon dioxide adsorption capacity of the COFs at 273 (red) and 298 K (blue) and 1 bar.

By contrast, when the functional groups were changed to ester units, the $[MeOAc]_X$-H_2P-COFs exhibited enhanced CO_2 adsorption capacities. $[MeOAc]_{50}$-H_2P-COF exhibites the highest capacity among the $[MeOAc]_X$-H_2P-COFs, with CO_2 adsorption capacities of 47 and 88 mg g^{-1} at 298 and 273 K, respectively (**Figure 6**).These values are 1.6-fold greater than those of the best-performing $[Et]_X$-H_2P-COFs. Notably, the introduction of carboxylic acid groups greatly enhanced the capacity. The capacities of $[AcOH]_{25}$-H_2P-COF, $[AcOH]_{50}$-H_2P-COF, $[AcOH]_{75}$-H_2P-COF, and $[AcOH]_{100}$-H_2P-COF were 50, 64, 58, and 50 mg g^{-1} at 298 K and 94, 117, 109, and 96 mg g^{-1} at 273 K, respectively (**Figure 6**). For example, $[EtOH]_{50}$-H_2P-COF exhibited capacities of 71 and 124 mg g^{-1} at 298 and 273 K, respectively, which are 2.3- to 2.4-fold greater than the capacities of $[HC{\equiv}C]_{25}$-H_2P-COF. Surprisingly, pore surface engineering with the amino groups led to an overall enhancement of CO_2 adsorption (**Figure 6**). The capacities of $[EtNH_2]_{25}$-H_2P-COF, $[EtNH_2]_{50}$-H_2P-COF, $[EtNH_2]_{75}$-H_2P-COF, and $[EtNH_2]_{100}$-H_2P-COF were 60, 82, 67, and 52 mg g^{-1} at 298 K and 116, 157, 133, and 97 mg g^{-1} at 273 K, respectively. $[EtNH_2]_{50}$-H_2P-COF exhibited the highest adsorption capacity, which was almost 3-fold greater than those of $[Et]_{50}$-H_2P-COF and $[HC{\equiv}C]_{50}$-H_2P-COF.

The nonpolar ethynyl and ethyl groups interact weakly with CO_2, resulting in their poor adsorption capacity. By contrast, the polar ester units could interact with CO_2 via dipole interactions and thus improve the affinity of the COF for CO_2. The enhanced capacities of $[AcOH]_X$-H_2P-COFs and $[EtOH]_X$-H_2P-COFs resulted from the dipole and hydrogen bonding interactions of carboxylic and hydroxyl units with CO_2. The amino groups can form acid–base pairs with CO_2, leading to a significant enhancement in CO_2 adsorption. COFs with the same functional groups show two different tendencies with respect to CO_2 adsorption. The first class is the $[Et]_X$-H_2P-COFs, in which the pore walls have fewer interactions with CO_2 and thus exhibit a simple decrease in CO_2 adsorption capacity with X values because of their decreased surface areas and pore volumes. The second class consists of the $[MeOAc]_X$-H_2P-COFs, $[AcOH]_X$-H_2P-COFs, $[EtOH]_X$-H_2P-COFs, and $[EtNH_2]_X$-H_2P-COFs, which all interact strongly with CO_2 and exhibit maximal capacities at X = 50. This behavior is the result of a balance between the two contradictory effects of enhanced affinity and decreased porosity on adsorption. This type of perturbation indicates that precise pore surface engineering is a key component of capturing CO_2

with COFs.

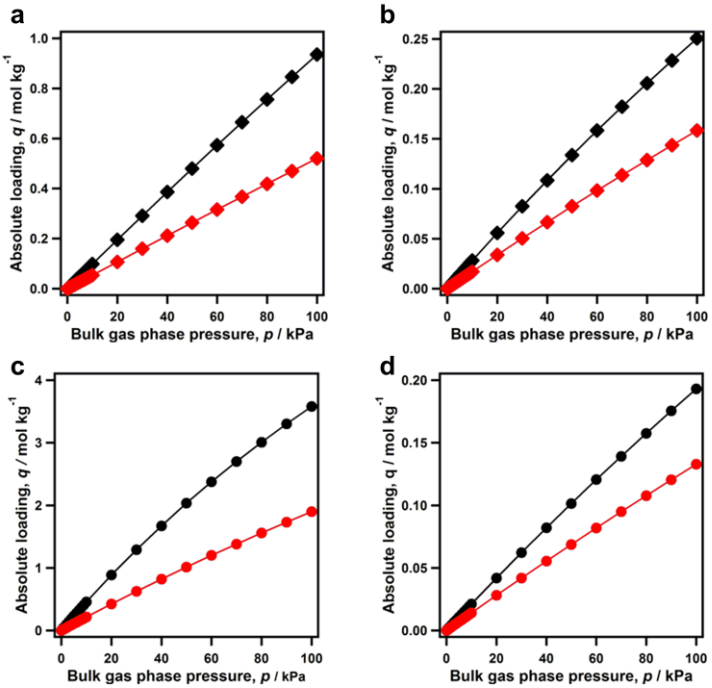

Figure 7. The fitted CO_2 and N_2 isotherm curves (black: 273K, red: 298K) of $[HC{\equiv}C]_{50}$-H_2P-COF (a, b) and $[EtNH_2]_{50}$-H_2P-COF (c, d).

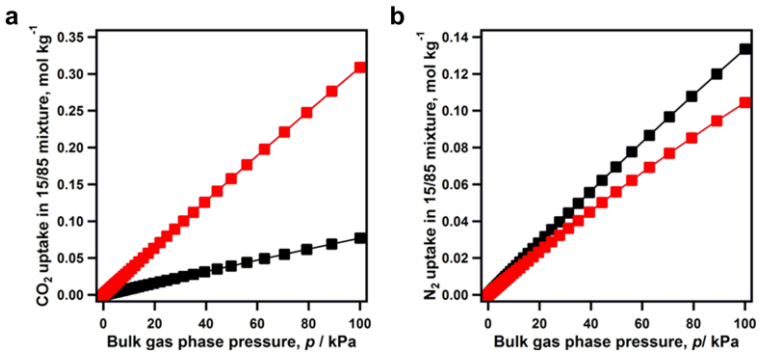

Figure 8. Calculations using Ideal Adsorbed Solution Theory (IAST) of Myers and Prausnitz for uptakes of CO_2 and N_2, expressed as moles per kg of adsorbent, in equilibrium with a binary CO_2/N_2 gas mixture maintained at isothermal conditions at 298 K(black: $[HC{\equiv}C]_{50}$-H_2P-COF, red: $[EtNH_2]_{50}$-H_2P-COF) . In these calculations the partial pressures of CO_2 and N_2 are taken to be p_1/ p_2=15/85.

To elucidate the nature of the CO_2 adsorption, we calculated the isosteric heat of adsorption (Q_{st}) from the CO_2 adsorption isotherm curves collected at pressures as high as 1 bar and at

temperatures of 273 and 298 K. Interestingly, the Q_{st} value increased in the order of $[HC\equiv C]_X$-H_2P-COFs ≈ $[Et]_X$-H_2P-COFs < $[MeOAc]_X$-H_2P-COFs < $[AcOH]_X$-H_2P-COFs < $[EtOH]_X$-H_2P-COFs < $[EtNH_2]_X$-H_2P-COFs. For example, $[HC \equiv C]_X$-H_2P-COFs and $[Et]_X$-H_2P-COFs had Q_{st} values of 15.3–16.8 kJ mol^{-1}. The Q_{st} values of $[MeOAc]_X$-H_2P-COFs were higher, ranging between 16.4 and 17.8 kJ mol^{-1}. More significant enhancements in the Q_{st} values were observed for $[AcOH]_X$-H_2P-COFs and $[EtOH]_X$-H_2P-COFs; these COFs had Q_{st} values of 17.7-18.8 and 18.2-19.3 kJ mol^{-1}, respectively. $[EtNH_2]_X$-H_2P-COFs exhibited the highest Q_{st} values, which ranged from 20.4 to 20.9 kJ mol^{-1}. These results indicate that the COFs with the strongest affinity for CO_2 were those with pore walls that were functionalized with amino groups; those groups facilitated the adsorption of CO_2 and contributed to the enhanced CO_2 adsorption performance (ideal adsorbed solution theory (IAST) calculations of selectivity, see **Figure 7**).

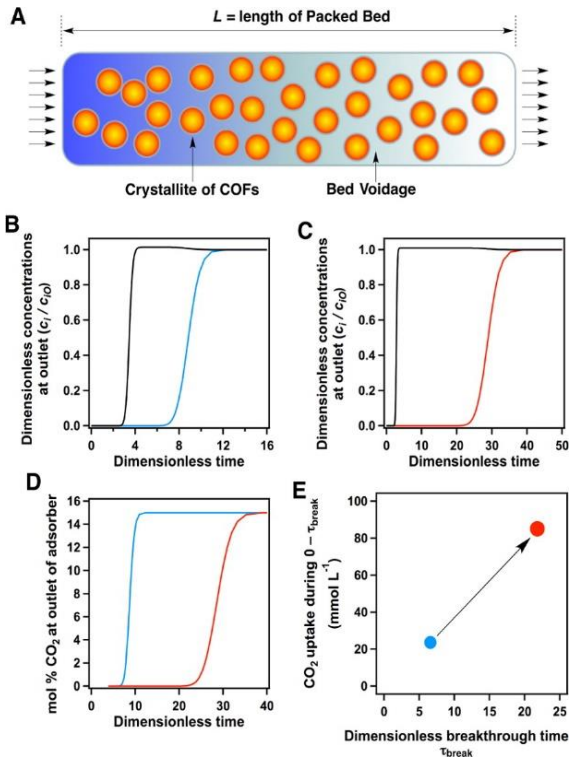

Figure 9. (A) Fixed-bed adsorber for COFs. Flue-gas breakthrough profiles of (B) $[HC\equiv C]_{50}$-H_2P-COF and (C) $[EtNH_2]_{50}$-H_2P-COF at 298 K. (D) Comparison of % CO_2 at the adsorber outlet at 298 K (blue curve, $[HC\equiv C]_{50}$-H_2P-COF; red curve, $[EtNH_2]_{50}$-H_2P-COF). (E) Comparison of CO_2 capture productivity at 298 K (blue circle, $[HC\equiv C]_{50}$-H_2P-COF; red circle, $[EtNH_2]_{50}$-H_2P-COF).

To evaluate the gas adsorption capability of adsorbents under kinetic flowing gas conditions (CO_2/N_2 mixture containing 15% CO_2 and 85% N_2, 298 K, 100 kPa), we performed breakthrough simulations using a precise methodology established by Krishna and Long (**Figures 8**). These simulations accurately reflect the separation ability of a pressure-swing adsorption (PSA) process, which is an energetically efficient method for industrial-scale capture. **Figure 9A** shows a schematic of a packed-bed absorber. **Figure 9B, C** presents typical breakthrough curves for $[HC{\equiv}C]_{50}$-H_2P-COF and $[EtNH_2]_{50}$-H_2P-COF, respectively, where the x-axis is dimensionless time, τ, which is defined as the division of actual time t by the characteristic time $L\varepsilon/\mu$. $[EtNH_2]_{50}$-H_2P-COF exhibited a breakthrough time of 25, which was much longer than that of $[HC{\equiv}C]_{50}$-H_2P-COF (7). **Figure 9D** compares the breakthrough characteristics of the two COFs in terms of CO_2 concentration (mol%) at the absorber outlet, which is depicted as a function of dimensionless time when the operation was performed at a total pressure of 100 kPa. $[EtNH_2]_{50}$-H_2P-COF (red curve) had a breakthrough time much longer than that of $[HC{\equiv}C]_{50}$-H_2P-COF (blue curve). Longer breakthrough times are desirable for greater CO_2 capture. For a quantitative evaluation, we arbitrarily chose the required outlet gas purity as <0.05 mol% CO_2. Using this purity specification, we determined the breakthrough times, τ_{break}, for the COFs. Based on the material balance on the absorber, we determined the amount of CO_2 captured during the time interval 0-τ_{break}. Figure 2E shows the plot of the number of millimoles of CO_2 capture per liter of adsorbent during the time interval 0 - τ_{break} against the τ_{break}. Notably, $[EtNH_2]_{50}$-H_2P-COF (red circle) exhibited superior CO_2 productivity (90 mmol L^{-1}) compared to $[HC{\equiv}C]_{50}$-H_2P-COF (blue circle; 21 mmol L^{-1}).

Conclusion

COFs with highly functionalized pore wall structures are difficult to obtain via direct polycondensation reactions. The systematic pore surface engineering of COFs enables the tailor-made covalent docking of a variety of different functional groups with controlled loading contents to the pore walls. The surface engineering of the pore walls profoundly affects the surface area, pore size, pore volume, and pore environment. As demonstrated for CO_2 adsorption, pore surface engineering is a high throughput and efficient method for achieving both enhanced

adsorption capacities and improved separation capabilities. Notably, this approach is not limited to the present COF and is widely applicable to many other previously reported COFs. We envisage that pore surface engineering might be a general strategy for screening for COF materials that satisfy the multiple requirements of CO_2 capture in industrial-level flow-gas applications.

Experimental Sections

Fourier transform Infrared (FT IR) spectra were recorded on a JASCO model FT IR-6100 infrared spectrometer. UV-Vis-IR diffuse reflectance spectrum (Kubelka-Munk spectrum) was recorded on a JASCO model V-670 spectrometer equipped with integration sphere model IJN-727. Powder X-ray diffraction (PXRD) data were recorded on a Rigaku model RINT Ultima III diffractometer by depositing powder on glass substrate, from $2\theta = 1.5°$ up to 60° with 0.02° increment. Elemental analysis was performed on a Yanako CHN CORDER MT-6 elemental analyzer. Nitrogen sorption isotherms were measured at 77 K with a Bel Japan Inc. model BELSORP-mini II analyzer. Before measurement, the samples were degassed in vacuum at 120 ℃ for more than 10 h. By using the non-local density functional theory (NLDFT) model, the pore volume was derived from the sorption curve. 1H NMR spectra were recorded on a JEOL model JNM-LA400 NMR spectrometer, where the chemical shifts (δ in ppm) were determined with a residual proton of the solvent as standard.

Materials and Synthetic Procedures

n-Butanol, o-dichlorobenzene (o-DCB), anhydrous acetone (99.5%), and tetrahydrofuran were purchased from Wako Chemicals. 1,4-Phthalaldehyde (PA) was purchased from TCI. Free-base 5,10,15,20-tetrakis(p-tetraphenylamino) porphyrin (H_2P) was prepared from p-nitrobenzaldehyde using a literature procedure.S1 2,5-Dihydroxyterephthalaldehyde (DHTA) and 2,5-bis(2-propynyloxy) terephthalaldehyde (BPTA) were synthesized according to a reported method.

$[HC{\equiv}C]_X$-H_2P-COFs. An o-DCB/BuOH (0.5 mL / 0.5 mL) mixture of H_2P (0.022 mmol, 14.9 mg) and DHTA/BPTA (total 0.044 mmol) at different molar ratios of 100/0, 75/25, 50/50, 25/75, and 0/100 in the presence of acetic acid catalyst (3 M, 0.1 mL) in a Pyrex tube (10 mL) was

degassed by three freeze-pump-thaw cycles. The tube was sealed off by flame and heated at 120 ℃ for 3 days. The precipitate was collected via centrifuge, washed with THF for 6 times, and washed with acetone 3 times. The powder was dried at 120 ℃ under vacuum overnight to give the corresponding COFs in isolated yields of 80%, 72%, 69%, 86%, and 80% for the $[HC{\equiv}C]_0$-H_2P-COF, $[HC{\equiv}C]_{25}$-H_2P-COF, $[HC{\equiv}C]_{50}$-H_2P-COF, $[HC{\equiv}C]_{75}$-H_2P-COF, and $[HC{\equiv}C]_{100}$-H_2P-COF, respectively.

$[R]_X$-H_2P-COFs. A toluene/n-butanol (0.8 mL / 0.2 mL) mixture of $[HC{\equiv}C]_{25}$-H_2P-COF (20 mg) in the presence of CuI (2 mg) and DIPEA (40 μL) in a Pyrex tube (10 mL) was added with azide compounds. The tube was degassed via three freeze-pump-thaw cycles and the mixture was stirred at room temperature for 24 h. The precipitate was collected via centrifuge, washed with ethanol 5 times, and dried at room temperature under vacuum, to produce $[R]_{25}$-H_2P-COF as a deep brown solid in quantitative yield. The ethynyl groups were quantatively reacted with the azide units as evident by the IR spectra. The click reaction of $[HC{\equiv}C]_X$-H_2P-COFs (X = 50, 75, and 100) with azides compounds were performed according to this method under otherwise same conditions.

Fitting of pure component isotherms

The salient properites of two different COFs ($[HC{\equiv}C]_{50}$-H_2P-COFs and $[EtNH_2]_{50}$-H_2P-COF) are specified in **Table 4**. The potential of these COFs are evaluated for the separation of CO_2/N_2 mixtures that is relevant for CO_2 capture from flue gases. For my evaluations, I assume the CO_2/N_2 mixtures to contain 15% CO_2, and 85% N_2, following the earlier work of Mason et al.[8a]

The experimentally measured excess loadings of CO_2, and N_2, obtained at different temperatures, were first converted to absolute loadings before data fitting. The procedure for converting to absolute loadings is the same as described in the Supporting Information accompanying the paper of Wu et al.[8b] For the purpose of converting to absolute loadings, the pore volumes used are specified in **Table 5**. The isotherm data for CO_2 were fitted with the Langmuir-Freundlich model:

$$q = q_{sat}\frac{bp^{\nu}}{1+bp^{\nu}} \quad (11)$$

with *T*-dependent parameter *b*

$$b_A = b_0 \exp\left(\frac{E}{RT}\right) \quad (12)$$

The Langmuir-Freundlich parameters for adsorption of CO_2 are provided in **Table 6**. The simpler Langmuir model was adequate for fitting the isotherm data for N_2; Table S6 provides the *T*-dependent Langmuir parameters for N_2 in different materials.

Table 4. Salient properties of $[HC{\equiv}C]_{50}$-H_2P-COF and $[EtNH_2]_{50}$-H_2P-COF (The crystal framework densities, required in the breakthrough simulations, are estimated as (bulk density)/(one-bed porosity) with the assumption that the bed porosity is 0.4.)

COFs	Bulk density (g cm^{-3})	S_{BET} (m^2 g^{-1})	Pore volume (cm^3 g^{-1})	Pore size (nm)
$[HC{\equiv}C]_{50}$-H_2P-COF	0.24	683	0.42	1.91
$[EtNH_2]_{50}$-H_2P-COF	0.27	568	0.36	1.56

Table 5. Langmuir-Freundlich parameters for adsorption of CO_2 in COFs (The experimentally measured excess loadings were first converted to absolute loadings before data fitting.)

COFs	q_{sat} (mol kg^{-1})	b_0 (Pa^{-v})	E (kJ mol^{-1})
$[HC{\equiv}C]_{50}$-H_2P-COF	18	3.82×10^{-10}	16.5
$[EtNH_2]_{50}$-H_2P-COF	15	3.14×10^{-10}	20.9

Table 6. One-site Langmuir parameters for N_2 in different materials

COFs	$q_{A,sat}$ (mol kg^{-1})	b_{A0} (Pa^{-1})	E_A (kJ mol^{-1})
$[HC{\equiv}C]_{50}$-H_2P-COF	2	3.28×10^{-9}	13.8
$[EtNH_2]_{50}$-H_2P-COF	2	8.4×10^{-9}	11

2.4.4 Isosteric heat of adsorption

The isosteric heat of adsorption, Q_{st}, defined as

$$Q_{st} = RT^2\left(\frac{\partial \ln p}{\partial T}\right)_q \quad (13)$$

was determined using the pure component isotherm fits using the Clausius-Clapeyron equation.

2.4.5 IAST calculations

The selectivity of preferential adsorption of component 1 over component 2 in a mixture containing 1 and 2, perhaps in the presence of other components too, can be formally defined as

$$S_{ads} = \frac{q_1/q_2}{p_1/p_2} \quad (14)$$

In equation (14), q_1 and q_2 are the *absolute* component loadings of the adsorbed phase in the mixture. These component loadings are also termed the uptake capacities. In all the calculations to be presented below, the calculations of q_1 and q_2 are based on the use of the Ideal Adsorbed Solution Theory (IAST) of Myers and Prausnitz.[8c] The accuracy of the IAST calculations for estimation of the component loadings for several binary mixtures in a wide variety of zeolites, and MOFs has been established by comparison with Configurational-Bias Monte Carlo (CBMC) simulations of mixture adsorption.[8d-i]

2.4.6 Simulation methodology for transient breakthrough in fixed bed absorbers

The separation of CO_2/N_2 mixtures is commonly carried out in fixed bed absorbers in which the separation performance is dictated by a combination of three separate factors: (a) adsorption selectivity, (b) uptake capacity, and (c) intra-crystalline diffusivities of guest molecules within the pores. Transient breakthrough simulations are required for a proper evaluation of MOFs; the simulation methodology used in my work is described in earlier publications.[8j,8k] A brief summary of the simulation methodology is presented below.

Assuming plug flow of an *n*-component gas mixture through a fixed bed maintained under isothermal conditions, the partial pressures in the gas phase at any position and instant of time are obtained by solving the following set of partial differential equations for each of the species *i* in the gas mixture.[8l]

$$\frac{1}{RT}\frac{\partial p_i(t,z)}{\partial t} = -\frac{1}{RT}\frac{\partial\left(v(t,z)p_i(t,z)\right)}{\partial z} - \frac{(1-\varepsilon)}{\varepsilon}\rho\frac{\partial \bar{q}_i(t,z)}{\partial t}; \qquad i = 1,2,\ldots n \qquad (15)$$

In equation (15), t is the time, z is the distance along the adsorber, r is the framework density, e is the bed voidage, v is the interstitial gas velocity, and $\bar{q}_i(t,z)$ is the *spatially averaged* molar loading within the crystallites of radius r_c, monitored at position z, and at time t.

At any time t, during the transient approach to thermodynamic equilibrium, the spatially averaged molar loading within the crystallite r_c is obtained by integration of the radial loading profile

$$\bar{q}_i(t) = \frac{3}{r_c^3}\int_0^{r_c} q_i(r,t)r^2 dr \qquad (16)$$

For transient unary uptake within a crystal at any position and time with the fixed bed, the radial distribution of molar loadings, q_i, within a spherical crystallite, of radius r_c, is obtained from a solution of a set of differential equations describing the uptake

$$\frac{\partial q_i(r,t)}{\partial t} = -\frac{1}{\rho}\frac{1}{r^2}\frac{\partial}{\partial r}\left(r^2 N_i\right) \qquad (20)$$

The molar flux N_i of component i is described by the simplified version of the Maxwell-Stefan equations in which both correlation effects and thermodynamic coupling effects are considered to be of negligible importance

$$N_i = -\rho D_i \frac{\partial q_i}{\partial r} \qquad (21)$$

Summing equation (19) over all n species in the mixture allows calculation of the *total average* molar loading of the mixture within the crystallite

$$\bar{q}_t(t,z) = \sum_{i=1}^{n} \bar{q}_i(t,z) \qquad (7)$$

The *interstitial* gas velocity is related to the *superficial* gas velocity by

$$v = \frac{u}{\varepsilon} \qquad (8)$$

In industrial practice, the most common operation uses a step-wise input of mixtures to be separated into an absorber bed that is initially free of adsorbents, i.e. I have the initial condition

$$t = 0; \quad q_i(0,z) = 0 \qquad (9)$$

At time $t = 0$, the inlet to the absorber, $z = 0$, is subjected to a step input of the n-component gas mixture and this step input is maintained till the end of the adsorption cycle when steady-state conditions are reached.

$$t \geq 0; \quad p_i(0,t) = p_{i0}; \quad u(0,t) = u_0 \quad (10)$$

where u_0 is the superficial gas velocity at the inlet to the absorber.

The breakthrough characteristics for any component is essentially dictated by two sets of parameters: (a) The characteristic contact time between the crystallites and the surrounding fluid phase, and (b) , that reflect the importance of intra-crystalline diffusion limitations. It is common to use the dimensionless time,, obtained by dividing the actual time t, by the characteristic time, when plotting simulated breakthrough curves.

If the value of is large enough to ensure that intra-crystalline gradients are absent and the entire crystallite particle can be considered to be in thermodynamic equilibrium with the surrounding bulk gas phase at that time *t*, and position *z* of the adsorber

$$\overline{q}_i(t,z) = q_i(t,z) \quad (11)$$

The molar loadings at the *outer surface* of the crystallites, i.e. at $r = r_c$, are calculated on the basis of adsorption equilibrium with the bulk gas phase partial pressures p_i at that position *z* and time *t*. The adsorption equilibrium can be calculated on the basis of the IAST. The assumption of thermodynamic equilibrium at every position *z*, and any time *t*, i.e. invoking Equation (11), generally results in sharp breakthroughs for each component. Sharp breakthroughs are desirable in practice because this would result in high productivity of pure products. Essentially, the influence of intra-crystalline diffusion is to reduce the productivity of pure gases. For all the breakthrough calculations reported in this work, I assume negligible diffusion resistances for all materials and I invoke the simplified Equation (11).

Notation

b_A	dual-Langmuir-Freundlich constant for species *i* at adsorption site A,
c_i	molar concentration of species *i* in gas mixture, mol m^{-3}
c_{i0}	molar concentration of species *i* in gas mixture at inlet to adsorber, mol m^{-3}
L	length of packed bed adsorber, m
N	number of species in the mixture, dimensionless
N_i	molar flux of species *i*, mol m^{-2} s^{-1}
p_i	partial pressure of species *i* in mixture, Pa
p_t	total system pressure, Pa
q_i	component molar loading of species *i*, mol kg^{-1}
$\overline{q}_i(t, z)$	*spatially averaged* component molar loading of species *i*, mol kg^{-1}
r_c	radius of crystallite, m
R	gas constant, 8.314 J mol^{-1} K^{-1}
t	time, s
T	absolute temperature, K
u	superficial gas velocity in packed bed, m s^{-1}
v	interstitial gas velocity in packed bed, m s^{-1}

Greek letters

e	voidage of packed bed, dimensionless
r	framework density, kg m^{-3}
	time, dimensionless

Subscripts

i	referring to component
i_{break}	referring to breakthrough
t	referring to total mixture

References

1. a) A. P. Côte, A. I. Benin, N. W. Ockwig, M. O'Keeffe, A. J. Matzger, O. M. Yaghi, *Science* **2005**, *310*, 1166-1170; b) S. Wan, J. Guo, J. Kim, H. Ihee, D. Jiang, *Angew. Chem., Int. Ed.* **2009**, *48*, 5439-5442; c) C. J. Doonan, D. J. Tranchemontagne, T. G. Glover, J. H. Hunt, O. M. Yaghi, *Nat. Chem.* **2010**, *2*, 235-238; d) C. R. DeBlase, K. E. Silberstein, T.-T. Truong, H. D. Abruña, W. R. Dichtel, *J. Am. Chem. Soc.* **2013**, *135*, 16821-16824; e) D. N. Bunck, W. R. Dichtel, *Angew. Chem., Int. Ed.* **2012**, *51*, 1885-1889; f) S. Y. Ding, W. Wang, *Chem. Soc. Rev.* **2013**, *42*, 548-568; g) M. Calik, F. Auras, L. M. Salonen, K. Bader, I. Grill, M. Handloser, D. D. Medina, M. Dogru, F. Löbermann, D. Trauner, A. Hartschuh, T. Bein, *J. Am. Chem. Soc.* **2014**, *136*, 17802-17807;
2. a) F. J. Uribe-Romo, J. R. Hunt, H. Furukawa, C. Klöck, M. O'Keeffe, O. M. Yaghi, *J. Am. Chem. Soc.* **2009**, *131*, 4570; b) L. M. Lanni, R. W. Tilford, M. Bharathy, J. J. Lavigne, *J. Am. Chem. Soc.* **2011**, *133*, 13975-13983; c) S. Kandambeth, D. B. Shinde, M. K. Panda, B. Lukose, T. Heine, R. Banerjee, *Angew. Chem., Int. Ed.* **2013**, *52*, 13052-13056; d) T. Zhou, S. Xu, Q. Wen, Z. Pang, X. Zhao, *J. Am. Chem. Soc.* **2014**, *136*, 15885-15888; e) Y. Zeng, R. Zou, Z. Luo, H. Zhang, X. Yao, X. Ma, R. Zou, Y. Zhao, *J. Am. Chem. Soc.* **2015**, *137*, 1020-1023; f) D. D. Medina, J. M. Rotter, Y. Hu, M. Dogru, V. Werner, F. Auras, J. T. Markiewicz, P. Knochel, T. Bein, *J. Am. Chem. Soc.* **2015**, *137*, 1016-1019.
3. a) Furukawa, H.; Yaghi, O. M. *J. Am. Chem. Soc.* **2009**, *131*, 8875-8883; b) Feng, X.; Ding, X.; Jiang, D. *Chem. Soc. Rev.* **2012**, *41*, 6010-6022; c) X. Chen, M. Addicoat, E. Jin, L. Zhai, H. Xu, N. Huang, Z. Guo, L. Liu, S. Irle, D. Jiang, *J. Am. Chem. Soc.* **2015**, *137*, 3241-3247.
4. a) P. Kuhn, M. Antonietti, A. Thomas, *Angew. Chem., Int. Ed.* **2008**, *47*, 3450-3453; b) X. Wang, K. Maeda, A. Thomas, K. Takanabe, G. Xin, J. M. Carlsson, K. Domen, M. Antonietti, *Nat. Mater.* **2008**, *8*, 76-80; c) A. Nagai, Z. Guo, X. Feng, S. Jin, X. Chen, X. Ding, D. Jiang, *Nat. Commun.* **2011**, *2*, 536; d) X. Liu, C. Guan, S. Ding, W. Wang, H. Yan, D. Wang, L. Wan, *J. Am. Chem. Soc.* **2013**, *135*, 10470-10474; e) Z. Li, X. Feng, Y. Zou, Y. Zhang, H. Xia, X. Liu, Y. Mu, *Chem. Commun.* **2014**, *50*, 13825-13828; f) L. Chen, K. Furukawa, J. Gao, A. Nagai, T. Nakamura, Y. Dong, D. Jiang, *J. Am. Chem. Soc.* **2014**, *136*, 9806-9809.
5. a) H. Xu, X. Chen, J. Gao, J. Lin, M. Addicoat, S. Irle, D. Jiang, *Chem. Commun.* **2014**, *50*, 1292-1294; b) N. Huang, X. Chen, R. Krishna, D. Jiang, *Angew. Chem., Int. Ed.* **2015**, *54*,

2986-2990.

6. a) E. L. Spitler, W. R. Dichtel, *Nat. Chem.* **2010**, *2*, 672-677; b) J. W. Colson, A. R. Woll, A.Mukherjee, M. P. Levendorf, E. L. Spitler, V. B. Shields, M. G. Spencer, J. Park, W. R. Dichtel, *Science* **2011**, *332*, 228-231; c) M. G. Rabbani, A. K. Sekizkardes, Z. Kahveci, T. E. Reich, R. Ding, H. M. El-Kaderi, *Chem. Eur. J.* **2013**, *19*, 3324-3328; d) L. Stegbauer, K. Schwinghammer, B. V. Lotsch, *Chem. Sci.* **2014**, *5*, 2789-2793; e) Q. Fang, Z. Zhuang, S. Gu, R. B. Kaspar, J. Zheng, J. Wang, S. Qiu, Y. Yan, *Nat. Commun.* **2014**, *5*, 4503.
7. a) S. Y. Ding, J. Gao, Q. Wang, Y. Zhang, W. Song, C. Su, W. Wang, *J. Am. Chem. Soc.* **2011**, *133*, 19816-19822; b) D. Wu, F. Xu, B. Sun, R. Fu, H. He, K. Matyjaszewski, *Chem. Rev.* **2012**, *112*, 3959-4015; c) D. Wu, Z. Li, M. Zhong, T. Kowalewski, K. Matyjaszewski, *Angew. Chem., Int. Ed.* **2014**, *53*, 3957-3960.
8. a) R. Krishna, J. R. Long, *J. Phys. Chem.* C **2011**, *115*, 12941-12950; b) J. A. Mason, K. Sumida, Z. R. Herm, R. Krishna, J. R. Long, *Energy Environ. Sci.* **2011**, *4*, 3030-3040.

Part II

Conjuagted Micro/Mesoporous Polymers

Chapter 3

High-Performance Heterogeneous Catalysis with Surface-Exposed Stable Metal Nanoparticles

Scientific Reports **2014**, *4*, 7228.

Ning Huang, Yanhong Xu and Donglin Jiang

Abstract: Protection of metal nanoparticles from agglomeration is critical for their functions and applications. The conventional method for enhancing their stability is to cover them with passivation layers to prevent direct contact. However, the presence of a protective shell blocks exposure of the metal species to reactants, thereby significantly impeding the nanoparticles' utility as catalysts. Here, I report that metal nanoparticles can be prepared and used in a surface-exposed state that renders them inherently catalytically active. This strategy is realised by spatial confinement and electronic stabilisation with a dual-module mesoporous and microporous three-dimensional π-network in which surface-exposed nanoparticles are crystallised upon in situ reduction. The uncovered palladium nanoparticles serve as heterogeneous catalysts that are exceptionally active in water, catalyse unreactive aryl chlorides for straightforward carbon–carbon bond formation and are stable for repeated use in various types of cross couplings. Therefore, my results open new perspectives in developing practical heterogeneous catalysts.

Keywords: Porous materials; Heterogenerous catalysts; Conjugated microporous polymers; Palladium nanoparticles

Introduction

Metal nanoparticles (MNPs) are a class of nanomaterials that consist of clusters of reduced metal atoms. They play a pivotal role in areas such as optoelectronics[1a,1b] energy storage and conversion,[1c] catalysts for the production of fuels and chemicals[2] and biomedical applications.[2d, 3a] MNPs tend to agglomerate to form large particles, a phenomenon known as Ostwald ripening, which results in a reduction of their surface area and a loss of their specific functions. A general strategy for preventing agglomeration is to cover the surface with passivation layers that block the direct contact of particles. Various surface-modification methods have been demonstrated to be effective in enhancing the stability of MNPs.[3-4] However, these methods are not free from problems. The presence of passivation shell unavoidably impedes the energy, electron and magnetic/spin exchanges and interactions with other molecules and thus stifles their inherent functions. A particular concern pertaining to the development of MNP-based catalysts is that the stability of MNPs is enhanced at the expense of catalytic performance because the presence of protective layers renders the metal species under the surface shells inaccessible to reactants. Surface exposure and particle stability are two incompatible aspects; their combination is highly desirable for disclosing their inherent functions and applications but remains a substantial challenge for MNPs.[4]

In this study, I develop a set of techniques concerning the surface-exposed yet stable MNPs, including a general technique for producing MNPs, a facile method to construct dual-module porous π-network as MNP carriers and a practical application of these surface-exposed MNPs as exceptional active heterogeneous catalysts. I explore the surface-exposed MNPs, with preservation of their stability, using conjugated microporous/mesoporous polymers (CMPs) as matrices through the in situ reductive crystallisation of nanoparticles. CMPs are a class of organic porous polymers that combine the properties of π-conjugated three-dimensional networks and permanent nanopores,[5-8] in contrast to other porous materials that are not π-conjugated and to conventional conjugated polymers that are nonporous. I design the CMPs with an electron-rich three-dimensional network capable of π-cloud delocalisation for the electronic stabilisation of uncovered MNPs and with a dual-module nanoporous hierarchy in which mesopores spatially confine palladium nanoparticles (PdNPs) and micropores help to block their association. This uncovered configuration exposes the inherent catalytic functions of MNPs.

Surface-exposed PdNPs in H_2P-CMP are highly active heterogeneous catalysts (PdNPs⊃H_2P-CMP) that function stably in neat water, are robust for repeated use in various cross-coupling reactions and efficiently catalyse even unreactive aryl chlorides for carbon–carbon bond formation. I demonstrate the generality and diverse functions of PdNPs⊃H_2P-CMP by using three different types of carbon–carbon bond formations, including Suzuki, Sonogashira and Stille reactions with a wide range of various different reactants. PdNPs⊃H_2P-CMP combines activity, stability, reusability, versatility and environmental benignity that meet the requirements of catalysts for practical application. These results unambiguously reveal the significance of exposed surface in disclosing inherent functions and applications of nanoparticles. The present surface-exposure technique is general and widely applicable to other nanoparticles.

The field of homogeneous palladium catalysis for carbon-carbon bond formation remains problematic with respect to the practical application owing to the difficulty in the separation of expensive catalysts for repeated use and the contamination of products by metal species.[9-10] The development of heterogeneous catalysts has proved to be increasingly important as an attractive solution to these problems. Using aryl chloride substrates is critical for applications, as they are readily available and inexpensive.[10] However, aryl chlorides are much more difficult to activate than the widely employed aryl bromides and iodides. Although heterogeneous palladium catalysts have been investigated for the carbon–carbon bond formation reactions by loading Pd NPs in various porous supporters such as metal-organic frameworks, covalent organic frameworks, CMPs, porous organic polymers, porous carbon, and porous silica, and other carriers such as dendrimers, graphenes, nanotubes, linear polymers, and oligomers, the successful examples that can use aryl chlorides have been very limited; the activation of aryl chlorides remains particularly challenging.[11a,11b] The majority of heterogeneous systems are working in organic solvents or organic-aqueous mixtures;[11c] the exploration of neat water as solvent is of particular environmental and economic concerns. Cycle performance is crucial for applications, however, satisfying results are rarely achieved for heterogeneous PdNP catalysts thus far reported; the reusability issue remains to be well explored.

Results and Discussion

The key to PdNPs⊃H_2P-CMP is to combine extended π-cloud delocalisation with dual-module mesopores and micropores in a three-dimensional network (**Figure 1a, b**). CMPs are usually obtained as microporous materials; dual-module microporous and mesoporous CMPs are rare.[21, 30, 34] I observed that the porosity of CMPs is largely dependent on the reaction time. For

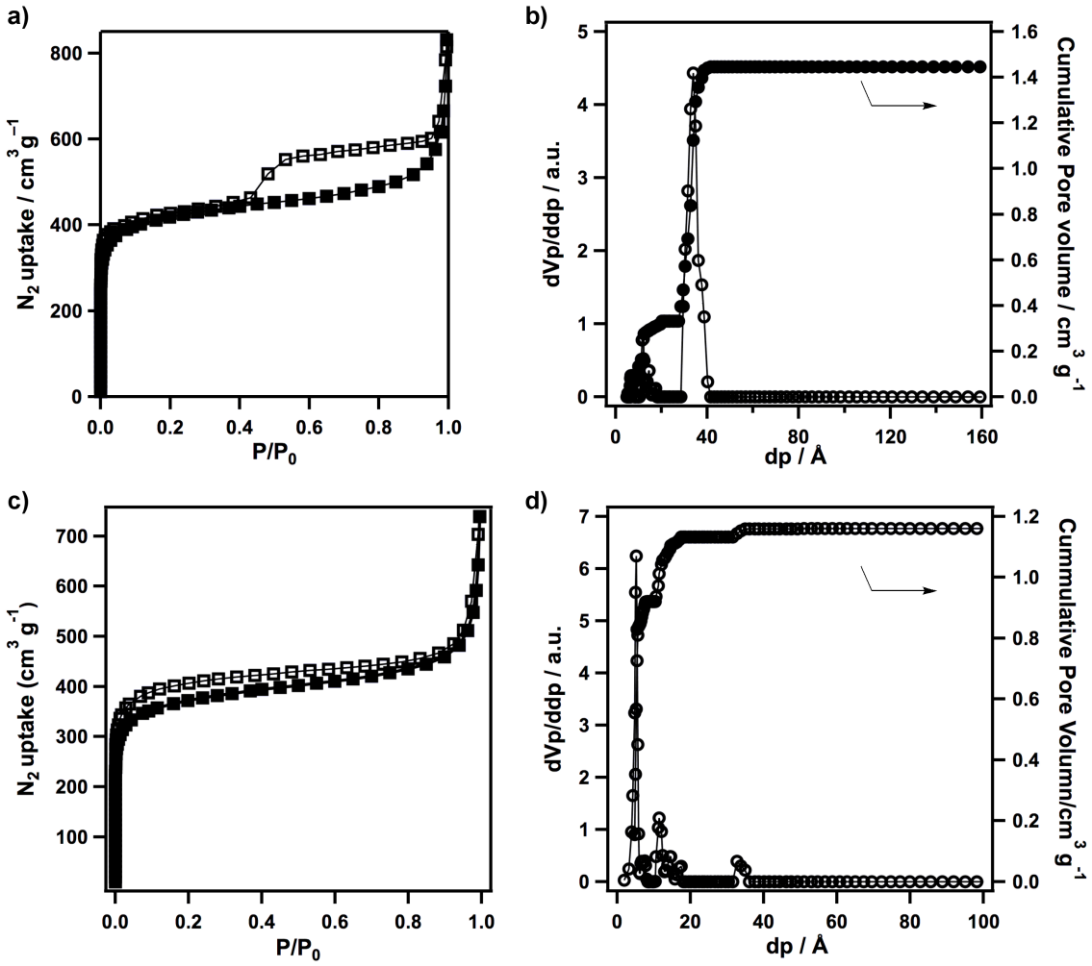

Figure 1. a) Nitrogen sorption isotherms of H_2P-CMP (24 h) measured at 77 K. b) pore size (open circle) distribution and pore volume (filled circle) profiles of H_2P-CMP (24 h). The BET surface area and pore volume of H_2P-CMP were 1283 m^2 g^{-1} and 1.48 cm^3 g^{-1}, respectively. The pore size was 3.1-4.0 nm. c) Nitrogen sorption isotherms of H_2P-CMP (72 h) measured at 77 K.d) pore size (open circle) distribution and pore volume (filled circle) profiles of H_2P-CMP (72 h).The BET surface area and pore volume of H_2P-CMP were 1148 m^2 g^{-1} and 1.16 cm^3 g^{-1}, respectively. The pore size was 0.6-0.8 nm and 1.0-1.6 nm.

example, the Yamamoto coupling reaction of 5, 10, 15, 20-tetrakis(4′-bromophenyl)porphyrin for 24 h yielded H_2P-CMP samples with dual-module mesopores and micropores (**Figure 1a, b**). Further extension of the reaction time caused the mesopores to disappear and eventually resulted

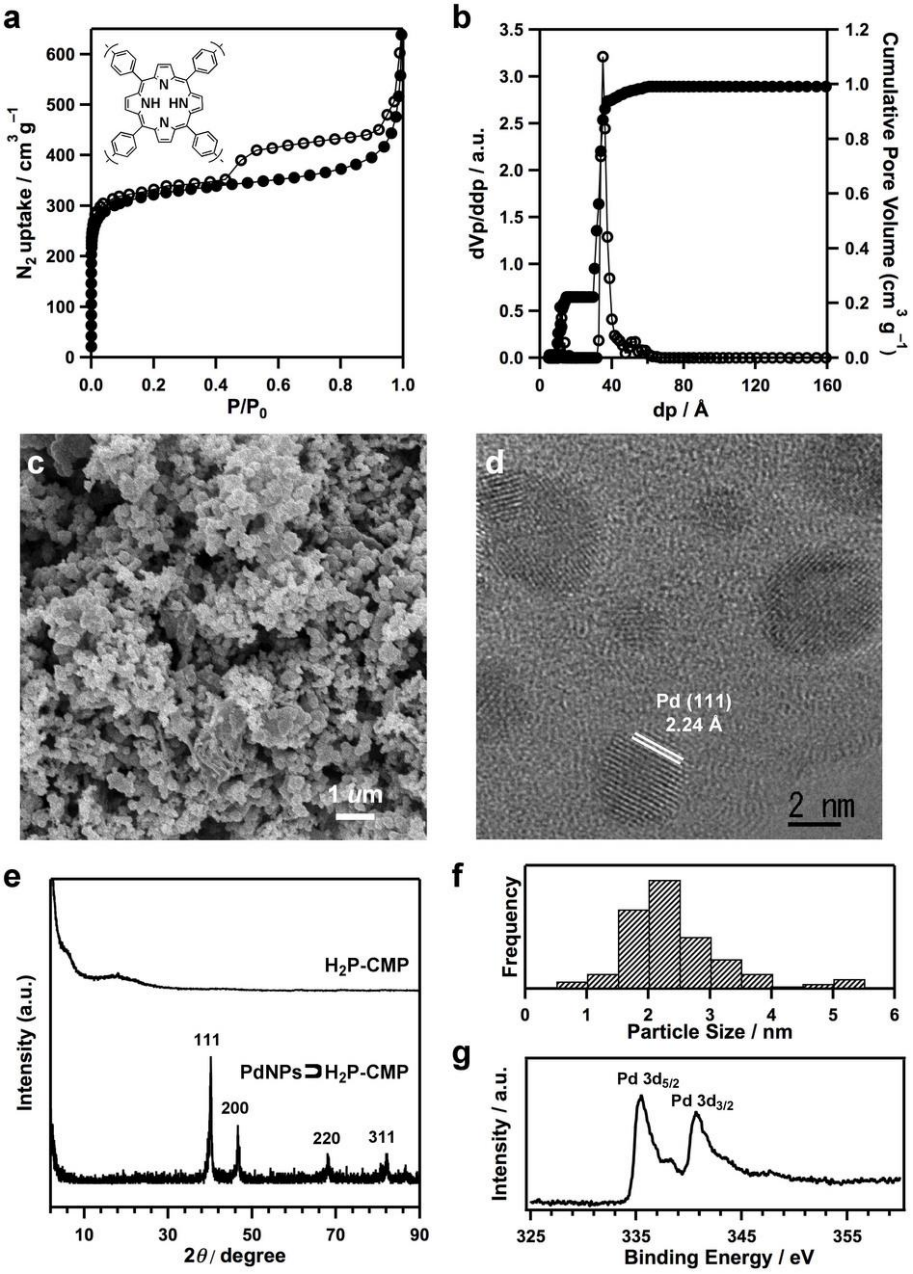

Figure 2. (a), Nitrogen sorption isotherms of PdNPs⊃H_2P-CMP measured at 77 K. (b), Pore size distribution and pore volume profiles of PdNPs⊃H_2P-CMP. (c), FE-SEM image of PdNPs⊃H_2P-CMP. (d), HR-TEM image of PdNPs⊃H_2P-CMP. (e), XRD patterns of H_2P-CMP (black; amorphous halo peak at 18°) and PdNPs⊃H_2P-CMP. (f), Size distribution profile of PdNPs. (g), XPS profile of PdNPs⊃H_2P-CMP.

in only microporous networks (**Figure 1c, d**). This method is general and applicable to other CMPs. [6a, 8b,9b] PdNPs⊃H_2P-CMP was prepared via impregnation of $Pd(NO_3)_2$ in H_2P-CMP dispersed in THF to generate Pd(II)-impregnated H_2P-CMP, followed by reduction under H_2 flow at 200 ℃. The PdNPs⊃H_2P-CMP assume a spherical shape with a size of 200-300 nm, as revealed by field-emission scanning electron microscopy (FE-SEM, **Figure 2a**). The average size of the PdNPs is 2.4 nm (**Figure 2b, c**), and the content of PdNPs in PdNPs⊃H_2P-CMP is 4.98 wt% as determined by using inductively coupled plasma atomic emission spectroscopy. PdNPs⊃H_2P-CMP is a highly porous dual-module material with a Brunauer–Emmett–Teller surface area of 1031 m^2 g^{-1} and pore volume of 1.03 cm^3 g^{-1} (**Figure 1d, e**); it contains both mesopores of 3.5 nm and micropores of 1.5 nm (**Figure 2d**). The contributions of mesopores and micropores to the total pore volume are 21% and 79%, respectively. Usually, porous materials upon loading of PdNPs leave low BET surface area and small pore volume in the resulted products. Notably, the PdNPs⊃H_2P-CMP preserves a high BET surface area and large pore volume, as a result of highly porous and dual-module structure of H_2P-CMP. Such a porous structure benefits the transport of reactants into and products out of the heterogeneous catalysts. High-resolution transmission electron microscopy (HR-TEM) revealed that PdNPs in PdNPs⊃H_2P-CMP are crystals with clear (111) facets that have a d-spacing of 2.24 Å (**Figure 2d**). X-ray diffraction (XRD) profiles of PdNPs⊃H_2P-CMP revealed a series of peaks at 40.7 °, 46.7 °, 68.2 ° and 82.2 °, which are assigned to the (111), (200), (220) and (311) facets, respectively (**Figure 2e**). X-ray photoelectron spectroscopy (XPS) measurements indicate a reduced Pd(0) state on the basis of the characteristic peaks at 334.7 and 340.3 eV, which are assigned to Pd $3d_{5/2}$ and Pd $3d_{3/2}$ electrons, respectively (**Figure 2g**). The small peaks at 336.1 and 341.2 eV are assignable to Pd(II) $3d_{5/2}$ and Pd(II) $3d_{3/2}$ electrons, respectively. The molar ratio of Pd(0) to Pd(II) is estimated to be 97:3 in the CMPs as evaluated from the XPS curves.

H_2P-CMP with an extended π-conjugation network, as indicated by its red-shifted Soret absorption band (**Figure 3a**), constitutes an electron-rich environment that electronically stabilises the uncovered PdNPs. [12a-c] In the PdNPs⊃H_2P-CMP, the mesopores (3.5 nm) are much larger than the average size (2.4 nm) of PdNPs, in addition to the presence of micropores, thus leaving sufficient space for mass transfer to PdNPs. The dual-module porous structure helps lock PdNPs

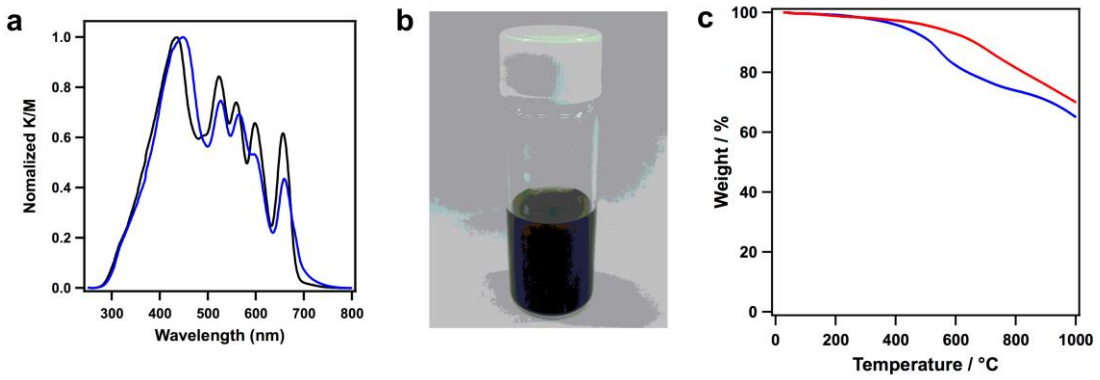

Figure 3. a) UV-vis spectrum for [p-Br]$_4$-H$_2$P (black curve) and H$_2$P-CMP (blue curve); b) An image of PdNPs⊃H$_2$P-CMP (10 mg) dispersed in neat water (2 mL); c) Thermogravimetric curve of H$_2$P-CMP (blue curve) and PdNPs⊃H$_2$P-CMP (red curve)

within the mesopores because PdNPs are too large to pass through the micropores. PdNPs⊃H$_2$P-CMP is stably dispersible in neat water (**Figure 3b**) and is thermally stable up to 500 ℃ (**Figure 3c**).

The Suzuki cross-coupling reactions of various aryl chlorides with arylboronic acids were investigated in the presence of the PdNPs⊃H$_2$P-CMP catalyst (**Table 1**). Suzuki coupling reactions are typically conducted in organic solvents or in aqueous-organic mixed solvents. The use of neat water as an environmentally benign solvent has received considerable attention with respect to green chemistry. The heterogeneous catalytic reaction was carried out in neat water at 80 ℃ (**Table 1**). A phase-transfer reagent, tetrabutylammonium bromide (TBAB), was added to enhance the reactivity in water. As a result, I was able to lower the catalyst loading to 0.5 mol%. Outstanding catalytic activity was observed for the coupling reaction of chlorobenzene (entry 1) and activated aryl chlorides, such as 4-chlorobenzonitrile (entries 2 and 3), 4-acetyl-1-chlorobenzene (entry 4), 1-chloro-4-formyl-benzene (entry 5), 1-chloro-4-fluoro-benzene (entry 6) and 1-chloro-4-nitrobenzene (entry 7), with phenylboronic acid.

High activities were achieved using the PdNPs⊃H$_2$P-CMP catalyst for deactivated aryl chlorides, such as 1-chloro-4-methyl-benzene (entry 8), 1-chloro-4-methoxy-benzene (entry 9) and 1-chloro-3-methyl-benzene (entry 10). PdNPs⊃H$_2$P-CMP catalysed efficiently non-robust hetero cross-coupling reactions in which steric hindrance at ortho-positions relative to the chlorid.

Table 1. Suzuki cross coupling reactions of aryl chlorides with aryl boronic acids under thermal[a] and microwave[b] conditions.

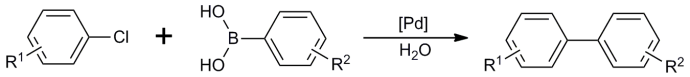

Entry	R^1	R^2	Product	Yield (%)[c]
1	H-	H-	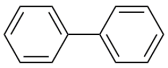	96[a]/95[b]
2	4-Me-	4-Me-	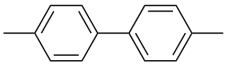	94/96
3	4-MeO-	H-	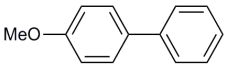	94/92
4	4-CN-	4-CN-	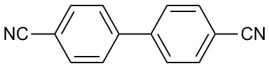	95/94
5	4-CN-	4-Me-	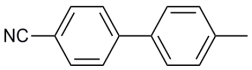	94/96
6	4-Acetyl-	H-	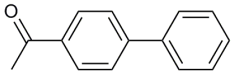	97/97
7	4-CHO-	H-	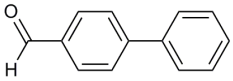	93/91
8	4-F-	H-	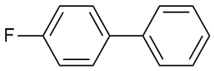	93/95
9	3-Me-	H-	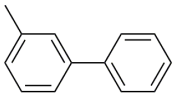	95/94
10	2-Me-	H-	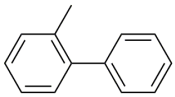	84/89
11	1,3-Me-	H-	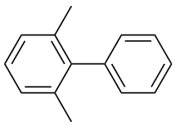	82/86
12	2-CN-	4-Me-	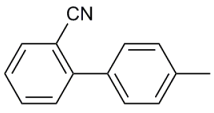	89/95
13	4-NO_2-	4-MeO-	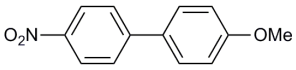	91/94
14	H-	H-	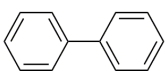	58/62
15	H-	H-	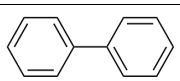	54/61

[a] Condition: aryl chlorides (0.5 mmol), arylboronic acids (0.75 mmol), PdNPs⊃H_2P-CMP (0.5 mol% Pd), TBAB (0.5 mmol), 1.5 M KOH aqueous solution (1 mL), 80 ℃, 12 h, Ar. [b]

Condition: aryl chlorides (0.5 mmol), arylboronic acids (0.75 mmol), PdNPs⊃H_2P-CMP (0.5 mol% Pd), 1.5 M KOH aqueous solution (1 mL), microwave, 100 ℃, 25 min, Ar. [c] Isolated yields after purified by chromatography. [d] 0.5 mol% of Pd (5 wt% Pd/C). [e] 0.5 mol% of Pd (5 wt% Pd/Al_2O_3). [f] 0.5 mol% of $Pd(OAc)_2$.

group are unreactive and are typically difficult to accomplish.[12d] Notably, the PdNPs⊃H_2P-CMP catalyst successfully facilitated the coupling reactions of the severely deactivated aryl chlorides, such as 2-chlorotoluene (entry 11), 2-chlorobenzonitrile (entry 12) and 1-chloro-2, 5-dimethyl-benzene (entry 13), with phenylboronic acid. These coupling reactions were achieved in excellent yields. Phenylboronic acids with different substituents, such as 4-cyano-phenylboronic acid (entry 2), 4-methylphenylboronic acid (entries 3, 8 and 12) and 4-methoxyphenylboronic acid (entry 7), are favourable for catalysis by PdNPs⊃H_2P-CMP. All of the coupling reactions, irrespective of the types and positions of the substituent groups, proceeded cleanly and highly efficiently in water.

The Suzuki coupling reaction catalysed by PdNPs⊃H_2P-CMP was promoted using microwave irradiation at 100 ℃ with the same catalyst loading of 0.5 mol% (**Table 1**). The reaction time was shortened from 12 h to only 25 min while preserving the high yields (**Table 1**). Remarkably, the coupling of phenylboronic acid with unreactive aryl chlorides such as 2-chlorotoluene (entry 11), 2-chlorobenzonitrile (entry 12) and 1-chloro-2,5-dimethyl-benzene (entry 13), proceeded smoothly and achieved high yields upon 25-min microwave irradiation.

The coupling reaction of chlorobenzene and phenylboronic acid was further performed in the presence of commercially available Pd catalysts, including heterogeneous catalysts Pd/C and Pd/Al_2O_3 and the authentic homogeneous catalyst $Pd(OAc)_2$, and gave rise to rather low yields (entries 14–16). To the best of my knowledge, PdNPs⊃H_2P-CMP exhibits the highest catalytic activity reported to date for the heterogeneous Suzuki coupling reactions of aryl chlorides.

Encouraged by the notable catalytic performance of PdNPs⊃H_2P-CMP in the Suzuki coupling reaction, I performed a Sonogashira coupling reaction of aryl chlorides with alkynes in

Table 2. Sonogashira cross coupling reaction of aryl chlorides with terminal alkynes under thermal[a] and microwave[b] conditions.

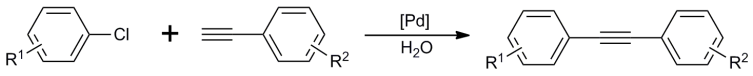

Entry	R^1	R^2	Product	Yield (%)[c]
1	H-	H-	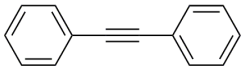	95[a]/96[b]
2	4-Me-	H-	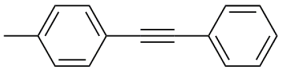	92/95
3	4-MeO-	H-	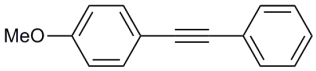	94/95
4	4-NO_2-	H-	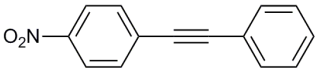	95/95
5	4-Acetyl	H-	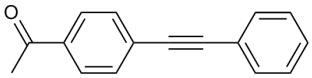	94/96
6	4-Me-	4-Me-	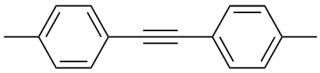	95/94
7	4-NO_2-	4-MeO-	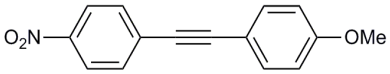	96/94
8	2-Cl-Py[d]	4-EtO_2C-	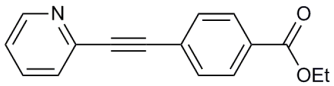	88/90
9	4-CF_3-	H-	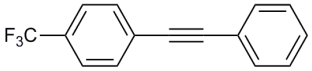	96/96
10	4-Et-	4-MeO-	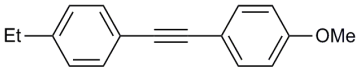	89/92

[a] Condition: aryl chlorides (0.5 mmol), alkynes (0.6 mmol), PdNPs⊃H_2P-CMP (0.5 mol% Pd), TBAB (0.5 mmol), 1.5 M Cs_2CO_3 aqueous solution (1 mL), 80 ℃, 8 h, Ar. [b] Condition: aryl chlorides (0.5 mmol), alkynes (0.6 mmol), PdNPs⊃H_2P-CMP (0.5 mol% Pd), TBAB (0.5 mmol), 1.5 M Cs_2CO_3 aqueous solution (1 mL), microwave, 100 ℃, 20 min, Ar. [c] Isolated yields after purified by chromatography. [d] 2-Chloropyridine.

the presence of the PdNPs⊃H_2P-CMP catalyst. Typically, the use of aryl chlorides requires a high catalyst loading, elevated reaction temperature, prolonged reaction time and the use of either CuI as co-catalyst or large amounts of ligands such as phosphines.[9d] Remarkably, I was able to conduct efficient ligand and copper-free Sonogashira coupling reactions of various aryl chlorides at 80 ℃ in the presence of PdNPs⊃H_2P-CMP in neat water without enhanced catalyst loading

(**Table 2**). High activity was achieved for the reactions of phenylacetylene with chlorobenzene (entry 1) and activated aryl chlorides, such as 1-chloro-4-nitrobenzene (entries 2 and 3), 1-chloro-4-acetylbenzene (entry 4) and 1-chloro-4-trifluoromethylbenzene (entry 5). The coupling reactions of these aryl chlorides are achieved in 94-96% yields. Deactivated aryl chlorides such as 4-chloro-toluene (entries 6 and 7), 1-chloro-4-methoxybenzene (entry 8) and 1-chloro-4-ethylbenzene (entry 9) were efficiently activated by PdNPs⊃H_2P-CMP to afford good yields. In addition to aryl chlorides, a heteroaryl chloride, 2-chloropyridine (entry 10), which is particularly detrimental to the catalytic activity of palladium, was readily activated by PdNPs⊃H_2P-CMP to give high yield. Notably, severely deactivated aryl chlorides such as 2-chlorobenzonitrile (entry 11) and 1-chloro-2, 5-dimethyl-benzene (entry 12) reacted with phenylacetylene effectively and achieved satisfactory yields of 84% and 90%, respectively, without requiring a higher reaction temperature or an enhanced loading of the catalyst. The PdNPs⊃H_2P-CMP exhibited high activity, regardless of the presence of activated and deactivated substituents, toward phenylacetylene (entries 3, 5, 7, 9 and 10). Notably, this is the first successful example of a heterogeneous PdNP catalyst for the Sonogashira reaction of aryl chlorides in neat water. Microwave irradiation also promoted the Sonogashira couplings catalysed by PdNPs⊃H_2P-CMP. As shown in **Table 2**, the reaction time was significantly shortened, to 20 min, whereas the yields were improved to 90–96%, irrespective of substituents on both reactants.

On the basis of these results, I conducted the Stille coupling reaction of aryl chlorides with organostannanes in the presence of PdNPs⊃H_2P-CMP in neat water at 80 ℃ (**Table 3**). To my best knowledge, heterogeneous catalysts that activate aryl chlorides for the Stille reaction in water have been very limited.[6c] The reaction of chlorobenzene (entry 1), activated aryl chlorides, such as 4-acetyl-1-chlorobenzene (entry 2), 1-chloro-4-formylbenzene (entry 3), 1-chloro-4-fluorobenzene (entry 4) and 1-chloro-3-nitrobenzene (entry 5) with trimethyl(phenyl)stannane proceeded smoothly in 5 h, with complete conversion and high yields of 93–96%. Satisfyingly, deactivated 1-chloro-4-methoxybenzene was efficiently converted in 5 h, with an impressive yield of 94% (entry 6). Furthermore, for severely deactivated 2-chlorotoluene (entry 7), 2-chlorobenzonitrile (entry 8) and 1-chloro-2, 5-dimethyl-benzene (entry 9), the Stille

reaction catalysed by PdNPs⊃H_2P-CMP afforded noteworthy yields of 94%, 86% and 88%, respectively; no prolonged reaction times or elevated reaction temperatures are required. To my

Table 3. Stille cross coupling reaction of aryl chlorides with trimethyl(phenyl)tin under thermal[a] and microwave[b] conditions.

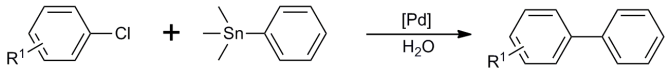

Entry	R^1	Product	Yield (%)[c]
1	H-	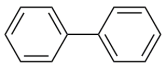	97[a]/96[b]
2	4-MeO-	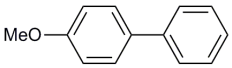	94/95
3	4-Acetyl	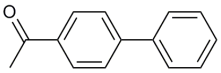	96/96
4	4-CHO-	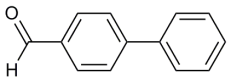	94/95
5	4-F-	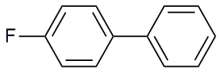	95/97
6	3-NO_2-	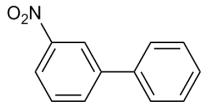	93/96
7	2-Me-	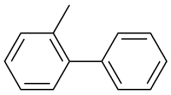	94/93

[a] Conditions: aryl chlorides (0.5 mmol), trimethyl(phenyl)tin (0.6 mmol), PdNPs⊃H_2P-CMP (0.5 mol% Pd), TBAF (1.5 mmol), 80 ℃, 5 h, Ar. [b] Conditions: aryl chlorides (0.5 mmol), trimethyl(phenyl)tin (0.6 mmol), PdNPs⊃H_2P-CMP (0.5 mol% Pd), TBAF (1.5 mmol), microwave, 100 ℃, 15 min, Ar. [c] Isolated yields after purified by chromatography.

knowledge, this result also represents the first example of a MNP-catalysed heterogeneous Stille coupling reaction of aryl chlorides. Under microwave irradiation at 100 ℃, the Stille coupling of aryl chlorides with organostannne was further promoted; PdNPs⊃H_2P-CMP completely converts all of the aryl chlorides, reaching high yields in only 15 min, irrespective of their substituents (**Table 3**).

PdNPs⊃H_2P-CMP efficiently catalyses aryl chlorides in Suzuki, Sonogashira and Stille coupling reactions. One of the structural features of PdNPs⊃H_2P-CMP is the uncovered PdNPs with a catalytically active Pd(0) surface that is readily accessible to aryl chlorides. Mechanistically, oxidative addition of aryl chlorides to Pd(0) is the key step for the coupling reaction. The superb catalytic activity observed for PdNPs⊃H_2P-CMP indicates that PdNPs⊃H_2P-CMP facilitates the oxidative addition step as well as the reductive elimination.

I evaluated the turnover number (TON) and turnover frequency (TOF) with 0.02 mol% Pd for the aforementioned three types of C–C bond formation reactions using 50 mmol of chlorobenzene under microwave irradiation conditions. Remarkably, for the Suzuki coupling of chlorobenzene and phenylboronic acid, the yield was 96% after 45 min; thus, the TON and TOF were 4800 and 6400 h^{-1}, respectively. The Sonogashira reaction of chlorobenzene and phenylacetylene reached 98% yield in 30 min; the TON and TOF were evaluated to be 4900 and 9800 h^{-1}, respectively. In the Stille reaction of chlorobenzene and trimethyl(phenyl)stannane, 96% yield was achieved in 20 min; the TON and TOF were 4800 and 14400 h^{-1}, respectively. Most of the heterogeneous PdNP catalytic systems have not been evaluated their TON and TOF values. The reaction yields are given in percentage when the Pd catalysts utilized the aryl chlorides as substrates.

Kinetic studies were conducted through the entire reaction region between 0% and 100% conversion, with each experiment performed at least in duplicate, whereas the average conversions were used for kinetics evaluations. The decease of chlorobenzene (open circles) and increase of the product (filled circles) in the coupling reactions are straightforward and the catalytic reactions proceed smoothly (**Figure 4a-c**). It is noteworthy that no induction periods are observable for these surface-exposed metal nanoparticle heterogeneous catalytic systems.

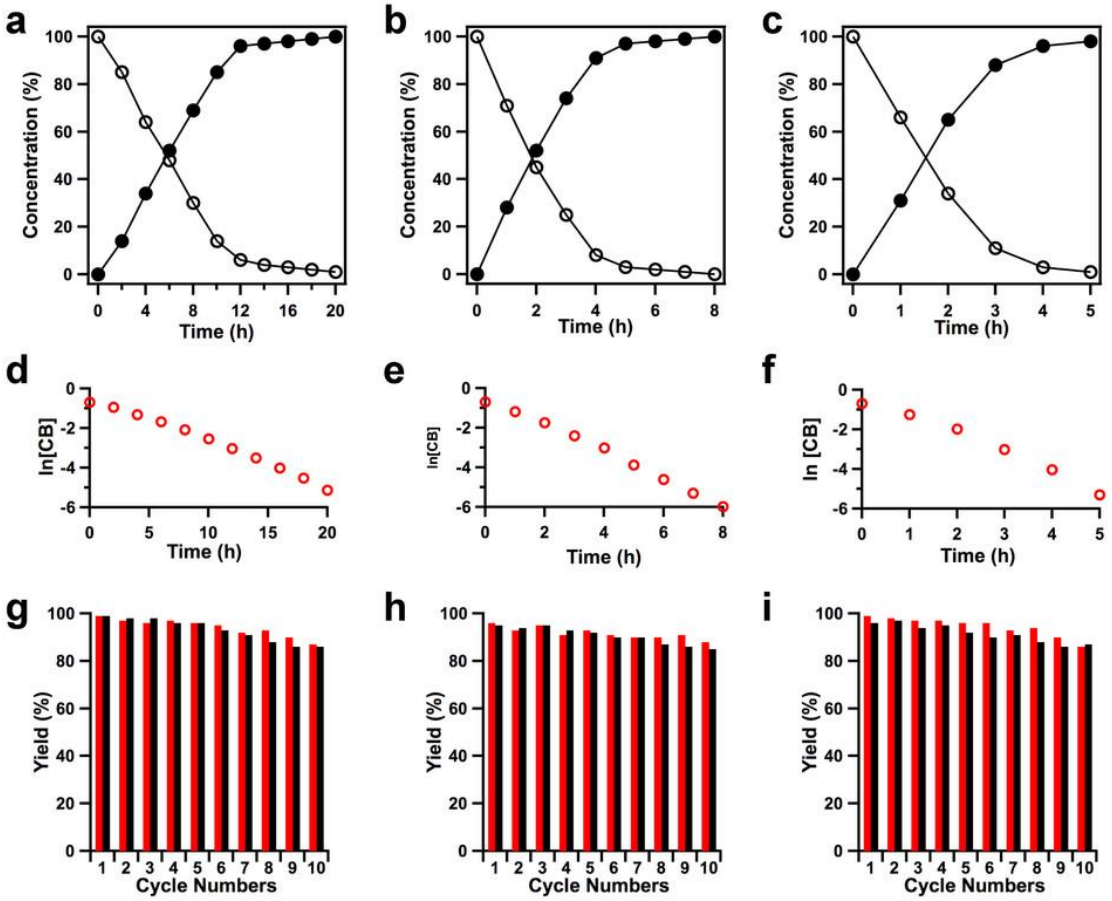

Figure 4. (a–c), Kinetics of (a) Suzuki, (b) Sonogashira and (c) Stille coupling reactions between chlorobenzene (CB) and phenylboronic acid phenylacetylene or trimethyl(phenyl)stannane (open circle: the remained CB concentration relative to loading concentration; filled circle: the coupling product concentration). (d–f), Plot of natural logarithm of the remained concentration of CB during reaction vs. time in (d) Suzuki, (e) Sonogashira and (f) Stille coupling reactions. (g–i), Recycling of PdNPs⊃H_2P-CMP (0.5 mol% Pd) for (g) Suzuki, (h) Sonogashira and (i) Stille coupling reactions under thermal (red bar) and microwave (black bar) conditions.

Under the reported conditions, all of the model reactions showed apparent first-order behavior (**Figure 4d-f**), consistent with a zero-order dependence on phenylboronic acid, phenylacetylene and trimethyl(phenyl)stannane. The rate constant (k_{obs}) and lifetime ($t_{1/2}$) were calculated to be k_{obs} = 0.222 ± 0.006 h^{-1} and $t_{1/2}$ = 4.96 h for Suzuki reaction, k_{obs} = 0.704 ± 0.014 h^{-1} and $t_{1/2}$ = 1.96 h for Sonogashira reaction and k_{obs} = 0.920 ± 0.027 h^{-1} and $t_{1/2}$ = 1.64 h for Stille reaction. The average catalytic productivity and activity of PdNPs⊃H_2P-CMP are increased in the order of Suzuki, Sonagashira and Stille reactions. A plausible explanation for the observed

first-order rate may involve the oxidative addition of aryl chlorides to the surface-exposed nanoparticle catalyst as the rate-determining step, while the capture of corresponding Pd-intermediates by phenylboronic acid, phenylacetylene or trimethyl(phenyl)stannane is immediate with a consequent rapid reductive elimination to yield the corresponding cross-coupling products.

A long catalyst lifetime and the capability of repeated use are highly desired for industrial applications. The PdNPs⊃H_2P-CMP catalyst is easily separated from the reaction mixture and recovered; filtration and subsequent rinsing with solvents and water refreshed the catalyst for the next reaction round. As for the heterogeneous PdNP catalysts thus far reported, their ability of cycle use for the activation of aryl chlorides remains unclear. In general, MNP catalysts undergo considerable agglomeration during reactions and finally lose activity. PdNPs⊃H_2P-CMP was subjected to repeated use for the Suzuki, Sonagashira and Stille coupling reactions under both thermal and microwave conditions. Notably, the PdNPs⊃H_2P-CMP catalyst retained its high activities and achieved high yields even after 10 cycles (**Figure 4g-i**), without the use of a prolonged reaction time or elevated reaction temperature. The PdNPs⊃H_2P-CMP catalyst exhibits

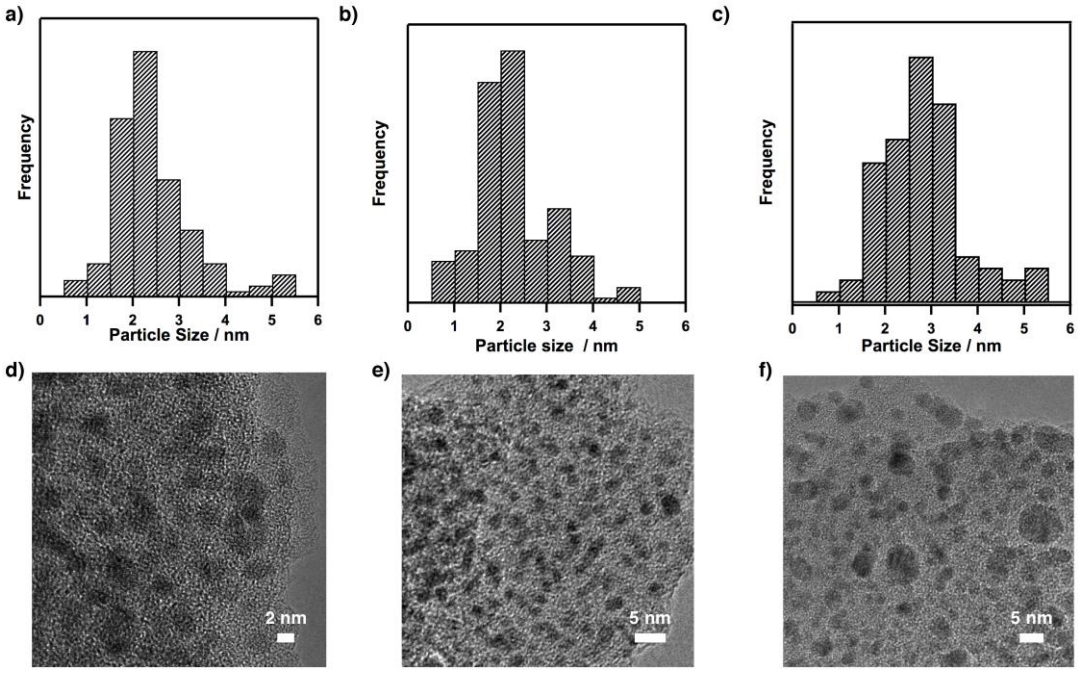

Figure 5. PdNPs size distribution of (a) as-synthesized, (b) after five cycles, and (c) after ten cycles. HR-TEM images of (c) as-synthesized, (d) after five cycles, and (e) after ten cycles, of PdNPs⊃H_2P-CMP.

the longest catalyst lifetime reported to date for heterogeneous carbon-carbon bond formation reactions. Together with the high activity and broad reactant scope, the excellent extended performance renders PdNPs⊃H_2P-CMP a more economic and environmentally benign process.

To gain structural insights into the extended performance of PdNPs⊃H_2P-CMP, I characterised the catalyst after 10 cycles using various analytical methods. Firstly, the size distribution of PdNPs was almost unchanged after ten cycles (**Figure 5a-c**), which suggests that the agglomeration of PdNPs was negligible (**Figure 5d-f**). Secondly, XRD measurements revealed that the crystal structure of PdNPs in PdNPs⊃H_2P-CMP was retained after 10 cycles (**Figure 6a**). The XPS profile suggests that PdNPs are retained in the Pd(0) state (**Figure 6b**). Thirdly, ICP-AES monitoring of the filtrates of the reaction mixtures revealed that no Pd was leached during 8 cycles, while was less than 0.01 mol% of the starting Pd catalyst in the filtrates of the reaction mixtures was detected after nine cycles. The Pd content in PdNPs⊃H_2P-CM after 10 cycles was 4.96 wt%, which is very close to that (4.98 wt%) of the pristine catalyst. These results indicate that PdNPs⊃H_2P-CMP is maintained within the pores of three-dimensional π-network, without losing its crystallinity and catalytic activity.

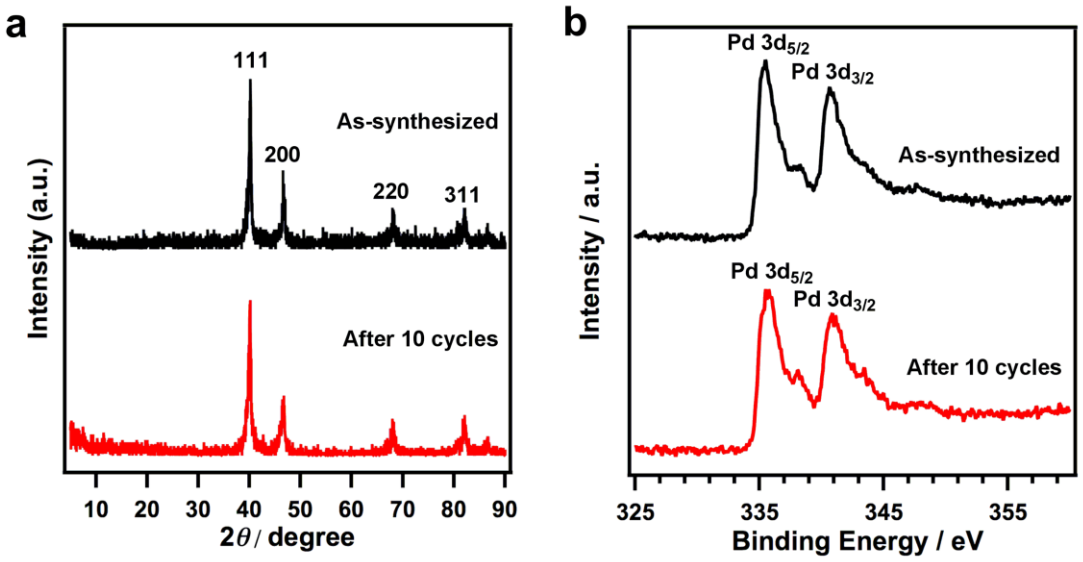

Figure 6. a) XRD profile of PdNPs⊃H_2P-CMP after ten cycles (red curve); b) XPS profile of PdNPs⊃H_2P-CMP after ten cycles (red curve).

Conclusion

In summary, I have developed the techniques for producing surface-exposed yet stable metal nanoparticles by locking them within a dual-module mesoporous and microporous three-dimensional π-network. The palladium nanoparticles exhibit inherently superior activity in the heterogeneous catalysis of different types of carbon–carbon bond formation reactions. Unreactive aryl chlorides are efficiently catalysed in Suzuki, Sonogashira and Stille coupling reactions in neat water under mild conditions. This novel class of heterogeneous catalysts, unlike previous examples thus far reported, combines activity, stability, reusability, versatility and environmental compatibility; these advantages offer a plausible solution to long-standing challenges for real applications in the field of heterogeneous catalyst. Therefore, these advancements open new perspectives in the design of heterogeneous catalysts for the sustainable production of fuels and chemicals. The present technique is applicable to producing various surface-exposed metal nanoparticles; utilization of this technique may disclose inherent functions and applications of other nanoparticles.

Experimental Sections

Materials and Methods ^{1}H and ^{13}C NMR spectra were recorded on a JEOL model JNM-LA400 NMR spectrometer, where the chemical shifts (δ in ppm) were determined with a residual proton of the solvent as standard. UV-Vis-IR diffuse reflectance spectrum (Kubelka-Munk spectrum) was recorded on a JASCO model V-670 spectrometer equipped with integration sphere model IJN-727. Matrix-assisted laser desorption ionization time-of-flight mass (MALDI-TOF MS) spectra were recorded on an Applied Biosystems BioSpectrometry model Voyager-DE-STR spectrometer in reflector or linear mode. Field-emission scanning electron microscopy (FE-SEM) was performed on a JEOL model JSM-6700 operating at an accelerating voltage of 5.0 kV. The sample was prepared by drop-casting a supersonicated suspension onto mica substrate and then coated with gold. X-ray diffraction (XRD) data were recorded on a Rigaku model RINT Ultima III diffractometer by depositing powder on glass substrate, from $2\theta = 1.5°$ up to $90°$ with $0.02°$ increment. Elemental analysis was performed on a Yanako CHN CORDER MT-6 elemental analyzer. TGA measurements were performed on a Mettler-Toledo model TGA/SDTA851 under N_2, by heating to 800 ℃ at a rate of 10 ℃ min^{-1}. The agitation of the reaction mixture was performed on a wrist-action shaker (Burrel Scientific, Inc.). X-ray photoelectron spectroscopy (XPS) measurements were performed in an integrated ultrahigh vacuum system equipped with multitechnique surface analysis system (VG ESCALAB MK II spectrometer). The metal contents in the solution were determined by ICP-AES (Teledyne Instruments Leeman Labs Inc.). Gas chromatographic (GC) analysis was performed on a Shimadzu GC-2010 system equipped with and FID detector and a capillary column of DB-5 (Agilent J&W, 0.25 mm i.d. × 30 m, 0.25 μm film thickness).

Nitrogen sorption isotherms were measured at 77 K with a Micromeritics Instrument Corporation model 3Flex surface characterization analyzer. Before measurement, the samples were degassed in vacuum at 120 ℃ for more than 10 h. The Brunauer-Emmett-Teller (BET) method was utilized to calculate the specific surface area. By using the non-local density functional theory (NLDFT) method, the pore volume was derived from the sorption curve.

Materials and synthetic procedures

Organic solvents for reaction were distilled over appropriate drying reagents under argon or obtained as dehydrated reagents from Kanto Chemicals. Deuterated solvents for NMR

measurement were obtained from Cambridge Isotope Laboratories, Inc. *p*-Bromobenzaldehyde, pyrrole, acetic acid and $Ni(COD)_2$ were obtained from Aldrich. 2, 2'-Bipyridine, COD and $Pd(NO_3)_2$ were purchased from Wako Chemicals.

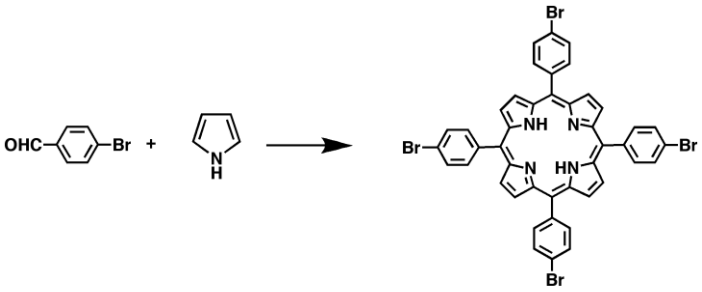

[*p*-Br]$_4$-H$_2$P

Synthesis of 5, 10, 15, 20-tetrakis(4'-bromophenyl)porphyrin ([*p*-Br]$_4$-H$_2$P). A mixture of *p*-bromobenzaldehyde (5.58 g, 30 mmol) in nitrobenzene (150 mL) and acetic acid (200 mL) was heated at 120 ℃ and then pyrrole (2.1 mL, 30 mmol) was added dropwise. The solution was stirred at 120 ℃ for 1h and cooled to room temperature. The brown violet precipitate was collected by filtration and washed with cooled methanol (100 mL× 3). The product was purified by recrystallization from $CHCl_3$/MeOH (1/3 by vol.), to give 5, 10, 15, 20-tetrakis(4'-bromophenyl)porphyrin as violet crystal (2.48 g) in 36% yield. ^{1}H NMR ($CDCl_3$, 400 MHz): δ (ppm) –2.87 (s, 2H, N–H), 7.91 (d, 8H, J = 8.2 Hz, Ar–H), 8.07 (d, 8H, J = 8.2 Hz, Ar–H), and 8.84 (s, 8H, pyrrole–H). MALDI-TOF MS: m/z 929.89, calcd. for $C_{44}H_{26}Br_4N_4$; found, $[M + H]^+$ 929.47

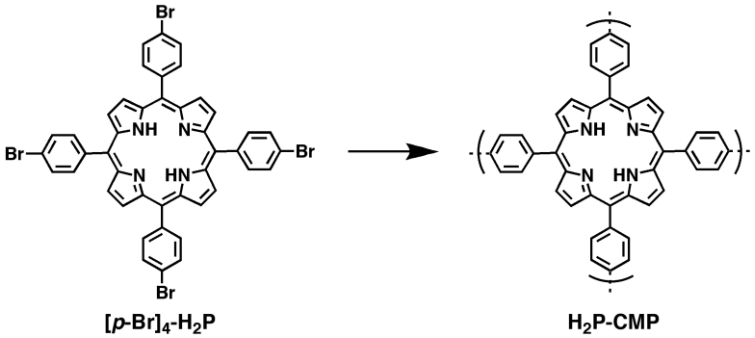

[*p*-Br]$_4$-H$_2$P **H$_2$P-CMP**

Synthesis of H$_2$P-CMP. 1,5-Cyclooctadiene (65 mg, 0.802 mmol) was added to a solution of bis(1,5-cyclooctadiene)nickel(0) (170 mg, 0.62 mmol) and 2, 2'-bipyridyl (96 mg, 0.62 mmol) in freshly distilled dehydrated dioxane (10 mL), and the mixture was heated at 90 ℃ for 1 h. To the purple mixture solution was added [*p*-Br]$_4$-H$_2$P (121 mg, 0.13 mmol), and the mixture was stirred

at 100 ℃ for 24 h to afford a deep purple suspension. After cooling to room temperature, concentrated HCl (4 mL) was added to the mixture. After filtration, the residue was washed with saturated aqueous EDTA solution (50 mL), H_2O (30mL × 5), $CHCl_3$ (30 mL × 5), and THF (30 mL × 5), extracted by Soxhlet with methanol, acetone, and THF for 2 days, respectively, and dried at 150 ℃ under vacuum overnight, to afford H_2P-CMP as red purple powders in 91% yield. Elemental analysis calcd. for $(C_{44}H_{26}N_4)n$ (theoretical formula for an infinite H_2P-CMP): C 79.16, H 3.62, N 8.39; found: C 72.96, H 4.28, N 7.67. FT IR (ν; cm^{-1}): 3056, 3027, 1603, 1489, 1349, 1072 (ν_{as} C-Br, weak), 966, 796, and 713. The isolated yield calculated based on the mass of H_2P-CMP and the monomer is 87-93%.

Synthesis of PdNPs⊃H_2P-CMP. 500 mg of H_2P-CMP was dispersed in 10 mL of THF and was stirred for 2 h at room temperature. A THF solution (1 mL) containing 150 mg $Pd(NO_3)_2$ $2H_2O$ was slowly added dropwise to the solution under vigorous agitation for 10 min. The 20 mL vial containing the slurry was subjected to ultrasounication for 30 min and was then magnetically agitated at room temperature for 48 h. The impregnated H_2P-CMP sample was washed with THF till the filtrate became colorless and then was slowly dried in air at room temperature for 24 h to obtain Pd^{II}⊃H_2P-CMP. The as-synthesized sample was further dried at 150 ℃ under vacuum overnight, followed by heating in a stream of H_2 at 200 ℃ for 6 h to yield PdNPs⊃H_2P-CMP. The Pd content in PdNPs⊃H_2P-CMP was evaluated to be 4.98 wt% by using ICP-AES.

Determination of Pd leaching in the coupling reactions. After reaction, the mixture was filtered in hot through celite, washed with deionized water and diethyl ether. An aliquot of the filtrate (10 mL) was boiled with concentrated HNO_3 and then subjected for ICP-AES analysis.

General procedure Suzuki coupling reactions under microwave irradiation. Aryl chlorides (0.50 mmol), arylboronic acids (0.75 mmol), PdNPs⊃H_2P-CMP (0.5 mol%), TBAB (0.5 mmol) and 1.5 M KOH aqueous solution (1 mL) were added to a 5 mL dry Schlenk tube with a stirring bar. Argon was bubbled through the solution for 10 min. The reaction mixture was heated with microwave irradiation at 100 ℃ (250 W) for 25 min and then cooled to room temperature. After separating the catalyst and the aqueous phase through centrifugation, the aqueous phase was decanted. The recovered catalyst was washed with THF (3 mL × 5) and water (3 mL × 5), which were then added to the aqueous phase. The filtrate was extracted with EtOAc (3 mL × 3), which

was dried over anhydrous magnesium sulfate and evaporated to dryness, to yield a crude product. The resulting solid was purified by silica gel column chromatography.

General procedure for Sonogashira coupling reaction under microwave irradiation. Aryl chlorides (0.5 mmol), alkynes (0.6 mmol), PdNPs⊃H_2P-CMP (0.5 mol%), TBAB (0.5 mmol) and 1.5 M Cs_2CO_3 aqueous solution (1 mL) were added to a 5 mL dry Schlenk tube with a stirring bar. Argon was bubbled through the solution for 10 min. The reaction mixture was heated with microwave irradiation at 100 ℃ (250 W) for 20 min and then cooled to room temperature. After separating the catalyst and the aqueous phase through centrifugation, the aqueous phase was decanted. The recovered catalyst was washed with THF (3 mL × 5) and water (3 mL × 5), which were then added to the aqueous phase. The filtrate was extracted with EtOAc (3 mL × 5), which was dried over anhydrous magnesium sulfate and evaporated to dryness, to yield a crude product. The resulting solid was purified by silica gel column chromatography.

General procedure for Stille coupling reaction under microwave irradiation. Aryl chlorides (0.5 mmol), trimethyl(phenyl)stannane (0.6 mmol), PdNPs⊃H_2P-CMP (0.5 mol%), TBAB (1.5 mmol) and water (1 mL) were added to a 5 mL dry Schlenk tube with a stirring bar. Argon was bubbled through the solution for 10 min. The reaction mixture was heated with microwave irradiation at 100 ℃ (250 W) for 15 min and then cooled to room temperature. After separating the catalyst and the aqueous phase through centrifugation, the aqueous phase was decanted. The recovered catalyst was washed with water (3 mL × 5) and THF (3 mL × 5), which were then added to the aqueous phase. The filtrate was extracted with EtOAc (3 mL × 5), which was dried over anhydrous magnesium sulfate and evaporated to dryness, to yield a crude product. The resulting solid was purified by silica gel column chromatography.

References

1. a) S. A. Maier, et al. *Nature Mater.* **2003**, *2*, 229-232; b) K.-S. Cho, et al. *Nature Photonics* **2009**, *3*, 341-345; c) A. S. Aricò, P. Bruce, B. Scrosati, J. M. Tarascon, and W. van Schalkwijk, *Nature Mater.* **2005**, *4*, 366-377; d) Tao, F. **2014**, RSC Publishing, Cambridge.
2. a) Y. Román-Leshkov, C. J. Barret, Z. Y. Liu, and J. A. Dumesic, *Nature* **2007**, *447*, 982-985; b) L. Kesavan, et al. *Science* **2011**, *14*, 195-199; c) Torres, G. et al. *Science* **2012**, *17*, 835–838; d) N. T. K. Thanha, L. A. W. Green, *Nano Today* **2010**, *5*, 213-230.
3. a) N. L. Rosi, C. A. Mirkin, *Chem. Rev.* **2005**, *105*, 1547-1562; b) Y. Wang, J. Zhang, W. Zhang, M. Zhang, *J. Org. Chem.* **2009**, *74*, 1923-1931; c) F. Wen, et al. *Chem. Mater.* **2008**, *20*, 2144-2150; d) B. J. Gallon, R. W. Kojima, R. B. Kaner, P. L. Diaconescu, *Angew. Chem., Int. Ed.*, **2007**, *46*, 7251-7254.
4. a) S. Ogasawara, S. Kato, *J. Am. Chem. Soc.* **2010**, *132*, 4608-4613; b) P. Zhang, Z. Weng, J. Guo, C. Wang, *Chem. Mater.* **2011**, *23*, 5243-5249; c) E. V. Johnston, et al. *Chem. Eur. J.* **2012**, *18*, 12202-12206; d) A. R. Siamaki, Y. Lin, K. Woodberry, J. W. Connell, B. F. Gupton, *J. Mater. Chem.* A **2013**, *1*, 12909-12918.
5. a) C. E. Chan-Thaw, et al. *Nano Lett.* **2010**, *10*, 537-541; b) L. Yin, J. Liebscher, *Chem. Rev.* **2007**, 107, 133-173; c) J. X. Jiang, et al. *Angew. Chem., Int. Ed.* **2011**, *50*, 1072-1075; d) L. Chen, Y. Yang, D. Jiang, *J. Am. Chem. Soc.* **2010**, *132*, 9138-9143.
6. a) C. A. Wang, et al. *Chem. Eur. J.* **2012**, *18*, 6718-6723; b) Y. Xie, T. Wang, X. Liu, K. Zou, W. Deng, *Nature Commun.* **2012**, *4*, 1960-1966; c) Y. Xu, S. Jin, H. Xu, D. Jiang, *Chem. Soc. Rev.* **2013**, 42, 8012-8031; d) J. X. Jiang, et al. *Angew. Chem., Int. Ed.* **2007**, *46*, 8574-8578 .
7. a)Y. Kou, Y. Xu, Z. Guo, D. Jiang, *Angew. Chem., Int. Ed.* **2011**, *50*, 8753-8757; b) L. Chen, Y. Yang, Z. Guo, D. Jiang *Adv. Mater.* **2011**, *23*, 3149-3154; c) X. Liu, Y. Xu, D. Jiang, *J. Am. Chem. Soc.* **2012**, *134*, 8738-8741; d) Y. Xu, L. Chen, Z. Q. Guo, A. Nagai, D. Jiang, *J. Am. Chem. Soc.* **2011**, *133*, 17622-17625.
8. a) Z. Wu, et al. *Adv. Mater.* **2013**, *26*, 1450-1455; b) C. Gu, N. Huang, J. Gao, F. Xu, Y. Xu, D. Jiang, *Angew. Chem., Int. Ed.* **2014**, *53*, 4850-4855; c) K. Zhang, D. Kopetzki, P. H. Seeberger, M. Antonietti, F. Vilela, *Angew. Chem., Int. Ed.* **2013**, *52*, 1432-1436; d) F. Xu, X. Chen, Z. Tang, D. Wu, R. Fu, D. Jiang *Chem. Commun.* **2014**, *50*, 4788-4790.

9. a) R. Dawson, et al. *Macromolecules* **2008**, *41*, 1591-1593; b) R. Jana, T. P. Pathak, M. S. Sig -man, *Chem. Rev.* **2011**, *111*, 1417-1492; c) G. Cahiez, A. Moyeux, *Chem. Rev.* **2010**, *110*, 1435-1462; d) N. Miyaura, A. Suzuki, *Chem. Rev.* **1995**, *95*, 2457-2483.

10. a) R. Chinchilla, C. Nájera, *Chem. Rev.* **2007**, *107*, 874-922; b) R. Martin, S. L. Buchwald, *Acc. Chem. Res.* **2008**, *41*, 1461-1473; c) A. F. Littke, G. C. Fu, *Angew. Chem., Int. Ed.* **2002**, *41*, 4176-4211; d) B. Yuan, Y. Pan, Y. Li, B. Yin, H. Jiang, *Angew. Chem., Int. Ed.* **2010**, *49*, 4054-4058.

11. a) M.-J. Jin, D.-H. Lee, *Angew. Chem., Int. Ed.* **2010**, *49*, 1119-1122 ; b) B. Li, et al. *Adv. Mater.* **2012** *24*, 3390-3395 ; c) R. N. Butler, A. G. Coyne, *Chem. Rev.* **2010**, *110*, 6302-6337; d) G. M. Scheuermann, L. Rumi, P. Steurer, W. Bannwarth, R. Mulhaupt, *J. Am. Chem. Soc.* **2009**, *131*, 8262-8270.

12. a) P. Zhang, Y. Gong, H. Li, Z. Chen, Y. Wang, *Nature Commun.* **2013**, *4*, doi:10.1038/ncomms2586; b) K. Okamoto, R. Akiyama, H. Yoshida, T. Yoshida, S. Kobayashi, *J. Am. Chem. Soc.* **2005**, *127*, 2125-2135; c) N. Kudo, N. Perseghini, G. C. Fu, *Angew. Chem., Int. Ed.* **2006**, *45*, 1282-1284; d) K. L. Billingsley, K. W. Anderson, S. L. Buchwald, *Angew. Chem., Int. Ed.* **2006**, *45*, 3484-3486.

Chapter 4

Controlled Synthesis of Conjugated Microporous Polymer Films: Versatile Platforms for Highly Sensitive and Label-Free Chemo- and Biosensing

Angew. Chem. Int. Ed. **2011**, *133*, 14510-14513

Cheng Gu,[†] Ning Huang,[†] Jia Gao, Fei Xu, Yanhong Xu and Donglin Jiang

([†] These authors contributed equally to this work.)

Abstract Conjugated microporous polymers (CMPs), in which rigid building blocks form robust networks, are usually synthesized as insoluble and unprocessable powders. I developed a methodology using electropolymerization for the synthesis of thin CMP films. The thickness of these films is synthetically controllable, ranging from nanometers to micrometers, and they are obtained on substrates or as freestanding films. The CMP films combine a number of striking physical properties, including high porosity, extended π conjugation, facilitated exciton delocalization, and high-rate electron transfer. I explored the CMP films as versatile platforms for highly sensitive and label-free chemo- and biosensing of electron-rich and electron-poor arenes, metal ions, dopamine, and hypochloroic acid, featuring rapid response, excellent selectivity, and robust reusability.

Keyword: biosensors; chemosensors; conjugated microporous polymers; electropolymerization; thin films

Introduction

Conjugated microporous polymers (CMPs) are a class of organic porous polymers that inherently combine π-conjugated skeletons with permanent nanopores, in sharp contrast to other porous materials that are not π-conjugated and conventional conjugated polymers that are nonporous.[1-3] As an emerging materials platform, CMPs feature a high flexibility in molecular design of conjugated skeletons and nanopores. Because of high surface areas and the microporous character, CMPs have emerged as a new class of porous materials for gas adsorption and storage.[1-3] The pores are accessible to various guest molecules and metal ions, which allow the construction of supramolecular structures and organic–inorganic hybrids.[1-3] Significantly, CMPs allow the complementary utilization of π conjugation and porosity to explore novel functions and have shown their high potential in the challenging of energy and environmental issues, as exemplified by their excellent performances in superabsorption,[3h] light emitting,[1, 3e,g] chemosensing,[3f] light harvesting,[3a] catalysis,[1, 2, 3b, c] and electric energy storage. [3d, k]

However, CMPs are usually obtained as powders, they are insoluble in any solvents, and it is difficult to obtain thin films of them.[1-4] A few approaches, including surface-initiated growing,[4a] layer-by-layer crosslinking,[4b] and hyperbranched structuring,[4c] have been reported to fabricate CMP films. However, these methods are tedious with regard to synthesis and structural control; the films thus prepared are nonporous. The development of a methodology for the synthesis of thin films with retained π conjugation and porosity is highly desired for the further advancement, but remains a substantial challenge.[1a] The difficulty to process CMPs hampers their applications in organic electronics; processability and device integration are highlighted as bottleneck issues of "paramount importance" in recent reviews of the CMP field.[1a, 3a] Herein, I report an electrochemical approach to the synthesis of CMP films. My CMP films combine intriguing physical properties, including extended π conjugation, facilitated exciton delocalization, and high porosity. I highlight that this methodology allows the control of thickness, size, and shape of the films, and affords freestanding thin films. To demonstrate the utility, I prepared photoactive CMP films, which are luminescent and exhibit fluorescence on/off chemo- and biosensing with rapid response, sensitivity, selectivity, and reusability.

Results and Discussion

I fabricated the CMP films using electropolymerization with concurrent polymer film deposition, which has been proven to be an especially useful method for the preparation of electroactive and conducting polymer films.[5] Generally, in this method, the precursors are oxidized electrochemically and the coupling reaction between the precursors occurs at the electrode surface with deposition of the crosslinked polymer network film onto the electrode. I synthesized the CMP precursor TPBCz, which bears a 1,3,5-triphenylbenzene focal core with three N-substituted carbazole groups at the periphery (**Scheme 1 a**). The N-substituted carbazole is well established as a highly electroactive compound, which has a relatively low oxidative potential. It enables the effective coupling reaction between its oxidative species (radical carbazyl cation) and produces only dimers.[5] These unique characteristics allow the precise control of the structure and properties of resulting CMP films. TPBCz with its triangular, twisted, and rigid focal structure was designed to bear three N-substituted carbazole groups linked in a C_3 geometry, which upon electrochemical reaction guarantee the growth of thin films with a three-dimensional conjugated network, high porosity, and uniform pore distribution.[6]

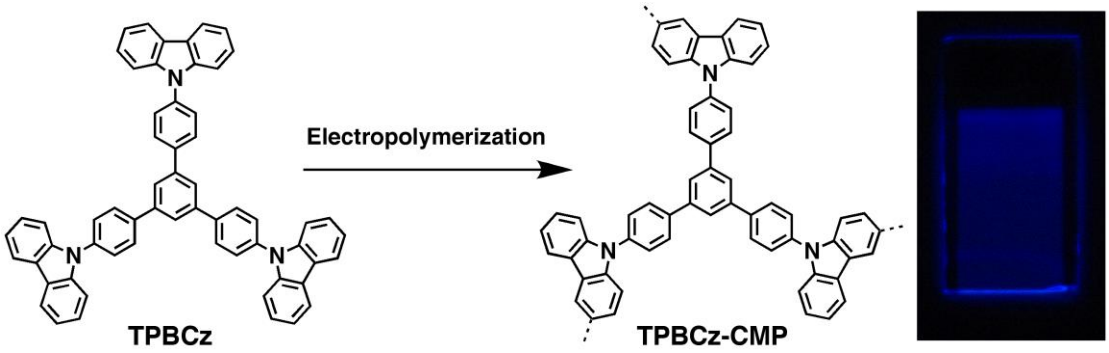

Scheme 1. a) Schematic representation of the electrochemical synthesis of TPBCz-CMP films. b) Elementary pore of the film. Photos of c) a film on an ITO substrate (0.5×1.5 cm2), d) the film under UV light, and e) a 100 nm thick freestanding film (0.5×1 cm2) in acetonitrile. Scale bars: 0.5 cm.

The TPBCz-CMP films were fabricated by multicycle cyclic voltammetry (CV) of TPBCz (1.25×10^{-3} m) in a mixture of acetonitrile and water (3/2 v/v) containing $LiClO_4$ as electrolyte in a

potential range from -0.8 to 0.7 V at room temperature. In the first cycle of the positive CV scan, the onset oxidative potential of TPBCz appeared at 0.64 V, which was attributed to the oxidation

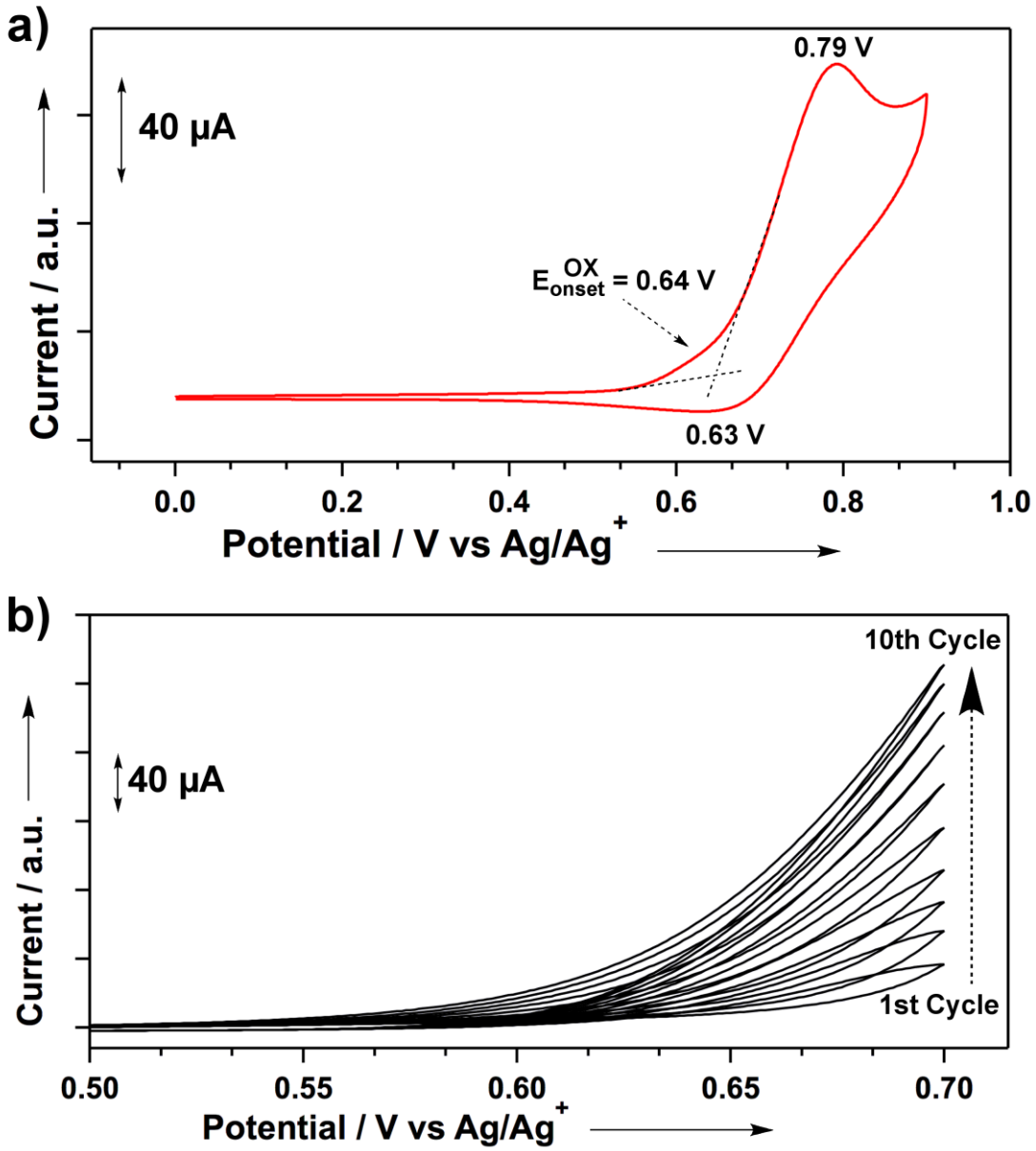

Figure 1. CV profiles of a) the 1st cycle and b) the 1st to 10th cycle of a solution of TPBCz in acetonitrile/water (3/2 v/v) in the presence of LiClO4 as electrolyte at 25 °C.

of carbazole (**Figure 1 a**).[5] At a scan potential of higher than 0.64 V, the anode current increased rapidly, indicating more carbazoles were oxidized. Previous studies have shown that upon oxidation, N-substituted carbazole transforms into the cationic radical, which effectively couples with another cationic radical to form a dimeric carbazole cation.[5, 7] During the negative scan, an

obvious reductive peak was observed at a potential of 0.63 V, which can be assigned to the reduction of dimeric carbazole cations. In the second cycle of a continuous CV scan (shown in

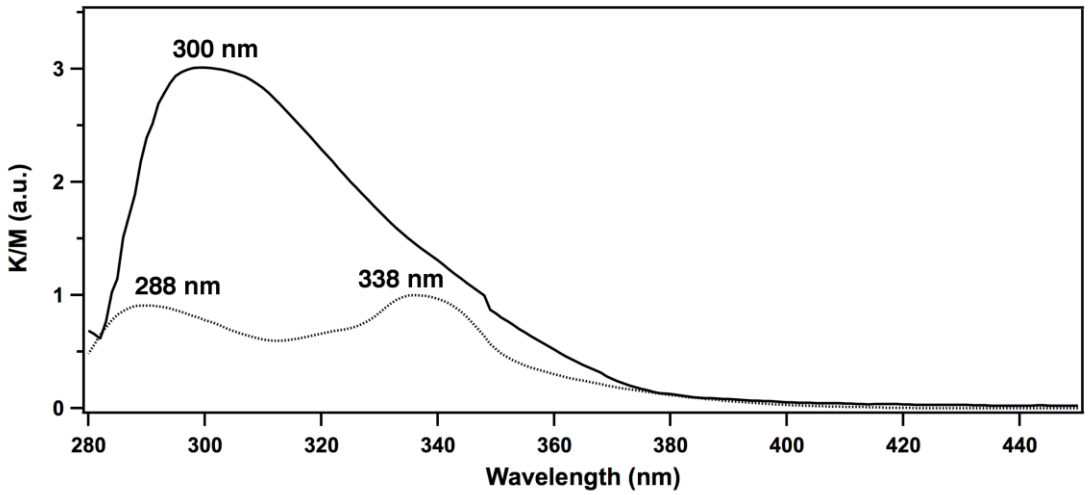

Figure 2. Normalized electronic absorption spectra of the CMP film (solid line) and spin-coated monomer film (dotted line).

Figure 1b), a new oxidative band appears at 0.60 V, which is due to the oxidation of dimeric carbazoles on the electrode.[5, 7] A distinct feature is that the current increases with the number of cycles, thus demonstrating the gradual growth of the TPBCz-CMP film on the electrode (**Figure 1b**). After ten CV cycles, the CMP films are transparent and exhibit a light-blue color (**Scheme 1 c**). The high reactivity and efficient coupling reaction of carbazoles are key to the synthesis of structurally well-defined CMP films, which are further studied by the following experimental investigations. First, the electronic absorption and infrared spectral analysis showed that the films are free of monomeric carbazole units (**Figures 2 and 3**). Second, the films are insoluble in organic solvents irrespective of polarity, which clearly reflects their highly crosslinked structure, in contrast to TPBCz, which is highly soluble in organic solvents such as acetonitrile (>50 mg mL^{-1}).

The thickness of CMP films can be precisely controlled by the numbers of scan cycles, with each cycle producing approximately 2.5 nm of film thickness using an oxidative potential of 0.7 V (**Figure 4a**). By employing this technique, I prepared a series of films with thicknesses ranging from several nanometers to several micrometers. When the thickness became larger than 50 nm, the films could automatically peel off the electrode to give freestanding CMP films (**Scheme 1 e**).

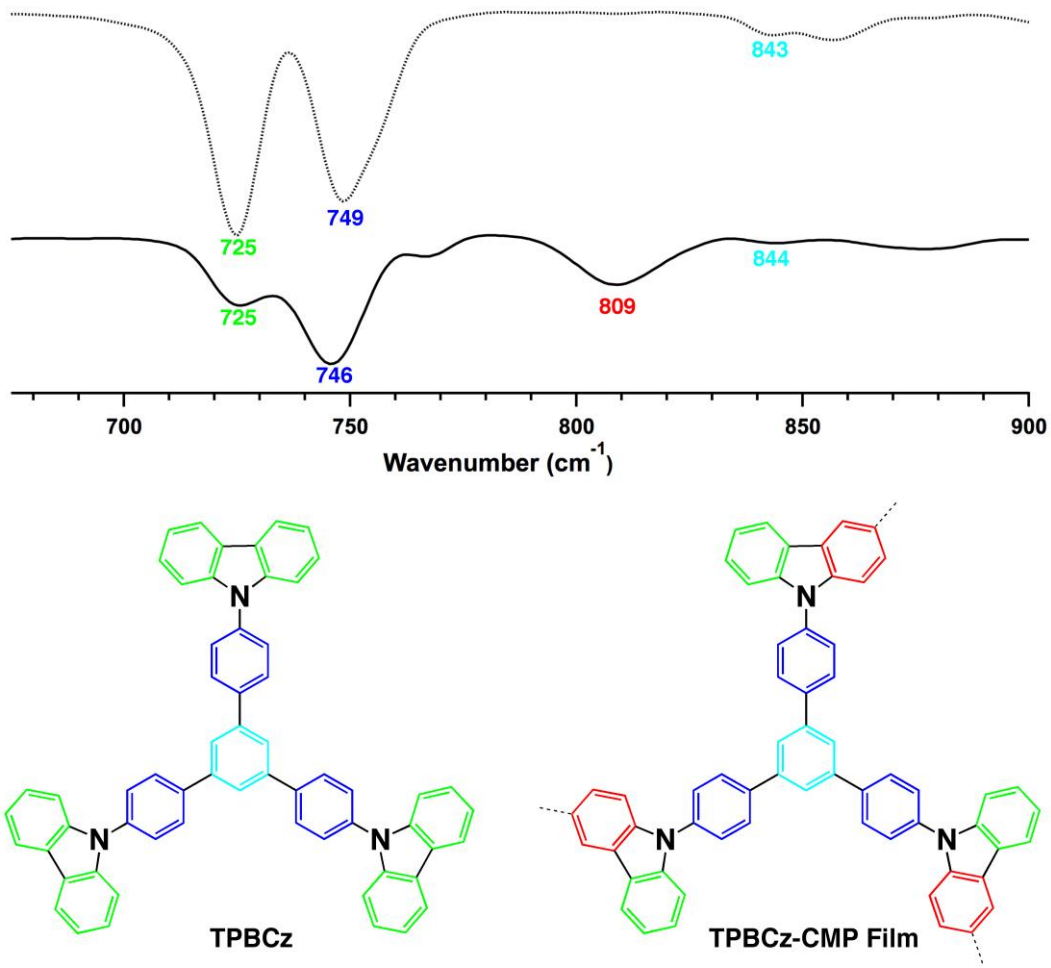

Figure 3. (a) FT-IR spectra of the TPBCz-CMP film (solid line) and monomer (dotted line), and their peak assignment (colored numbers correspond to vibrational bands of C–H bonds in different phenyl units).

The freestanding films only grew on the electrode and were of the same size and shape as the employed electrodes; in my studies, films with a size of up to 0.5×1.5 cm^2 were produced. The present method produces high quality films either on electrodes or in a freestanding form, with synthetically controlled thickness, size, and shape. I conducted Kr sorption isotherm measurements and found that these CMP films are highly porous and have a Brunauer-Emmett-Teller surface area of as high as 1450 $m^2 g^{-1}$ (Figure 5a). The thickness of the CMP films used for Kr sorption measurements was about 1 μm, which corresponds to a mass of 120 μg (two films on ITO (indium tin oxide)). I measured the Kr sorption curves for four lots of samples to assure the reproducibility. On the other hand, the BET surface area of a bulk CMP

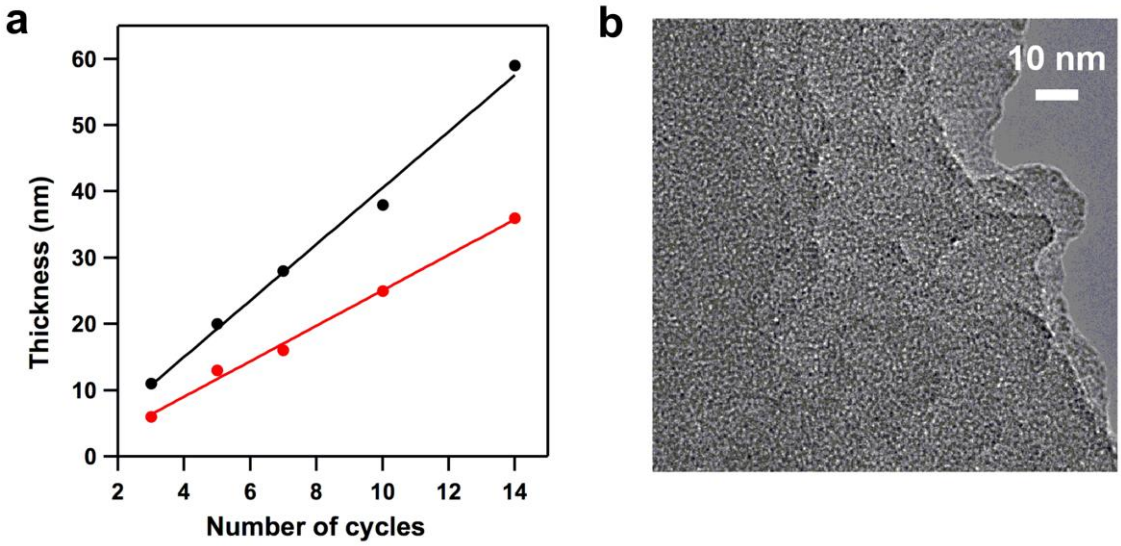

Figure 4. a) The thickness of the CMP films under different CV cycles and potentials (black line: –0.8 ~ 0.75 V; red line: –0.8 ~ 0.7 V; scan rate: 0.05 V s^{-1}); b) The HR TEM images of the CMP film.

sample prepared through oxidation polymerization in solution was much lower with only 135 m^2 g^{-1} (**Figure 5b**). High-resolution transmission electron microscopy supports the porous texture of the films (**Figure 4b**).

A spin-coated film of TPBCz monomers exhibited an absorption band at 338 nm, assignable to the π→π* transition of the triphenylbenzene focal unit, and a band at 288 nm, assignable to the π→π* transition of the N-substituted carbazole group (**Figure 3**). In the TPBCz-CMP films, the dimeric carbazole unit displayed an absorption band at 300 nm, which is 12 nm red-shifted compared to the spin-coated TPBCz film, and features a greatly enhanced absorption coefficiency. In this case, the band resulting from the focal triphenylbenzene unit was superimposed by the broad band resulting from the carbazole dimers. These results indicate an extended π conjugation in the CMP films. Upon excitation at 340 nm, the CMP film emitted a deep-blue luminescence (Scheme 1 d) with two peaks at 374 and 399 nm, respectively (Figure 6a). The absolute fluorescence quantum yield is 10 %. In contrast, the spin-coated TPBCz film gave a fluorescence spectrum similar to that of the CMP film, but its fluorescence quantum yield is only 1 %. The network structure in the CMP film greatly enhances the light-emitting activity.[3e] Since the CMP film allows an extended π conjugation, I further investigated the fluorescence depolarization profiles of the CMP films,

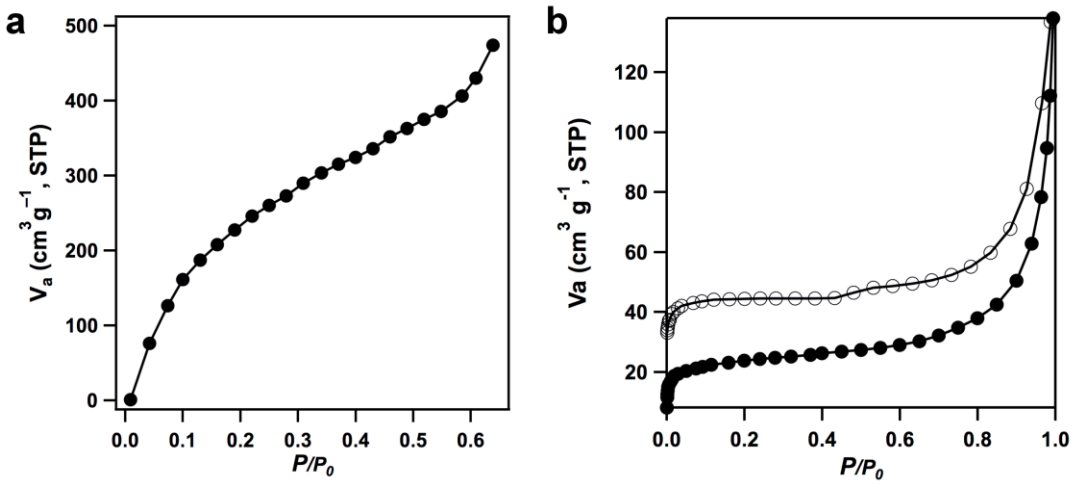

Figure 5. a) Kr sorption isotherm curve of the CMP films measured at 77 K. b) N_2 sorption isotherm curves of a bulk CMP sample measured at 77 K.

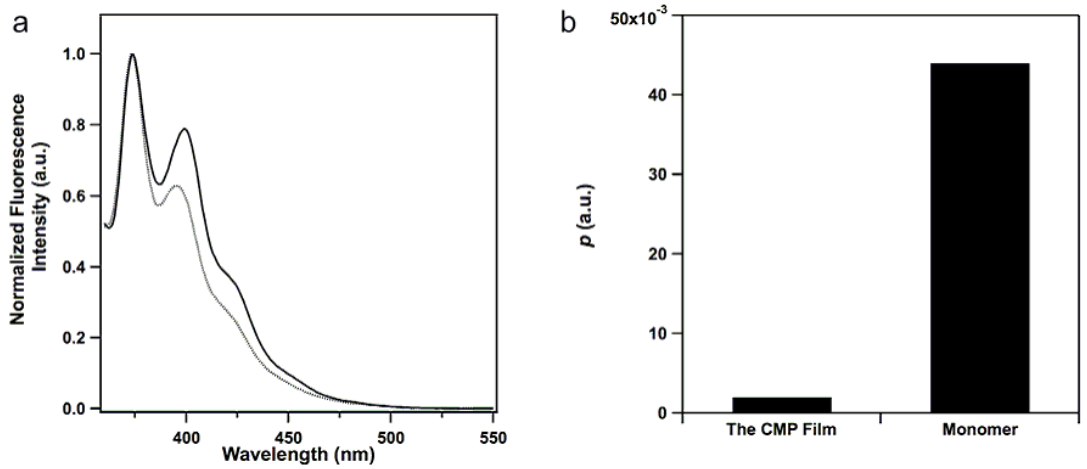

Figure 6. a) Nomalized fluorscence spectra of the CMP film (solid line) and monomer (dotted line) upon excitation at 340 nm; b) Fluorescence depolarization of the CMP film and monomer. Here, the degree of fluorescence depolarization (p) is defined as $p = (I_{//} - GI_{\perp})/ (I_{//} + GI_{\perp})$, whereas $I_{//}$ and $I_{\perp}$ are the fluorescence intensities of the parallel and perpendicular components relative to the polarity of the excitation light, respectively, while G is an instrumental correction factor.

which are considered to reflect the occurrence of photochemical events in the microporous network. The suppression of Brownian motion in a viscous medium should result in fluorescence depolarization occurring predominantly by exciton migration along the conjugated chain. The TPBCz monomer showed a fluorescence depolarization value of 0.044 in poly-ethylene glycol (**Figure 6b**). In contrast, the CMP film exhibited a significantly depolarized fluorescence with an extremely low depolarization value of 0.002. This observation demonstrates that the CMP film facilitates exciton migration over the network, which endows the film with a collective response, a key factor to enhance the sensitivity.

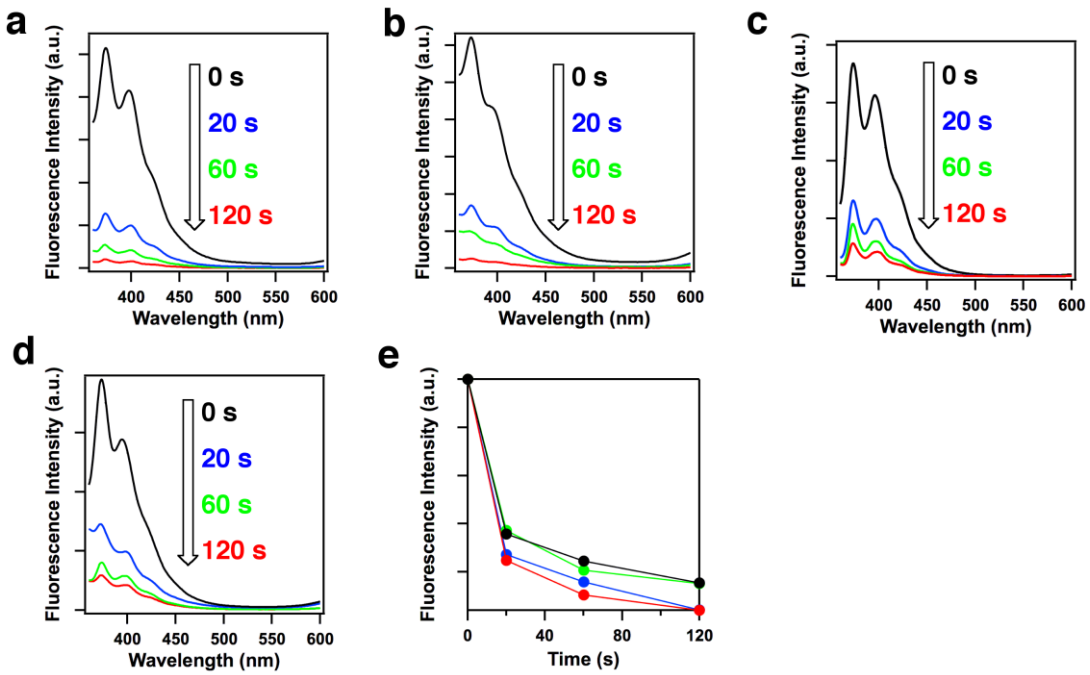

Figure 7. Fluorescence spectral changes of the CMP films with different thickness of (a) 5 nm, (b) 10 nm, (c) 15 nm, (d) 20 nm, upon exposure to the vapor of DNB for different period of time. (e) Normalized fluorescence intensity of the CMP films upon exposure to DNB vapor (blue: 5-nm thick film, red: 10-nm thick film, green: 15-nm thick film, black: 20-nm thick film).

Chemosensing experiments were conducted by exposing CMP films to arene vapors for specific periods of time at 25 °C followed by monitoring with fluorescence spectroscopy. The air was not removed from the micropores of the CMP films prior to their exposure to arene vapors. I first investigated the effect of the thickness of CMP films on the chemosensing properties. As shown in **Figure 7**, the CMP film with a thickness of 10 nm exhibited the best performance. For

each chemosensing experiment, several individual CMP films with a thickness of 10 nm were used in parallel experiments, and the results showed excellent reproducibility.

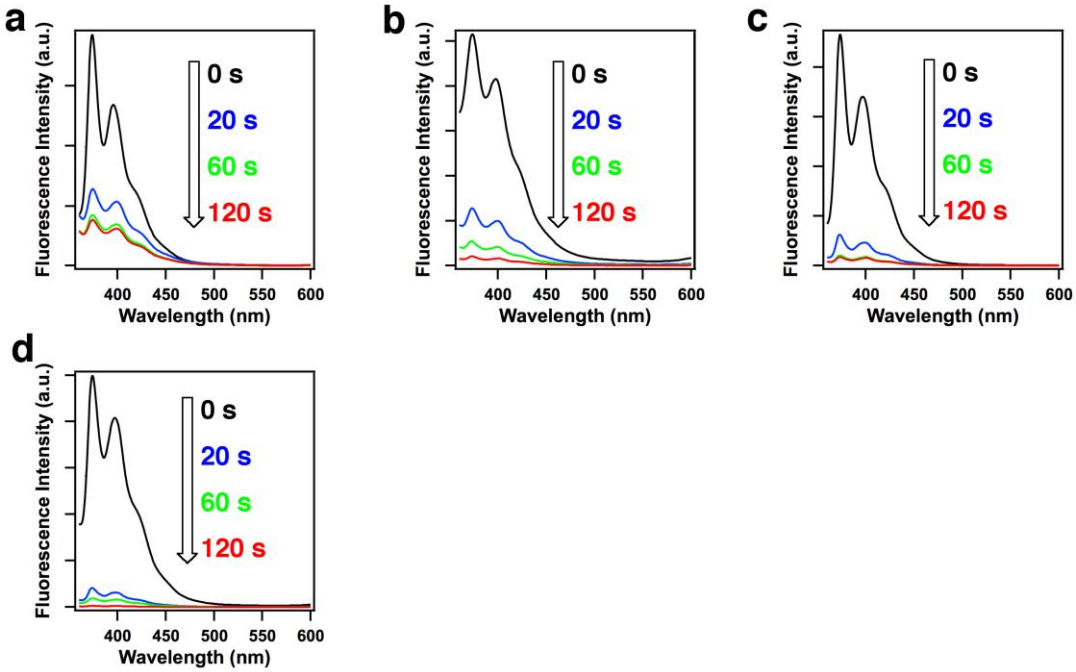

Figure 8. Fluorescence spectral changes of the CMP films upon exposure to the vapors of (a) BN, (b) DNB, (c) HFB, and (d) BQ for different period of time.

The CMP films are extremely sensitive to arenes, as shown in **Figures 8** and **10**. For example, upon exposure to the vapor of benzonitrile (BN) for only 20 s, the fluorescence of the CMP films was significantly quenched (**Figure 10 a**, black line), and only 33 % of the intensity of the pristine CMP film remained. As the exposure time was prolonged, further quenching was observed, and the fluorescence gradually settled at 20 % of its original intensity. Interestingly, the fluorescence-off chemosensing was not specific to BN, but was widely applicable to other electron-deficient arenes. The CMP films exhibited an enhanced response to 1,2-dinitrobenzene (DNB) with 75 % of the fluorescence quenched upon exposure for 20 s (**Figure 10 a**, red line). Notably, 87 % of the fluorescence was quenched upon exposure to hexafluorobenzene (HFB) for 20 s (**Figure 10 a**, blue line). The most explicit quenching of fluorescence was observed with 1,4-benzoquinone (BQ). A 20 s exposure resulted in a 92 % loss of fluorescence (**Figure10 a**,

green line and photos). After 120 s exposure, the fluorescence of CMP films was completely quenched.

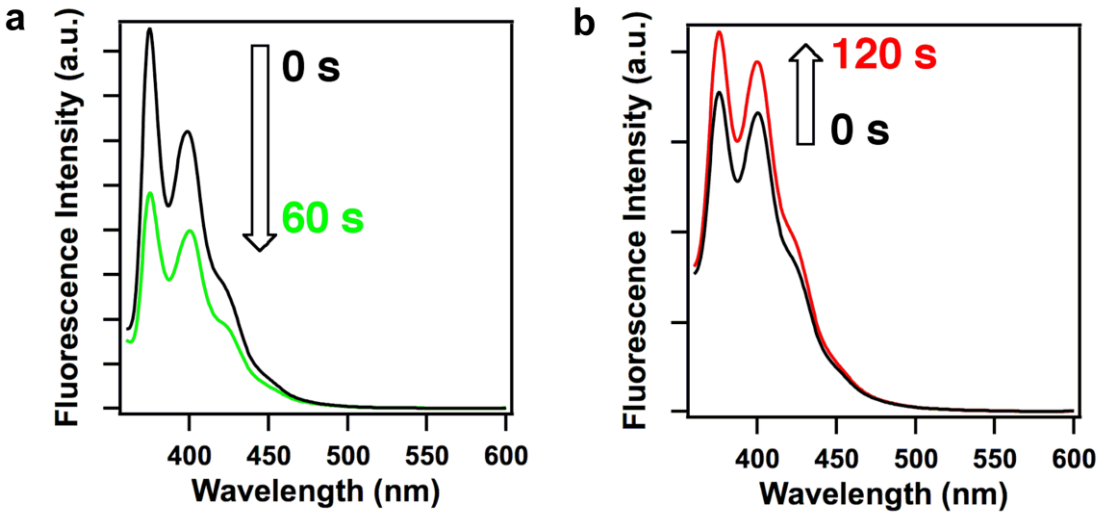

Figure 9. a) Fluorescence spectral change of spin-coated monomer film upon exposure to the vapors of BQ for 60 s; b) Fluorescence spectral changes of the spin-coated TPBCz film upon exposure to the vapors of CB for 120 s.

The degree of fluorescence quenching is in good agreement with the trend in the lowest unoccupied molecular orbital (LUMO) of arenes, as a result of an enhanced driving force for photoinduced electron transfer from the CMP films to arenes.[8] Therefore, a lower LUMO energy level gives a higher detection sensitivity. In contrast, spin-coated TPBCz films, which are nonporous and do not have an extended π conjugation, exhibited a maximum quenching percentage of only 43 % after 120 s exposure under otherwise identical conditions (**Figure 9a**). These results indicate that the function of the CMP films is multifold: the extended π-conjugation network allows exciton migration, the porous skeleton provides a broad interface for electron transfer, and the micropores hold the arene molecules. These features cooperate to facilitate the signaling process and improve the response. The CMP films offer a practical platform for fabricating chemosensors, which feature a precisely controlled structure and a simple fabrication process together with excellent reproducibility and high performance.

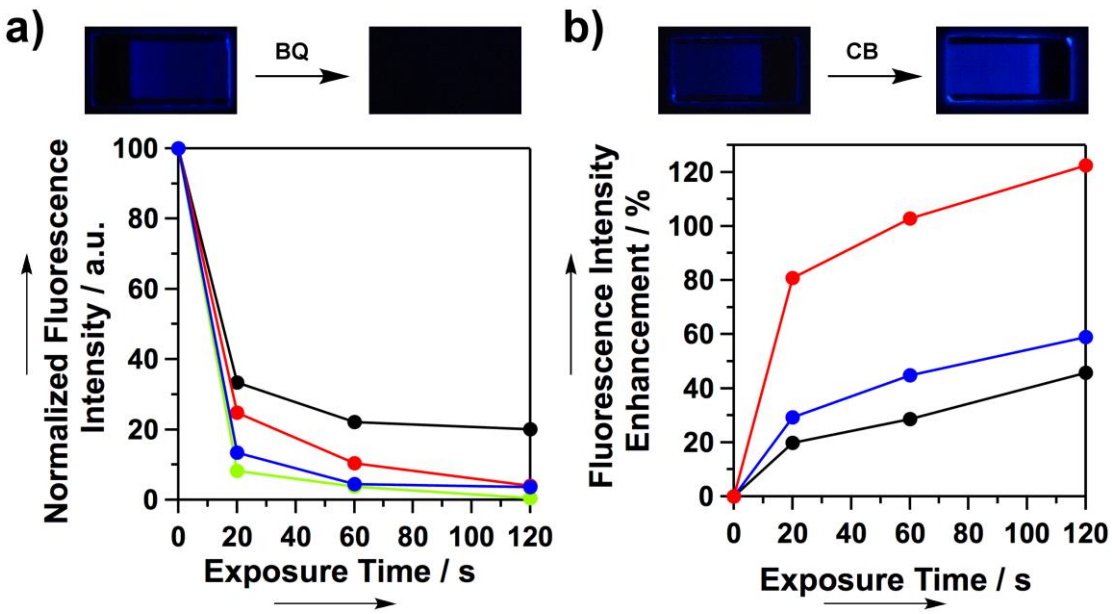

Figure 10. a) Normalized fluorescence intensity of the CMP films upon exposure to vapors of benzonitrile (BN, black line), 1,2-dinitrobenzene (DNB, red line), hexafluorobenzene (HFB, blue line), and 1,4-benzoquinone (BQ, green line) for different periods of time. Photos: fluorescence quenching by BQ vapor. b) Enhancement of fluorescence intensity of the CMP films upon exposure to vapors of toluene (black line), benzene (blue line), and cholorobenzene (CB, red line) for different periods of time. Photos: enhancement of fluorescence intensity upon exposure to CB vapor.

The CMP films are also sensitive to electron-rich arenes. In contrast to electron-deficient arenes that quench fluorescence, electron-rich arenes enhanced the fluorescence intensity of the CMP films, thus allowing fluorescence-on sensing (**Figure 11**). For example, upon exposure to toluene vapor for 20 s, the fluorescence intensity of the CMP films increased by 20 % (**Figure 10 b**, black line). As the exposure time was prolonged, further enhancement was observed, whereas the fluorescence intensity reached a 46 % increment upon 120 s exposure. Similarly, benzene vapor triggered a 59 % enhancement on 120 s exposure (**Figure 10 b**, red line). Remarkably, upon exposure to chlorobenzene (CB) vapor, the fluorescence intensity was increased by 81 % in 20 s, and by 122 % in 120 s (Figure 10 b, blue line and inset). In contrast, spin-coated TPBCz films exhibited a very limited change in fluorescence intensity with only 19 % enhancement for CB after 120 s exposure under otherwise identical conditions (Figure 10b). The flow of electrons of

arenes to the conduction band of TPBCz-CMP enhances the fluorescence intensity, as observed for bulk CMP solids.[3f]

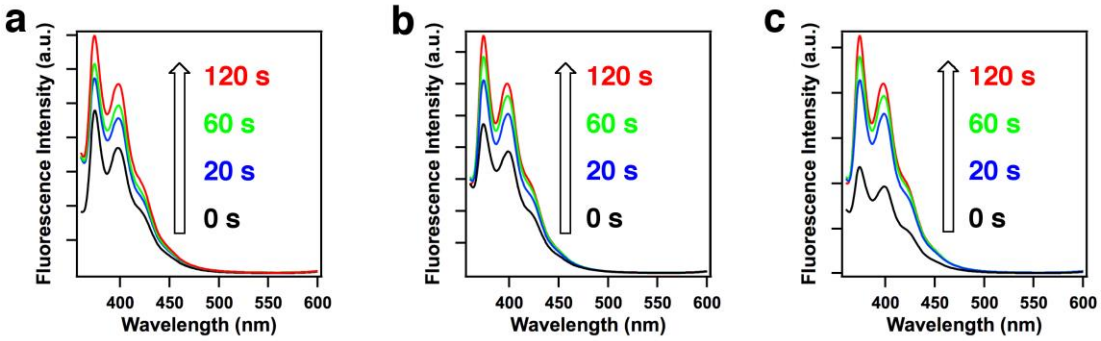

Figure 11. Fluorescence spectral changes of CMP films upon exposure to the vapors of (a) toluene, (b) benzene, and (c) CB, for different period of time.

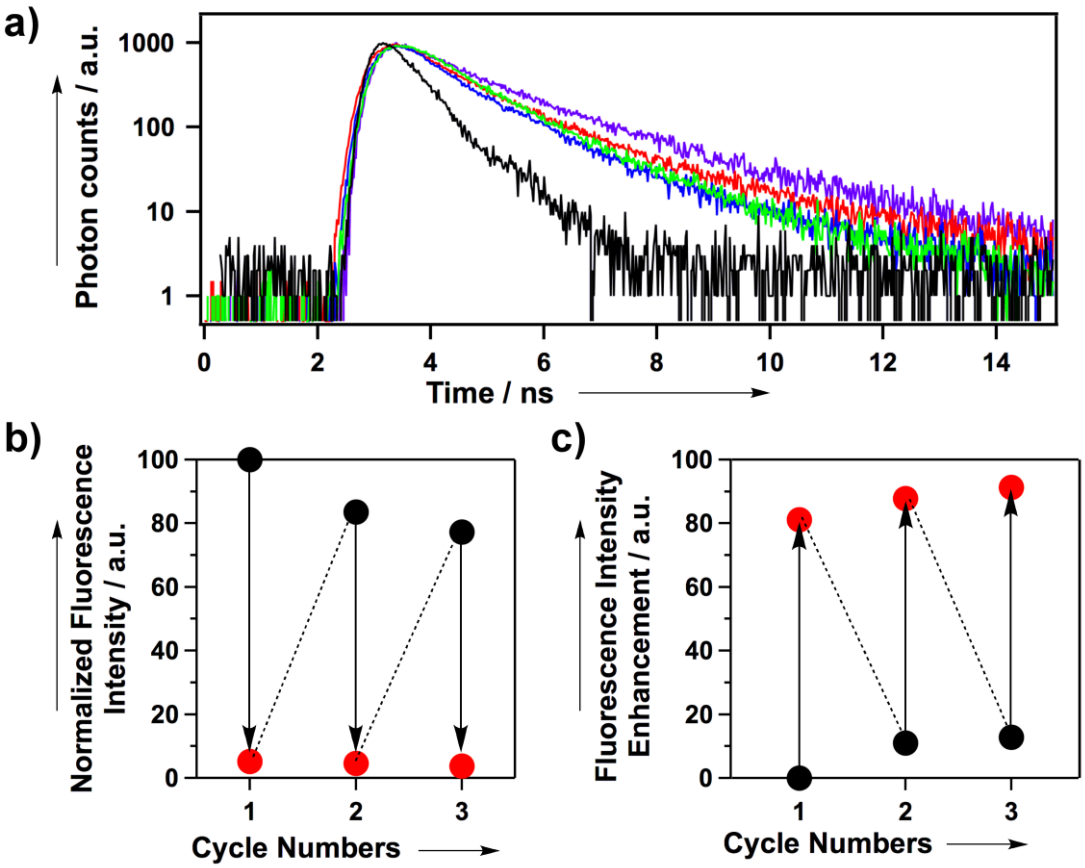

Figure 12. a) Fluorescence-decay profiles of the original CMP film (purple) and the films upon exposure to BQ (red curve), CB (blue curve), and Fe^{3+} (green curve). The black curve represents the IRF (instrument response function) profile. Cycling test of the CMP films upon 20 s exposure to vapors of b) BQ and c) CB.

Time-resolved fluorescence spectroscopy was utilized to investigate the kinetics of electron transfer. The CMP film exhibited a fluorescence lifetime (τ_0) of 3.25 ns, which was decreased to 1.03 and 1.86 ns (τ_{DA}) upon exposure to BQ or CB vapor for 20 s, respectively (**Figure 12 a**). The pseudo-first-order rate constant of electron transfer from the film to BQ or from CB to the film was estimated to be 6.63×10^8 or 2.30×108 s^{-1}, respectively, by using τ_{DA}-1-τ_0-1. On the other hand, the lifetime of spin-coated TPBCz film was decreased from 4.65 to 3.32 or 3.79 ns, on contact with BQ or CB vapor for 20 s (**Figure 13a**). The electron-transfer rate constants from the TPBCz film to BQ and from CB to the film were 8.62×10^7 and 4.88×10^7 s^{-1}, respectively. Therefore, the electron transfer of the CMP films is much faster than that of the monomer films.

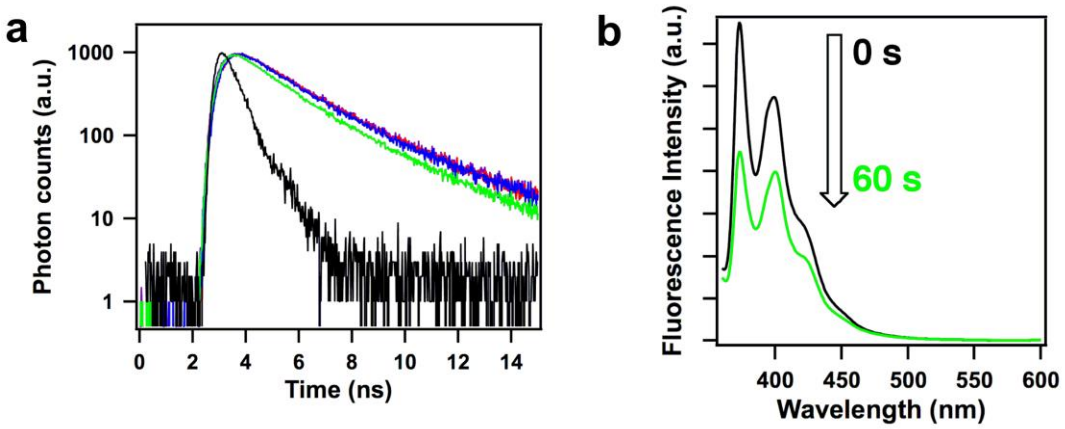

Figure 13. a) Fluorescence decay profiles of the spin-coated monomer film (black: IRF, purple: CMP film, red: exposure to BQ, blue: exposure to CB, green: exposure to Fe^{3+} solution); b) Fluorescence spectral changes of the spin-coated monomer film upon immersion in aqueous Fe^{3+} solution with concentrations of 10^{-5} M for 60 s.

The CMP films can be used repetitively. For example, upon exposure to BQ vapor for 20 s, the CMP film exhibited the same degree of fluorescence quenching after each cycle, and the fluorescence intensity recovered to a similar level when the BQ vapor was removed (**Figure 12b**). The CMP films exhibited a similar degree of the enhancement in fluorescence intensity upon repetitive exposure to CB vapor for 20 s in the cycling test (**Figure 12c**). Because of their highly

crosslinked network skeletons, the CMP films achieve outstanding stability and can be used repetitively, while retaining a high sensitivity and rapid response.

The carbazole groups in the CMP films can be oxidized chemically or electrochemically, providing a possibility for sensing redox-active ions. For instance, Fe^{3+}, an essential ion in biological systems, has a standard electrode potential of 0.77 V ($E_{Fe(III)/Fe(II)}$),[5a] which is higher than the oxidative potential of dimeric carbazoles (0.6 V) in the CMP films. I found that when the CMP films were immersed in an aqueous Fe^{3+} solution, the dimeric carbazoles in the CMP films were oxidized to form cations, which quenched the fluorescence of the CMP films. Based on this result, the CMP films were utilized to detect different concentrations of Fe^{3+} (**Figure 14**). As shown in **Figure 15 a**, when the CMP films were immersed for 20 s in aqueous solutions of Fe^{3+} in concentrations ranging from 10^{-3} to 10^{-5} m, the degree of fluorescence quenching exceeded 90 %. Remarkably, as the concentration of Fe^{3+} decreased to 10^{-6} and 10^{-7} m, over 80 % of the fluorescence was quenched. Even when

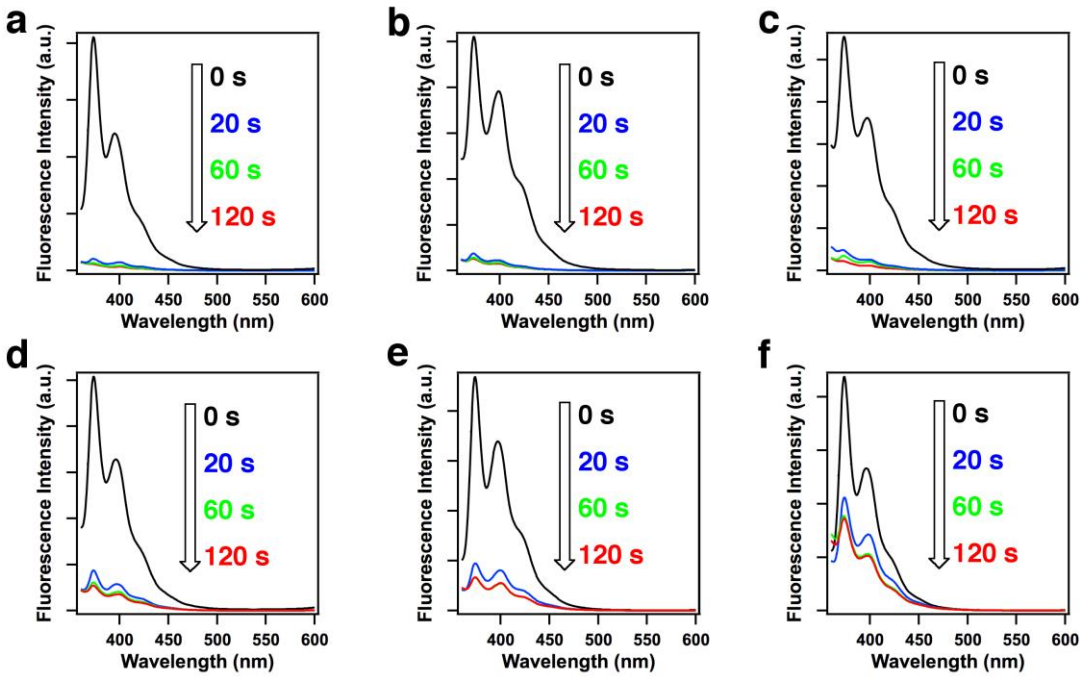

Figure 14. Fluorescence spectral changes of the CMP films upon immersion in aqueous Fe^{3+} solutions with different concentrations of (a) 10^{-3} M, (b) 10^{-4} M, (c) 10^{-5} M, (d) 10^{-6} M, (e) 10^{-7} M, and (f) 10^{-8} M, respectively.

the Fe^{3+} concentration was decreased to 10^{-8} m, the degree of fluorescence quenching was as high as 50 %. The CMP films with such a high sensitivity for reporting Fe^{3+} outperform other Fe^{3+} chemosensors thus far reported.[9] In contrast, the spin-coated TPBCz films exhibited a low sensitivity for Fe^{3+} by showing a degree of fluorescence quenching of only 41 % when immersed in a 10^{-5} m solution for 60 s (**Figure 13b**). The rate constant of electron transfer from the CMP film to Fe^{3+} was 5.85×10^{8} s^{-1} (**Figure 12 a**).

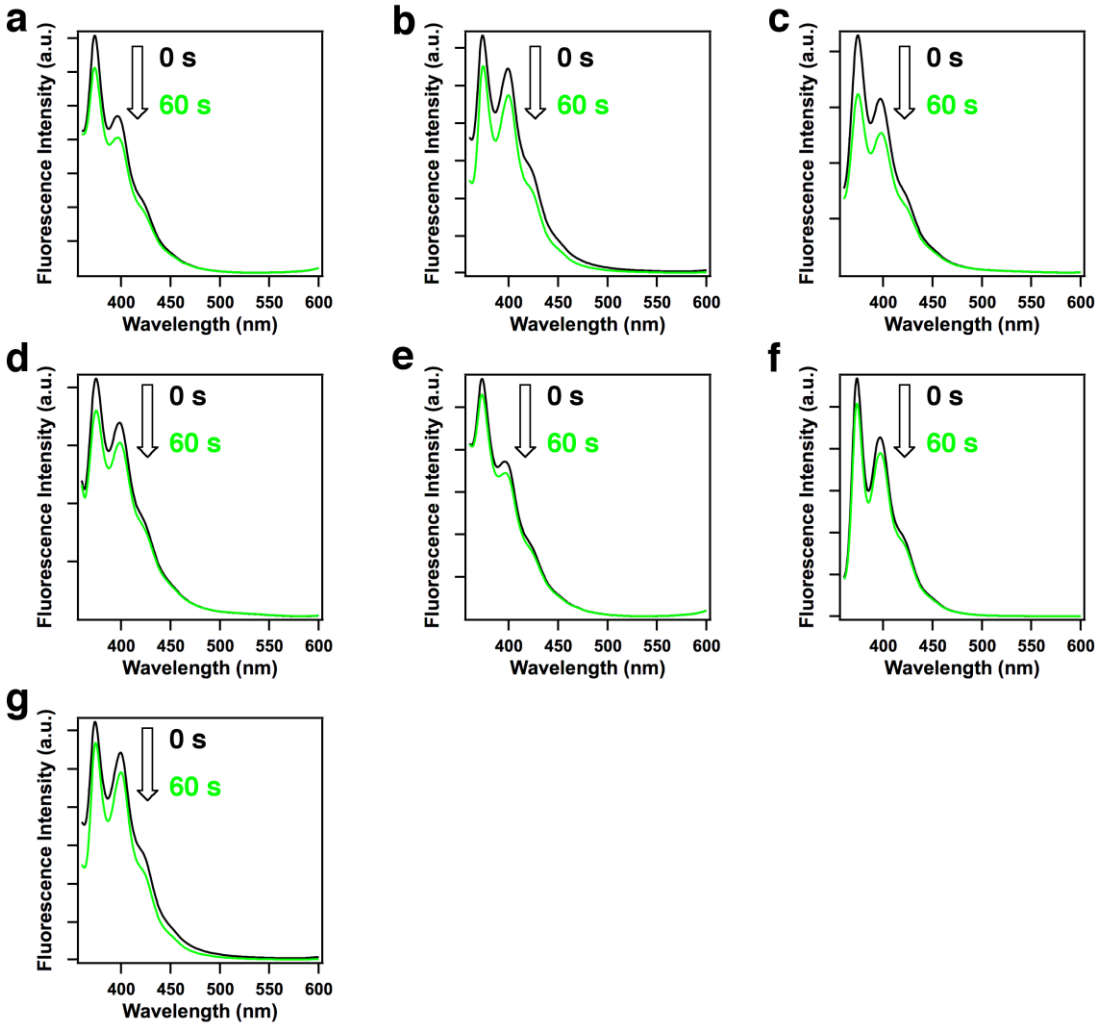

Figure 15. Fluorescence spectral changes of the CMP films upon immersion for 60 s in aqueous solutions of (a) Ni^{2+}, (b) Co^{2+}, (c) Cu^{2+}, (d) Fe^{2+}, (e) K^{+}, (f) Ca^{2+}, and (g) Mg^{2+} at a concentration of 10^{-4} M.

I further investigated the scope of ion species that can be sensed (**Figure 15**). Compared to Fe^{3+} ions, the CMP films exhibited low sensitivity and torpid response to other non-oxidative metal ions (**Figure 16 b**). For example, the fluorescence was slightly quenched with a degree of

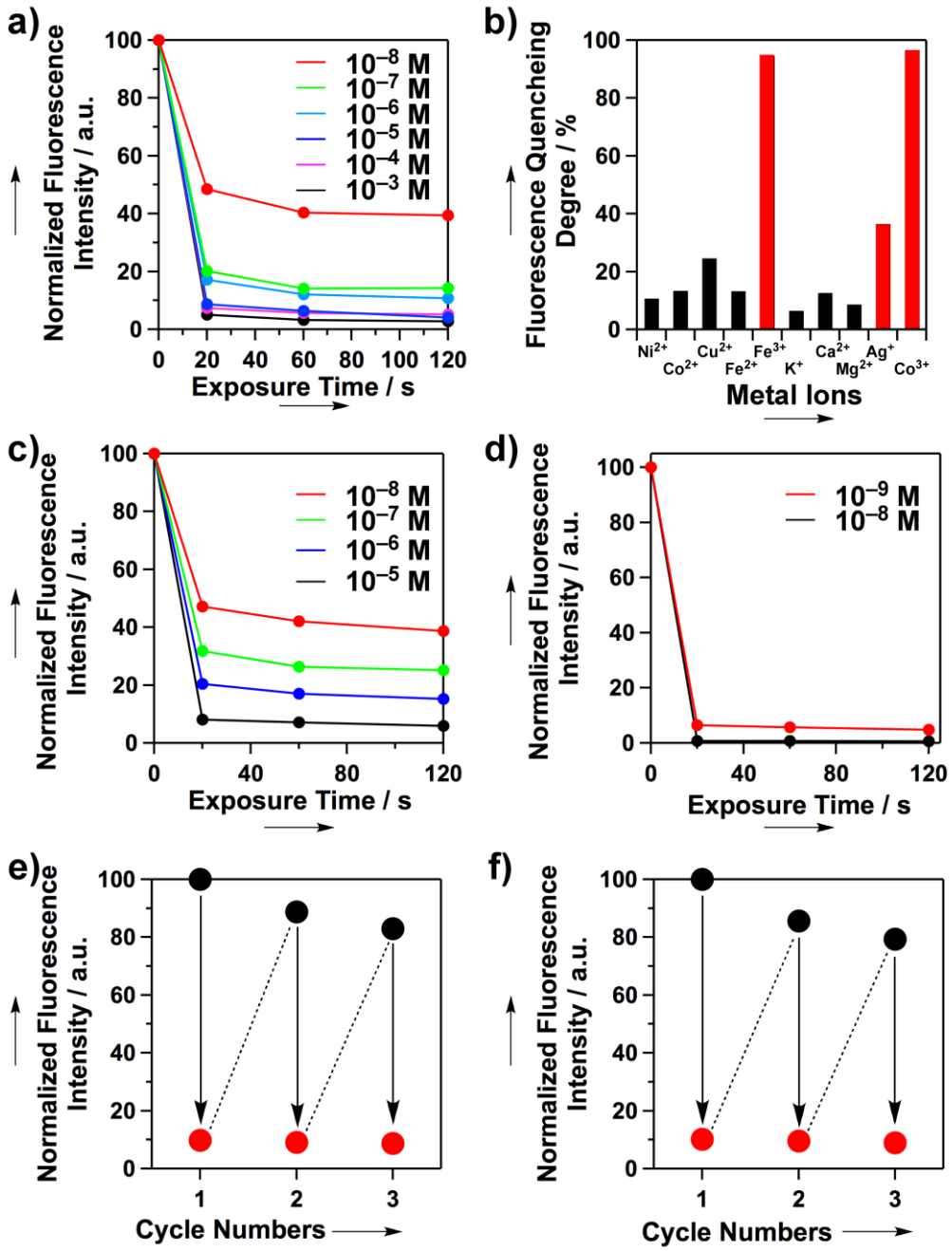

Figure 16. a) Normalized fluorescence intensity of the CMP films upon immersion in aqueous solutions of Fe^{3+} at different concentrations (10^{-3} to 10^{-8} M) for different periods of time. b) Degree of fluorescence quenching of the CMP films upon 60 s immersion in aqueous solutions of different metal ions (10^{-4} M). Red bars are for Fe^{3+}, Ag^{+}, and Co^{3+}. Normalized fluorescence intensity of the CMP films upon immersion in saline solutions of c) dopamine and d) HOCl at different concentrations for different periods of time. Recycle test of the CMP films for biosensing saline solutions (10^{-8} M) of e) dopamine and f) HOCl.

only 17 % when immersed for 60 s in an aqueous solution of Fe^{2+} with a concentration of 10^{-4} m. Similarly, the CMP films are not sensitive to other transition metals, such as Co^{2+}, Cu^{2+}, and Ni^{2+}. As for alkali metal ions, I examined K^{+}, Ca^{2+}, and Mg^{2+}, which could not effectively quench the fluorescence of the CMP films.

To investigate whether the CMP films are sensitive to other oxidative metal ions, I conducted sensing experiments with Ag^{+} and Co^{3+}, which are known as oxidative metal species. The CMP films exhibited a significant fluorescence quenching when exposed to an aqueous solution of Ag^{+} (10^{-4} m) for only 60 s (**Figure 15 h**). A more sensitive quenching was observed with Co^{3+}; the fluorescence of the films was quenched almost completely (**Figure 15i**). The degree of fluorescence quenching was 36 % and 96 % for Ag^{+} and Co^{3+}, respectively (**Figure 16 b**). These results clearly demonstrate that the CMP films are responsive to oxidative metal ions, such as Fe^{3+}, Co^{3+}, and Ag^{+} (**Figure 16b**).

The reported chemosensors for the detection of metal ions usually utilize probe molecules that coordinate with metal ions to cause spectral change.[10] However, such methods suffer from the interference of other transition-metal ions,[10] such as Ni^{2+}, Co^{2+}, Cu^{2+}, and Fe^{2+}. To show the difference, I further examined the chemosensing of a mixture of Fe^{3+} and Co^{2+} (each 10^{-7} m) using the CMP film (**Figure 17**), which exhibited a high degree of fluorescence quenching, as observed for a solution of Fe^{3+}. Even in the case of a physiological saline solution containing Fe^{3+} (10^{-7} m), the CMP film displayed a high sensitivity and quick response (**Figure 18**). Because of less interference, the CMP films are promising for real-time biosensing of oxidative ion species.[11] The CMP films were recyclable for Fe^{3+} sensing (**Figure 19**) by immersion into a solution of

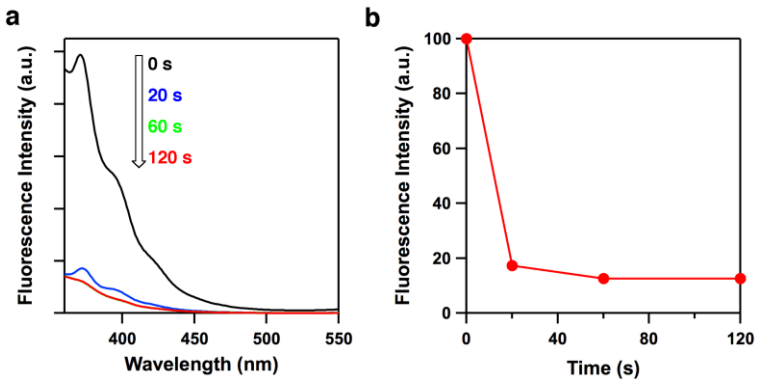

Figure 17. (a) Fluorescence spectral changes and (b) normalized fluorescence intensity of the CMP film upon immersion in an aqueous solution of Fe^{3+} and Co^{2+} (10^{-7} M).

$NaBH_4$, which can reduce the dimeric carbazyl cations to their neutral states and recover the fluorescence.

Dopamine (DA, 3,4-dihydroxyphenethylamine) is an important neurotransmitter,[12, 13] and malfunction of DA-responsive neurons has been implicated in a number of diseases, including Parkinson's disease. This has sparked significant interest for the development of detection methods for DA. However, the low sensitivity and complexity of various analytical methods, such as electrochemical techniques and HPLC, make it a great challenge to provide technically simple and label-free DA detection. I found that the electron-donating CMP films serve as a new type of sensors, featuring high sensitivity and label-free detection of DA as a result of high-rate electron transfer (**Figure 20**). When the CMP films were immersed in the saline solutions of DA with a concentration of 10^{-5} and 10^{-6} m for only 20 s, the fluorescence was quenched by 90 % and 80 %, respectively (**Figure 16c**, black and blue dots). The DA concentration could be decreased to 10^{-8} m (red dot), upon which the fluorescence of the film was quenched to 50 % after only 20 s exposure. This high sensitivity makes the CMP films superior to other DA sensors thus far reported. The fluorescence decay profiles revealed that the rate constant of the electron transfer from the CMP film to DA is as high as $3.8 \times 108\ s^{-1}$ (**Figure 21**).

Hypochlorous acid (HOCl) is a highly active antibacterial agent and a key compound involved in biological defence.[14] Because the dimeric carbazole units can be oxidized by HOCl, the CMP films can serve as an outstanding sensor for HOCl (**Figure 22**). When the CMP films were immersed in the saline solutions of HOCl with a concentration of 10^{-8} m for only 20 s, the fluorescence of the films was completely quenched (**Figure 16d**, black dots). Remarkably, even when the HOCl concentration was decreased to as low as 10^{-9} m, the quenching degree still exceeded 90 % (red dots). The exceptionally sensitive fluorescence quenching is beyond the photon-counting instrument for a fluorescence decay measurement. The CMP films are recyclable for biosensing DA and HOCl. By rinsing with a $NaBH_4$ solution and deionized water, the films recovered the fluorescence and were reused for sensing (**Figure 16 e, f**).

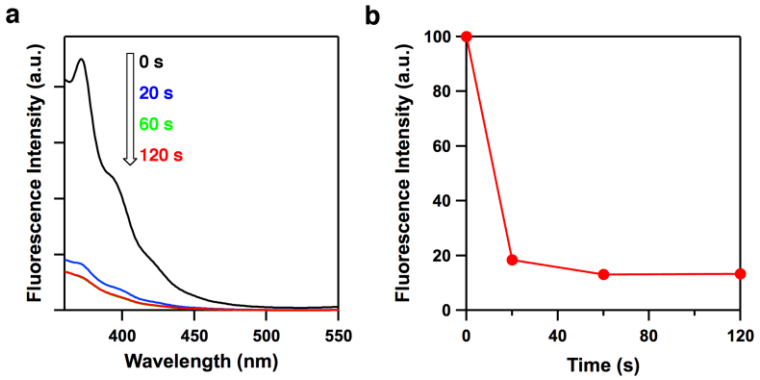

Figure 18. (a) Fluorescence spectral changes and (b) normalized fluorescence intensity of the CMP film upon immersion in physiological saline solution containing Fe^{3+} (10^{-7} M).

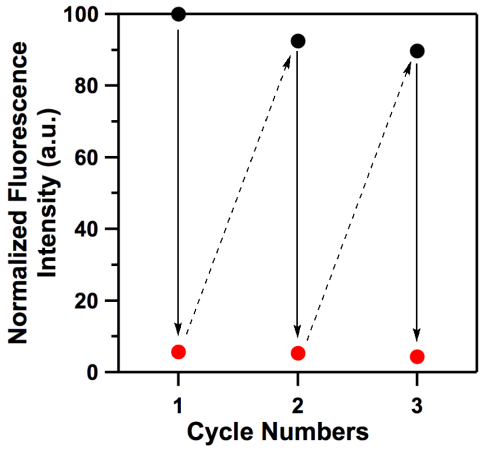

Figure 19. Cycling test of the CMP films for Fe(III) solution (10^{-6} M) upon 20-s immersion, followed by washing with $NaBH_4$ solution and deionized water.

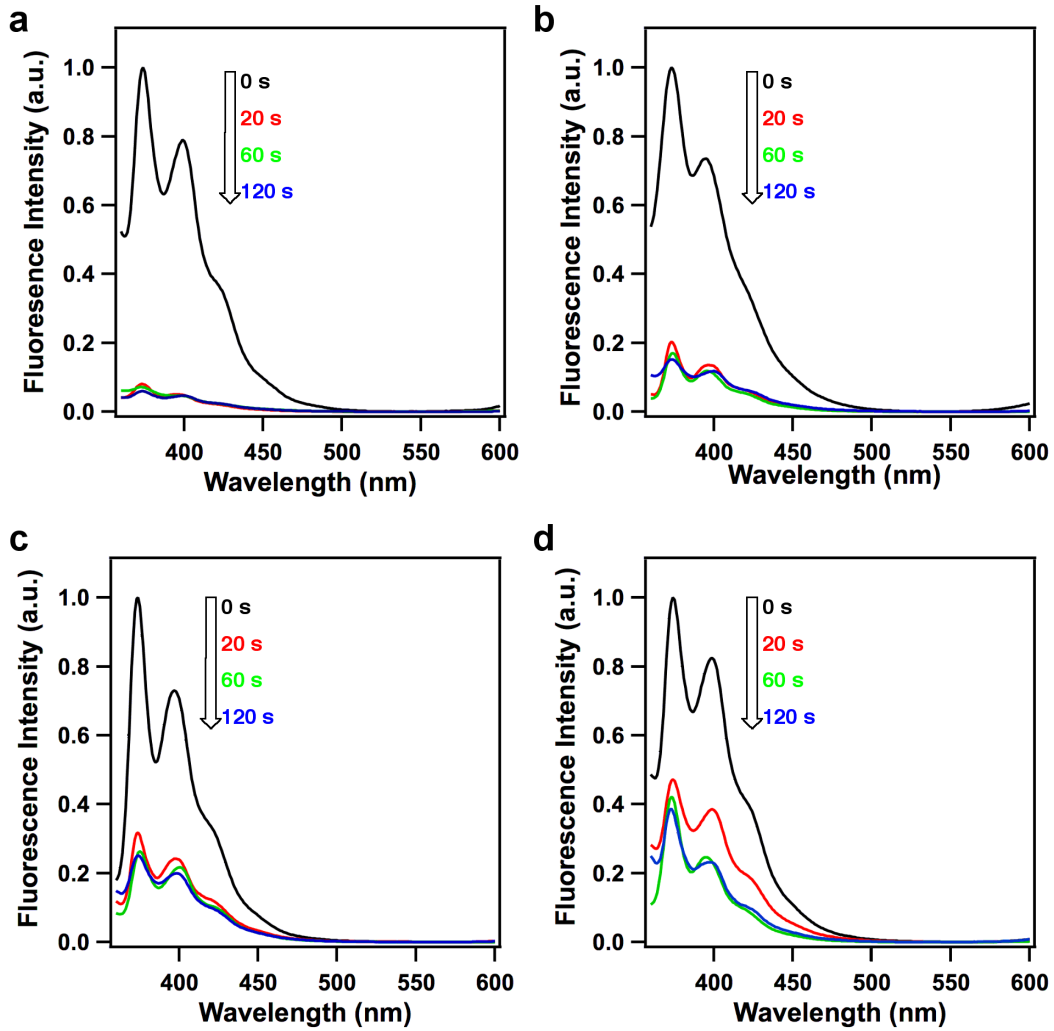

Figure 20. Fluorescence spectral changes of the CMP films upon immersion in the saline solutions of dopamine at (a) 10^{-5} M, (b) 10^{-6} M, (c) 10^{-7} M, and (d) 10^{-8} M.

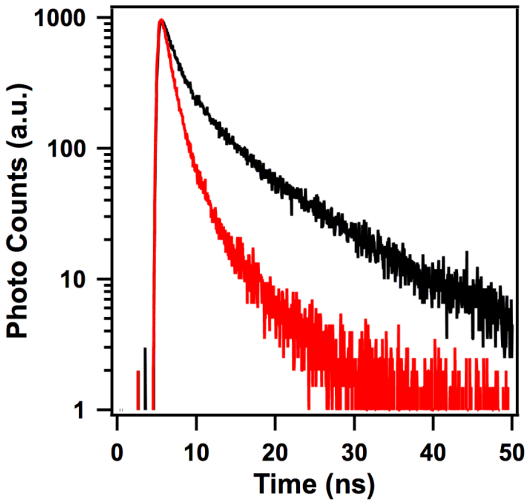

Figure 21. Fluorescence decay profiles of the CMP films (black: the CMP film, red: exposure to dopamine (10^{-7} M, 20 s)).

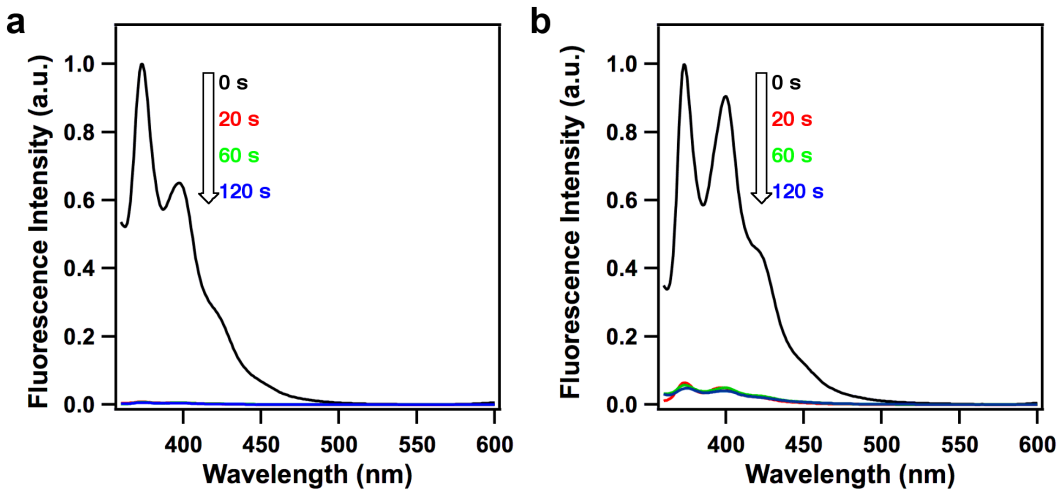

Figure 22. (a) Fluorescence spectral of the CMP films upon immersion in the saline solutions of HOCl at (a) 10^{-8} M) and (b) 10^{-9} M.

Conclusion

In summary, I have developed an electrochemical approach for the controlled synthesis of thin films of conjugated microporous polymers. The thickness of the CMP films can be synthetically controlled, and the films can be obtained on substrates or as freestanding films. The films are unique in that they are porous, possess extended π conjugation, allow exciton delocalization over the skeletons, and enable high-rate electron transfer. Because of these features, I developed the CMP films as versatile platforms for chemo- and biosensing. The CMP sensors feature excellent selectivity, rapid response, and high sensitivity, discriminate electron-rich and electron-poor arenes through fluorescence on/off sensing, and selectively detect oxidative ions by redox-induced fluorescence quenching. The films function as label-free sensors for the highly sensitive detection of biologically important dopamine and HOCl species. Given the structural diversity and flexibility of CMPs, I anticipate the emergence of an exciting field in designing CMP films, which would significantly expand the potential of CMPs for applications.

Experimental Sections

Materials and Methods Tetrahydrofuran (THF, 99.0%), hexane, acetic ester, and diethyl ether were purchased from Kanto Chemicals. Toluene, triisopropyl borate, ammonia water, concentrated HCl, $LiClO_4$, and *n*-butyllithium (1.6 M) were purchased from Wako Chemicals. Copper(I) iodide, 18-crown-6 , potassium carbonate, anhydrous magnesium sulfate, 1,3-dimethyl-3,4,5,6-tetrahydro-2(1H)-pyrimidinone, and *p*-dibromobenzene were purchased from TCI. Tetrakis(triphenylphosphine) palladium(0) and carbazole were purchased from Aldrich. All chromatographic separations were carried out on silica gel (300 mesh).

^{1}H NMR spectra were recorded on JEOL models JNM-LA400 NMR spectrometers, where chemical shifts (δ in ppm) were determined with a residual proton of the solvent as standard. Fourier transform Infrared (FT-IR) spectra were recorded on a JASCO model FT-IR-6100 infrared spectrometer. UV-Vis-IR diffuse reflectance spectrum (Kubelka-Munk spectrum) was recorded on a JASCO model V-670 spectrometer equipped with integration sphere model IJN-727. Matrix-assisted laser desorption ionization time-of-flight mass (MALDI-TOF MS) spectra were recorded on an Applied Biosystems BioSpectrometry model Voyager-DE-STR spectrometer in reflector or linear mode. Field-emission scanning electron microscopy (FE-SEM) was performed on a JEOL model JSM-6700 operating at an accelerating voltage of 5.0 kV. The sample was prepared by drop-casting an acetone suspension onto mica substrate and then coated with gold. High-resolution transmission electron microscopy (HR-TEM) images were obtained on a JEOL model JEM-3200. Photoluminescence spectrum was recorded on a JASCO model FP-6600 spectrofluorometer. The absolute quantum yield was determined by standard procedure with an integral sphere JASCO model ILF-533 mounted on the FP-6600 spectrofluorometer. The film thickness was measured on an Veeco Dektak 150 profilometer. Time-resolved fluorescence spectroscopy was recorded on Hamamatsu compact fluorescence lifetime spectrometer Quantaurus–Tau model C11367-11. Kr sorption isotherm measurements of the CMP films were performed by using micromeritics$^@$ model 3Flex at 77 k.

Electropolymerization and Film preparations. The electropolymerization was performed using a standard one compartment, three-electrode electrochemical cell attached to an ALS/CHi 610C Electrochemical Workstation. The Ag/Ag^+ nonaqueous electrode was used as reference electrode.

ITO was used as the working electrode, and titanium metal was used as the counter electrode. A mixture of TPBCz (1 mg mL^{-1}) and $LiClO_4$ (0.1 M) in acetonitrile/H_2O (3/2 by vol) was used as electrolyte solution. The electropolymerization potential range was set between –0.8 V and 0.7 V, and the scan rate was 50 mV s^{-1}. After the electropolymerization process, the resulting films were washed with acetonitrile to remove unreacted precursors and supporting electrolytes, and dried in vacuum.

Bulk CMP samples. A bulk CMP sample was synthesized by the oxidation polymerization of TPBCz using $(NH_4)_2S_2O_8$ oxidant in CH_3CN for 72 h. The resulted powder was collected by filtration and washed exhaustively with CH_3OH. The powder was dried under vacuum at 120 ℃ overnight to give a black-colored solid in 75% yield.

Arene sensings. For the liquid arenes, 1 mL of arene was placed in an open glass vial (10 mL) that was placed in a capped glass vial (50 mL) for a week to ensure that the equilibrated vapor pressure of arenes was reached. For solid arene, 100 mg was utilized and set in the same set-up for liquid arenes. The CMP films were put into the 50 mL vial for a designated period for exposure to the vapors and were taken out and without any delay mounted to the sample holder of the fluorescence spectrophotometer and the emission spectrum was recorded. The original emission spectra of the CMP films were collected before placing the CMP films into the bottles containing the arenes. For the cycle test, the CMP films were exposed to arene vapors, measured with fluorescence spectrophotometer, vacuumed at 25 ℃ for 4 h to remove the absorbed arenes, left in air under dark for half an hour, and then were utilized in the next around detection.

Metal ion sensings. CMP films were put into quartz cuvette containing aqueous solution certain concentration of metal ions. The original emission spectra of the CMP films were collected by putting into quartz cuvette containing deionized water. $FeCl_3$, $FeSO_4$, $NiSO_4$, $CoSO_4$, $CuSO_4$, KCl, $CaCl_2$, and $MgCl_2$ were utilized as the source of metal ions.

Biosensings of dopamine and HOCl. The CMP films were put into quartz cuvette containing saline solutions with certain concentrations of dopamine and HOCl. The original emission spectra of the CMP films were collected by putting into quartz cuvette containing saline solution.

Recycle test. After sensing, the resulting CMP films were repeatitively rinsed with $NaBH_4$ solution and deionized water, dried under vacuum, and reused in the next-round sensing test.

Synthetic Procedures

Synthesis of TPBCz monomer.

9-(4-Bromophenyl)carbazole was synthesized from dibromobenzene using a literature procedure.[15] 4-Carbazolyl-1-bromophenylboronic was prepared according to a reported method.[16] 1,3,5-tris[4-(*N*-carbazolyl)phenyl] benzene was obtained as indicated by ^{1}H NMR by comparison with that described previously.[17]

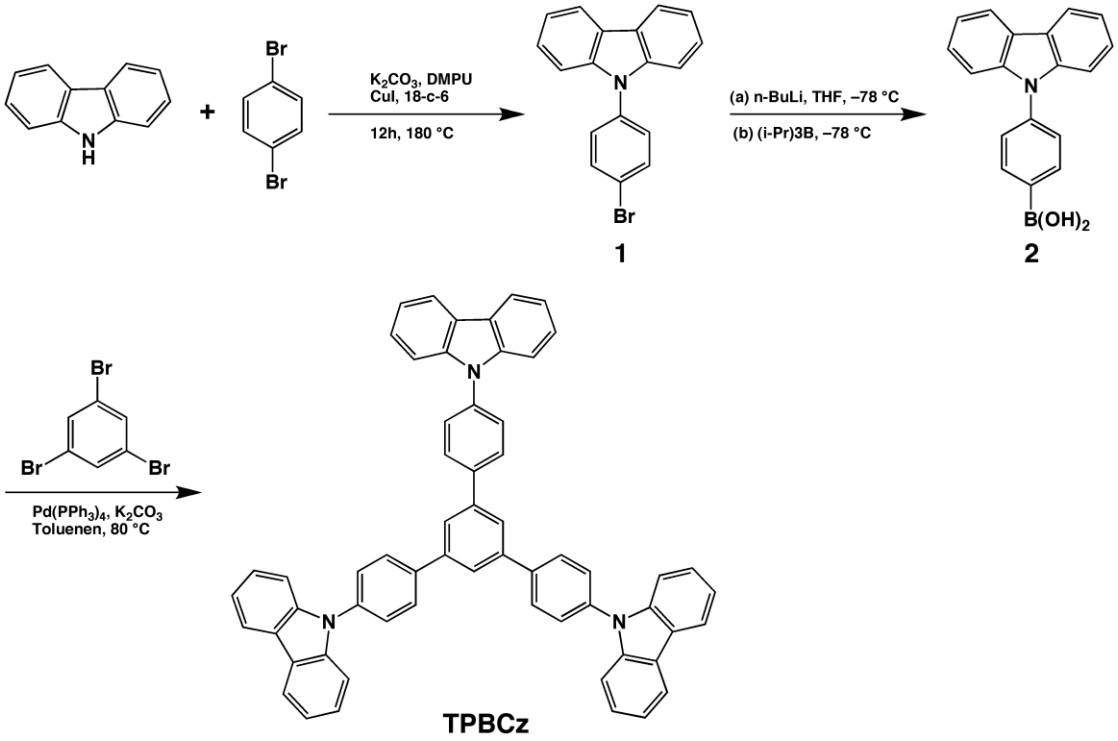

Synthesis of 9-(4-bromophenyl)carbazole (1).

A mixture of CuI (1.14 g, 6 mmol), 18-crown-6 (0.53 g, 2 mmol), K_2CO_3 (16.6 g, 120 mmol), 1,3-dimethyl-3,4,5,6-tetrahydro-2(1H)-pyrimidinone (DMPU) (20 mL), *p*-dibromobenzene (14.2 g, 60 mmol), and carbazole (10 g, 60 mmol) was heated at 170 ℃ for 11 h under argon. After cooling to room temperature, the mixture was quenched with 2 M HCl, and the precipitate was collected and washed with ammonia solution, and deionized water. The grey solid was purified with column chromatography using hexane as an eluent to give a white product (11.7 g). Yield: 74%. mp: 145–146℃. ^{1}H NMR (400 MHz, $CDCl_3$): δ (ppm) = 8.13 (d, 2 H, J = 7.6 Hz), 7.72 (d, 2 H, J = 8.8 Hz), 7.45 (d, 2 H, J = 8.8 Hz), 7.41–7.37 (dt, 4H, J_1 = 6.8 Hz, J_2 = 6.8 Hz), 7.30 (t, 2H, J = 6.6 Hz).

Synthesis of 4-carbazolyl-1-bromophenylboronic acid (2).

n-Buthyl lithium in hexane (1.6 M, 11.5 mL, 18 mmol) was added dropwise to a solution of (**1**) (4.3 g, 15 mmol) in THF (40 mL) at –78 ℃ with stirring. After reaction for 1h, triisopropyl borate (32 mL, 18 mmol) was added using a syringe. The mixture was stirred for additional 1 h and then was gradually heated to room temperature and stirred overnight. The clear solution was diluted with ether (100 mL) and washed with deionized water. The organic layer was dried over anhydrous $MgSO_4$. After filtration, the solution was concentrated using a rotary evaporator. Flash column chromatography of the residue over silica gel with a mixed solvent of hexane and ethyl acetate (9/1) as a gradient eluent afforded 3.3 g white solid with a yield of 87%. ^{1}H NMR (400 MHz, $CDCl_3$): δ (ppm) = 8.56 (d, 2H, J = 8.0 Hz), 8.18 (d, 2H, J = 7.6 Hz), 7.80 (d, 2H, J = 8.0 Hz), 7.56 (d, 2H, J = 8.0 Hz), 7.46 (t, 2H, J = 7.2 Hz), 7.33 (t, 2H, J = 7.6 Hz).

Synthesis of 1,3,5-tris[4-(N-carbazolyl)phenyl] benzene (TPBCz).

Tetrakis(triphenylphosphine)palladium (0.042 g, 0.09 mmol), (2) (0.517 g, 1.8 mmol), and (3) (0.187 g, 0.6 mmol) were added to an air-free two-phase mixture of toluene (15 mL) and 2M K_2CO_3 aqueous solution (12 mL). The resultant system was vigorously stirred under an argon atmosphere at 80 ℃ for 24 h. The organic layer was separated and the aqueous phase was extracted with diethyl ether. The organic phases were combined and washed with brine and dried over anhydrous $MgSO_4$. The solvent was evaporated and the residue went through silica-gel column with EtOAc–hexane (1/9 by vol, R_f = 0.65) as an eluent to afford yellowish solid with a yield of 83%. ^{1}H NMR ($CDCl_3$, 400 MHz) δ (ppm) 8.19 (d, J = 8.52 Hz, 4H), 8.05 (s, 3H), 8.03 (d, J = 8.52 Hz, 3H), 7.75 (d, J = 8.04 Hz, 4H), 7.54 (d, J = 8.52 Hz, 4H), 7.46 (t, J = 7.04 Hz, 4H), 7.39 (t, J = 7.04 Hz, 4H), 7.33 (t, J = 7.04 Hz, 4H), 7.21 (d, J = 8.52 Hz, 3H), 7.14 (d, J = 8.52 Hz, 3H), 7.09 (d, J = 8.52 Hz, 3H). MALDI-TOF MS (calcd for $C_{60}H_{39}N_3$: 801.31), found m/z = 802.44 $(M + H)^+$.

References

1. a) J. X. Jiang, F. Su, A. Trewin, C. D. Wood, N. L. Campbell, H. Niu, C. Dickinson, A. Y. Ganin, M. J. Rosseinsky, Y. Z. Khimyak, A. I. Cooper, *Angew. Chem.* **2007**, *119*, 8728-8732; *Angew. Chem. Int. Ed.* **2007**, *46*, 8574-8578; b) J. X. Jiang, F. Su, A. Trewin, C. D. Wood, H. Niu, J. T. A. Jones, Y. Z. Khimyak, A. I. Cooper, *J. Am. Chem. Soc.* **2008**, *130*, 7710-7720; c) A. I. Cooper, *Adv. Mater.* **2009**, *21*, 1291-1295; d) J. T. A. Jones, D. Holden, T. Mitra, T. Hasell, D. J. Adams, K. E. Jelfs, A. Trewin, D. J. Willock, G. M. Day, J. Bacsa, A. Steiner, A. I. Cooper, *Angew. Chem.* **2011**, *123*, 775-779; *Angew. Chem. Int. Ed.* **2011**, *50*, 749-753; e) J. X. Jiang, C. Wang, A. Laybourn, T. Hasell, R. Clowes, Y. Z. Khimyak, J. L. Xiao, S. J. Higgins, D. J. Adams, A. I. Cooper, *Angew. Chem.* **2011**, *123*, 1104-1107; *Angew. Chem. Int. Ed.* **2011**, *50*, 1072-1075.
2. a) A. Thomas, P. Kuhn, J. Weber, M. M. Titirici, M. Antonietti, *Macromol. Rapid Commun.* **2009**, *30*, 221-236; b) M. J. Bojdys, S. A. Wohlgemuth, A. Thomas, M. Antonietti, *Macromolecules* **2010**, *43*, 6639-6645.
3. a) L. Chen, Y. Yang, D. Jiang, *J. Am. Chem. Soc.* **2010**, *132*, 9138-9143; b) L. Chen, Y. Honsho, S. Seki, D. Jiang, *J. Am. Chem. Soc.* **2010**, *132*, 6742-6748; c) L. Chen, Y. Yang, Z. Guo, D. Jiang, *Adv. Mater.* **2011**, *23*, 3149-3154; d) Y. Kou, Y. Xu, Z. Guo, D. Jiang, *Angew. Chem.* **2011**, *123*, 8912-8916; *Angew. Chem. Int. Ed.* **2011**, *50*, 8753-8757; e) Y. Xu, L. Chen, Z. Guo, A. Nagai, D. Jiang, *J. Am. Chem. Soc.* **2011**, *133*, 17622-17625; f) X. Liu, Y. Xu, D. Jiang, *J. Am. Chem. Soc.* **2012**, *134*, 8738-8741; g) Y. Xu, S. Jin, H. Xu, A. Nagai, D. Jiang, *Chem. Soc. Rev.* **2013**, *42*, 8012-8031; h) Y. Xu, A. Nagai, D. Jiang, *Chem. Commun.* **2013**, *49*, 1591- 1593; i) X. Liu, Y. Xu, Z. Guo, A. Nagai, D. Jiang, *Chem. Commun.* **2013**, *49*, 3233-3235; j) Y. Xu, D. Jiang, *Chem. Commun.* **2014**, *50*, 2781-2783; k) F. Xu, X. Chen, Z. Tang, D. Wu, R. Fu, D. Jiang, *Chem. Commun.* **2014**, *50*, DOI: 10.1039/C4CC01002G.
4. a) S.-Y. Moon, J.-S. Bae, E. Jeon, J.-W. Park, *Angew. Chem.* **2010**, *122*, 9694-9698; *Angew. Chem. Int. Ed.* **2010**, *49*, 9504 -9508; b) M. Kim, M. Byeon, J.-S. Bae, S.-Y. Moon, G. Yu, K. Shin, F. Basarir, T.-H. Yoon, J.-W. Park, *Macromolecules* **2011**, *44*, 7092-7095; c) V. Senkovskyy, I. Senkovska, A. Kiriy, *ACS Macro Lett.* **2012**, *1*, 494-498; d) G. Cheng, T. Hasell, A. Trewin, D. J. Adams, A. I. Cooper, *Angew. Chem.* **2012**, *124*, 12899-12903; *Angew. Chem.*

Int. Ed. **2012**, *51*, 12727- 12731; e) K. V. Rao, S. Mohapatra, T. K. Maji, S. J. George, *Chem. Eur. J.* **2012**, *18*, 4505-4509; f) X. Zhu, C. Tian, S. M. Mahurin, S.-H. Chai, C. Wang, S. Brown, G. M. Veith, H. Luo, H. Liu, S. Dai, *J. Am. Chem. Soc.* **2012**, *134*, 10478-10484; g) X. Zhu, C. Tian, S. Chai, K. Nelson, K. S. Han, E. W. Hagaman, G. M. Veith, S. M. Mahurin, H. Liu, S. Dai, *Adv. Mater.* **2013**, *25*, 4152-4158.

5. a) A. J. Bard, L. Faulkner, Electrochemical Methods-Fundamentals and Applications, *2nd ed.*, Wiley, New York, **2001**; b) J. Heinze, B. Frontana, S. Ludwigs, *Chem. Rev.* **2010**, *110*, 4724 -4771; c) P. M. Beaujuge, J. R. Reynolds, *Chem. Rev.* **2010**, *110*, 268-320; d) C. Gu, T. Fei, Y. Lv, T. Feng, S. Xue, D. Lu, Y. Ma, *Adv. Mater.* **2010**, *22*, 2702-2705; e) C. Gu, T. Fei, L. Yao, Y. Lv, D. Lu, Y. Ma, *Adv. Mater.* **2011**, *23*, 527-530; f) C. Gu, W. Dong, L. Yao, Y. Lv, Z. Zhang, D. Lu, Y. Ma, *Adv. Mater.* **2012**, *24*, 2413-2417; g) C. Gu, Z. Zhang, S. Sun, Y. Pan, C. Zhong, Y. Lv, M. Li, K. Ariga, F. Huang, Y. Ma, *Adv. Mater.* **2012**, *24*, 5727-5731; h) C. Gu, Y. Chen, Z. Zhang, S. Xue, S. Sun, K. Zhang, C. Zhong, H. Zhang, Y. Pan, Y. Lv, Y. Yang, F. Li, S. Zhang, F. Huang, Y. Ma, *Adv. Mater.* **2013**, *25*, 3443-3448.
6. a) F. Piron, P. Leriche, I. Grosu, J. Roncali, *J. Mater. Chem.* **2010**, *20*, 10260-10268; b) Y. Yuan, F. Sun, H. Ren, X. Jing, W. Wang, H. Ma, H. Zhao, G. Zhu, *J. Mater. Chem.* **2011**, *21*, 13498-13502.
7. a) A. Desbene-Monvernay, P.-C. Lacaze, J.-E. Dubois, *J. Electroanal. Chem.* **1981**, *129*, 229-241; b) A. Desbene-Monvernay, P.-C. Lacaze, M. Delamar, *J. Electroanal. Chem.* **1992**, *334*, 241-246.
8. S. Pramanik, C. Zheng, X. Zhang, T. J. Emge, J. Li, *J. Am. Chem. Soc.* **2011**, *133*, 4153-4155.
9. a) X. Wang, C. Drew, S.-H. Lee, K. J. Senecal, J. Kumar, L. A. Samuelson, *Nano Lett.* **2002**, *2*, 1273-1275; b) S. J. Lee, J.-E. Lee, J. Seo, I. Y. Jeong, S. S. Lee, J. H. Jung, *Adv. Funct. Mater.* **2007**, *17*, 3441-3446; c) M. Shellaiah, Y.-H. Wu, A. Singh, M. V. R. Raju, H.-C. Lin, *J. Mater. Chem.* A **2013**, *1*, 1310-1318.
10. a) Y. Xiang, A. Tong, *Org. Lett.* **2006**, *8*, 1549-1552; b) J. Du, M. Hu, J. Fan, X. Peng, *Chem. Soc. Rev.* **2012**, *41*, 4511-4535.
11. a) S. E. Webber, *Chem. Rev.* **1990**, *90*, 1469-1482; b) A. W. Czarnik in Fluorescent Chemosensors for Ion and Molecule Recognition, American Chemical Society, Washington,

DC, **1992**; c) G. D. Scholes, K. P. Ghiggino, *J. Chem. Phys.* **1994**, *101*, 1251-1261; d) D. T. McQuade, A. E. Pullen, T. M. Swager, *Chem. Rev.* **2000**, *100*, 2537-2574; e) B. S. Gaylord, A. J. Heeger, G. C. Bazan, *Proc. Natl. Acad. Sci.* USA **2002**, *99*, 10954-10957; f) B. Liu, G. C. Bazan, *Chem. Mater.* **2004**, *16*, 4467-4476; g) S. W. Thomas III, G. D. Joly, T. M. Swager, *Chem. Rev.* **2007**, *107*, 1339-1386; h) D. W. Domaille, E.-L. Que, C.-J. Chang, *Nat. Chem. Biol.* **2008**, *4*, 168-175; i) T. Terai, T. Nagano, *Curr. Opin. Chem. Biol.* **2008**, *12*, 515- 521.

12. G. S. Wilson, M. A. Johnson, *Chem. Rev.* **2008**, *108*, 2462-2481.
13. D. W. Hatchett, M. Josowicz, *Chem. Rev.* **2008**, *108*, 746-769.
14. Y. Yang, Q. Zhao, W. Feng, F. Li, *Chem. Rev.* **2013**, *113*, 192-270
15. J. You, G. Li, Z. Wang, *Org. Biomol. Chem.* **2012**, *10*, 9481-9490.
16. J. You, G. Li, R. Wang, Q. Nie, Z. Wang, J. Li, *Phys. Chem. Chem. Phys.* **2011**, *13*, 17825-17830.
17. K.-S. Kim, S. Jeong, C. Kim, J.-Y. Ham, Y. Kwon, B.-D. Choi, Y. S. Han, *Synth. Met.* **2009**, *159*, 1870-1875.

Chapter 5

Summary and Perspectives

Covalent organic frameworks (COFs) and conjugated microporous polymers (CMPs) are two new classes of porous polymers that allow the integration of organic units with atomic precision into long-range-ordered two and three-dimensional structures. From a synthetic point of view, COFs and CMPs are intriguing scaffolds since they allow a new degree of control of porosity, composition and component positions. However, the construction of COFs and CMPs to date has been limited to certain monomers, and the lack of suitable protocols utilizing other units has impeded further advances in this emerging field. To advance this emerging field it is important to extend the limited number of synthetic protocols and monomer units available and explore the advanced application for these two kinds of materials. From this point of view, in this context, I explored the possibility of constructing functional COFs and CMPs with novel π systems and new protocol.

Carbon dioxide has been considered as the primary anthropogenic greenhouse gas accumulated by the human activities, which is responsible for global warming and climate change. The level of CO_2 in the atmosphere is increasing everyday through the combustion of fossil fuels and wastes, and also via several chemical reactions used in the industrial processes. Thus, in order to decrease the CO_2 level in atmosphere, its removal from flue-gas streams via adsorption or sequestration is very important. Although, commercial carbon dioxide capture systems are known but their capture quantity/capacity is much smaller than that of the demand. Hence, research on the design and synthesis of high CO_2 adsorbent material for carbon capture and sequestration (CCS) is an emerging and first growing area of research.

In Chapter 1, we developed a strategy for convertinga conventional 2D COF into an outstanding CO_2 capture scaffold through channel-wall functionalization. The high-throughput ring opening reaction is useful for creating carboxylic-acid-functionalized channel walls while retaining the layered and open porous structure. Given the rather limited room for increasing the porosity of 2D COFs, together with the availability of a broad diversity of different functional groups, we anticipate that the present channel-wall engineering strategy will be critical to exploring 2D COFs for high-performance gas storage and separation. In Chapter 2, COFs with highly functionalized pore wall structures are difficult to obtain via direct poly-condensation reactions. The systematic pore surface engineering of COFs enables the tailor-made covalent docking of a variety of different functional groups with controlled loading contents to the pore

walls. The surface engineering of the pore walls profoundly affects the surface area, pore size, pore volume, and pore environment. As demonstrated for CO_2 adsorption, pore surface engineering is a high throughput and efficient method for achieving both enhanced adsorption capacities and improved separation capabilities. Notably, this approach is not limited to the present COF and is widely applicable to many other previously reported COFs. We envisage that pore surface engineering might be a general strategy for screening for COF materials that satisfy the multiple requirements of CO_2 capture in industrial level flow-gas applications.

In Chapter 3, we have developed the techniques for producing surface-exposed yet stable metal nanoparticles by locking them within a dual-module mesoporous and microporous three-dimensional π-network. The palladium nanoparticles exhibit inherently superior activity in the heterogeneous catalysis of different types of carbon–carbon bond formation reactions. Unreactive aryl chlorides are efficiently catalysed in Suzuki, Sonogashira and Stille coupling reactions in neat water under mild conditions. This novel class of heterogeneous catalysts, unlike previous examples thus far reported, combines activity, stability, reusability, versatility and environmental compatibility; these advantages offer a plausible solution to long-standing challenges for real applications in the field of heterogeneous catalyst. Therefore, these advancements open new perspectives in the design of heterogeneous catalysts for the sustainable production of fuels and chemicals. The present technique is applicable to producing various surface-exposed metal nanoparticles; utilization of this technique may disclose inherent functions and applications of other nanoparticles.

In Chapter 4, we have developed an electrochemical approach for the controlled synthesis of thin films of conjugated microporous polymers. The thickness of the CMP films can be synthetically controlled, and the films can be obtained on substrates or as freestanding films. The films are unique in that they are porous, possess extended π conjugation, allow exciton delocalization over the skeletons, and enable high-rate electron transfer. Because of these features, we developed the CMP films as versatile platforms for chemo- and biosensing. The CMP sensors feature excellent selectivity, rapid response, and high sensitivity, discriminate electron-rich and electron-poor arenes through fluorescence on/off sensing, and selectively detect oxidative ions by redox-induced fluorescence quenching. The films function as label-free sensors for the highly sensitive detection of biologically important dopamine and HOCl species. Given the structural

diversity and flexibility of CMPs, we anticipate the emergence of an exciting field in designing CMP films, which would significantly expand the potential of CMPs for applications.

In summary, COFs and CMPs represent a new synthetic era in the field of organic materials. Their unique features, such as highly flexible molecular design, permanent porosity, and controllable pore size, and the diversity of available building blocks promise that this field, although currently in its infant stages, will grow into a rich and broad area of great importance. In this context, the development of new synthetic methods and the exploration of new linkage reactions is key to expanding the COF and CMP family. A more direct tool for evaluating the layered structure of COFs and CMPs, especially the slipped distance, is desired. The determination of defects in the framework and improved understanding of the thermodynamic behaviors of DCC during the condensation reactions would enable the consistent preparation of high-quality COF and CMP materials. The synthetic control of the macroscopic shape of the COF and CMP materials is another important aspect that requires development. Enhancing the complexity of the COF and CMP structures and generating multifunctional COFs and CMPs are an important issue in the functional exploration. This is possible by developing multicomponent reaction systems or post-synthesis modifications. Most importantly, the complementary functional design of both the pores and skeletons may provide a practical means of exploring COFs and CMPs for challenging energy and environmental issues.

List of Publications

発表論文リスト

1. **Ning Huang**, Rajamani Krishna and Donglin Jiang.
   Tailor-Made Pore Surface Engineering in Covalent Organic Frameworks: Systematic Functionalization for Performance Screening.
   J. Am. Chem. Soc. **2015**, *137*, 7079-7082.
2. **Ning Huang**, Xuesong Ding, Jangbae Kim, Hyotcherl Ihee, and Donglin Jiang.
   A Photoresponsive Smart Covalent Organic Framework.
   Angew. Chem. Int. Ed. **2015**, DOI: 10.1002/anie.201503902.
3. **Ning Huang**, Xiong Chen, Rajamani Krishna and Donglin Jiang.
   Two dimensional covalent organic frameworks for carbon dioxide capture through channel-wall functionalization.
   Angew. Chem. Int. Ed. **2015**, *54*, 2986-2990.
4. Cheng Gu*, **Ning Huang***, Fei Xu, Jia Gao, Donglin Jiang.
   Cascade exciton-pumping engines with manipulated speed and efficiency in light-harvesting porous π-network films.
   Scientific Reports **2015**, *5*, 8867. (* These authors contributed equally to this work.)
5. Cheng Gu*, **Ning Huang***, Yang Wu, Hong Xu, Donglin Jiang.
   Design of highly photofunctional porous polymer films with controlled thickness and prominent microporosity. (* These authors contributed equally to this work.)
   Angew. Chem. Int. Ed. **2015**, DOI: 10.1002/anie.201504786.
6. **Ning Huang**, Yanhong Xu, Donglin Jiang.
   High-performance heterogeneous catalysis with surface-exposed stable metal nanoparticles.
   Scientific Reports **2014**, *4*, 7228.
7. Cheng Gu*, **Ning Huang***, Jia Gao, Fei Xu, Yanhong Xu and Donglin Jiang.
   Controlled synthesis of conjugated microporous polymer films: versatile platforms for highly sensitive and label-free chemo- and biosensing.
   Angew. Chem. Int. Ed. **2014**, *53*, 4850-4855. (* These authors contributed equally to this work.)

8. Xiong Chen, **Ning Huang**, Jia Gao, Hong Xu, Fei Xu and Donglin Jiang.
   Towards covalent organic frameworks with predesignable and aligned open docking sites.
   Chem. Commun. **2014**, *50*, 6161-6163.
9. Xiong Chen, Matthew Addicoat, Enquan Jin, Lipeng Zhai, Hong Xu, Ning Huang, Zhaoqi Guo, Lili Liu, Stephan Irle, and Donglin Jiang.
   Locking covalent organic frameworks with hydrogen bonds: general and remarkable effects on crystalline structure, physical properties, and photochemical activity
   J. Am. Chem. Soc. **2015**, *137*, 3241-3247.

学会発表リスト

1. The 8th International Conference on Materials for Advanced Technologies of the Materials Research Society of Singapore & IUMRS-International Conference in Asia (ICMAT2015 & IUMRS-ICA2015), Jun. 28-Jul. 3 **2015**, Singapore. *"Covalent Organic Frameworks for Carbon Dioxide Adsorption and Separation"* (Poster presentation)
2. The 64nd SPSJ Annul Meeting, May 26-29 **2015**, Sapporo, Japan. *"Surface Engineering of Covalent Organic Frameworks"* (Oral presentation)
3. The 96th Annual Meeting of CSJ, Mar. **2015**, Tokyo, Japan. *"Band Gap Engineering in Covalent Organic Frameworks"* (Oral presentation)
4. The Winter School of Asian CORE Program, Jan. **2015**, Okazaki, Japan. *"Enhancement of CO_2 Adsorption in Covalent Organic Frameworks via Pore Size and Surface Engineering"* (Poster presentation)
5. China-Japan Joint Symposium on Functional Supramolecular Architectures, Dec. **2014**, Tianjin, China. *"Surface Exposed Stable Metal Nanoparticles for High-Performance Heterogenerous Catalysis"* (Oral presentation)
6. The 10th SPSJ International Polymer Conference, Dec. **2014**, Tsukuba, Japan *"Pore Surface Engineering of Covalent Organic Frameworks and Impact on Carbon Dioxide Adsorption"* (Oral presentation)
7. MOF2014, Sep. **2014**, Kobe, Japan. *"Designing Covalent Organic Frameworks for Exceptional Carbon Dioxide Adsorption and Separation"* (Poster presentation)

8. The 63rd Symposium on Macromolecules, Sep. **2014**, Nagasaki, Japan *"High-Performance Nanoparticle Catalyst in Conjugated Mesoporous Polymers"* (Oral presentations)
9. 248th ACS National Meeting & Exposition, Aug. **2014**, San Francisco, USA *"Developing 2D Covalent Organic Frameworks for Carbon Dioxide Adsorption"* (Poster presentation)
10. The 95th Annual Meeting of CSJ, Mar. **2014**, Nagoya, Japan. *"Pore Surface Engineering of Covalent Organic Frameworks and Impact on Carbon Dioxide Adsorption"* (Oral presentations)
11. The Winter School of Asian CORE Program, Feb. **2014**, Taibei, Taiwan. *"Design and Applications of Photo-Responsive Covalent Organic Frameworks"* (Oral & Poster presentations)
12. 246th ACS National Meeting & Exposition, Sep. **2013**, Indianapolis, USA. *"Anthracene-Based Covalent Organic Frameworks and Layer Locking-and-Unlocking Driven by External Stimuli"* (Poster presentation)
13. The 62nd SPSJ Annul Meeting, May **2013**, Kyoto, Japan. *"Covalent Organic Frameworks Transformation under External Stimuli"* (Oral presentation)
14. The Winter School of Asian CORE Program, Jan. **2013**, Busan, Korea. *"Covalent Organic Frameworks for Photo Response Application"* (Poster presentation)

Acknowledgements

I wrote my thesis with a big thankful heart. During the past 3 years at IMS, I received countless amounts of help and support from many people. I wish I could find a better way to express my thankfulness.

The first one I would like to thank is my advisor, Prof. Donglin Jiang, for all his advice, encouragement and help all these years. From him, I saw the attributes of a great scientist, and learned a lot that can never be obtained in classrooms. I was extremely fortunate to get trained under his supervision. His insight, attitude and enthusiasm have been a never-ending source of inspiration and support. His encouragement and patience have made my time working here so enjoyable, even in difficulties and failures. I know I can never repay him for what I have received, and I hope I can pass these qualities on when I have opportunities to help others.

The interdisciplinary work presented in this thesis would have not been possible without close collaborations and interactions with experts from various fields, and from different departments and universities. In particular, I collaborate very closely with Prof. Rajamani Krishna in Amstdam University, who helped us to calculate the selectivity of carbon dioxide over nitrogen of all the COFs materials presented in this thesis. I would like to give my thankfulness for their wonderful work. I was also fortunate to have the opportunity to work closely with Prof. Stephan Irle in Nagoya University. Their structure optimization helps us a lot to understand the structure of all the materials. Moreover, Dr. Cheng Gu in our group contributed significantly to my research efforts.

The work in this thesis could not be done without the help from the people at the Instrument Center in IMS. I'm especially thankful to Dr. Motoyasu Fujiwara, Dr. Satoru Nakao, Ms. Midori Saito, Mr. Seiji Makita and Ms. Michiko Nakano, for their kind helps in PXRD, FE-SEM, HR-TEM, EA and NMR measurements.

I also owe my sincere gratitude to my friends and my labmates Dr. Sasanka Dalapati, Dr. Yanhong Xu, Dr. Xiong Chen, Dr. Hong Xu, Mr. Yang Wu, Mr. Fei Xu, Mr. Enquan Jin, Mr. Jia Gao, Mr. Lipeng Zhai, Miss Ping Wang, Miss Shanshan Tao, Mr. Qing Xu and our secretary Ms. Sayuri Suzuki, who gave me their help and encouragements in not only research but also everyday

life.

Last but not least, I would like to thank my family, my mother, father, sister and my wife for all their love, supports and encouragements almost all my life.

Ning Huang

2015